The Pennsylvania State University
The Graduate School

CLASSIFICATION AND MODELING OF HUMAN ACTIVITIES USING EMPIRICAL MODE DECOMPOSITION WITH S-BAND AND MILLIMETER-WAVE MICRO-DOPPLER RADARS

A Dissertation in
Electrical Engineering
by
Dustin P. Fairchild

© 2013 Dustin P. Fairchild

Submitted in Partial Fulfillment
of the Requirements
for the Degree of

Doctor of Philosophy

December 2013

The dissertation of Dustin P. Fairchild was reviewed and approved* by the following:

Ram M. Narayanan
Professor of Electrical Engineering
Dissertation Advisor, Chair of Committee

Timothy J. Kane
Professor of Electrical Engineering

Randy Young
Senior Research Associate

Kamesh Madduri
Assistant Professor of Computer Science and Engineering

Kultegin Aydin
Professor of Electrical Engineering
Department Head

*Signatures are on file in the Graduate School.

Abstract

The ability to identify human movements can be an important tool in many different applications such as surveillance, military combat situations, search and rescue operations, and patient monitoring in hospitals. This information can provide soldiers, security personnel, and search and rescue workers with critical knowledge that can be used to potentially save lives and/or avoid a dangerous situation. Most research involving human activity recognition is focused on using the Short-Time Fourier Transform (STFT) as a method of analyzing the micro-Doppler signatures. Because of the time-frequency resolution limitations of the STFT and because Fourier transform-based methods are not well-suited for use with non-stationary and nonlinear signals, we have chosen a different approach for classification. Empirical Mode Decomposition (EMD) has been shown to be a valuable time-frequency method for processing non-stationary and nonlinear data such as micro-Doppler signatures and EMD readily provides a feature vector that can be utilized for classification. For classification, the method of a Support Vector Machine (SVMs) was chosen. SVMs have been widely used as a method of pattern recognition due to their ability to generalize well and also because of their moderately simple implementation.

In this dissertation, we discuss the ability of these methods to accurately identify human movements based on their micro-Doppler signatures obtained from S-band and millimeter-wave radar systems. Comparisons will also be made based on experimental results from each of these radar systems. Furthermore, we will present simulations of micro-Doppler movements for stationary subjects that will enable us to compare our experimental Doppler data to what we would expect from an "ideal" movement.

The Doppler radars that were developed for human activity classification consisted of a transmitter and a single receiver that are colocated in a quasi-monostatic configuration. Thus, only the radial component of the target's velocity produces

a Doppler signal. If the target is moving tangentially to the radar line of sight, Doppler signals cannot be detected. To remedy this, multiple bistatic radars can be utilized so that if one receiver does not detect Doppler, the other will. In addition to providing more information for classification purposes, multiple Doppler sensors can also be employed to determine a moving target's orientation by comparing the Doppler frequency shift at each sensor. The algorithm developed here uses the relationship between the Doppler frequencies measured at each sensor to determine the oscillation angle of the target. Experiments have been performed which show excellent agreement with simulations for both the mechanical motion of a swinging pendulum and also for simple human motions. These capabilities are discussed in detail and the experimental results are shown for a micro-Doppler radar system with a single transmitter and two receivers. Classification results using a 2-sensor micro-Doppler radar are be presented.

Contents

List of Figures viii

List of Tables xiv

Acknowledgments xvi

Chapter 1
Introduction 1

Chapter 2
Background 6
2.1 Noise Radar . . . 6
2.1.1 Radar Basics . . . 6
2.1.2 Range Resolution . . . 7
2.1.3 Target Ranging and Matched Filtering . . . 8
2.2 Doppler . . . 10
2.3 Through-the-Wall Radar Considerations . . . 11
2.3.1 Wall Attenuation . . . 11
2.3.2 Wall Reflection . . . 15
2.3.3 Dispersion . . . 15
2.3.4 Signal-to-Noise Ratio and Maximum Detectable Range . . . 16
2.3.5 Wall Effects on Micro-Doppler Signatures . . . 19
2.3.5.1 Constant Phase Offset . . . 19
2.4 Micro-Doppler Signals of Targets with a Translational Velocity . . . 22
2.4.1 Walking Humans . . . 23
2.4.2 Animals . . . 25

Chapter 3
S-Band Radar Design **30**
3.1 Design Considerations . . . 30
3.2 System Description . . . 31
3.2.1 Transmit Chain . . . 33
3.2.2 Receive Chain . . . 34
3.2.3 Antennas . . . 35
3.3 Through-wall Ranging Results . . . 39

Chapter 4
Millimeter-Wave Radar Design **44**
4.1 Design Considerations . . . 44
4.2 System Description . . . 46
4.2.1 Transmit Chain . . . 48
4.2.2 Receive Chain . . . 50
4.2.3 Antennas . . . 51
4.3 Ranging Results . . . 54
4.3.1 Long Range Detection . . . 54
4.3.2 Through Foliage Detection . . . 56

Chapter 5
Time-Frequency Transforms **58**
5.1 Short-Time Fourier Transform . . . 58
5.2 Continuous Wavelet Transform . . . 59
5.3 The Hilbert-Huang Transform and Empirical Mode Decomposition . 60
5.4 Other Time-Frequency Transforms . . . 65

Chapter 6
Micro-Doppler Signals of Stationary Targets **67**
6.1 Experimental micro-Doppler of Human Motions . . . 67
6.2 Models of Simple Human Motions . . . 80
6.3 Comparison of Through-the-Wall vs. Non-Through-the-Wall micro-Doppler Signatures . . . 95
6.4 Adding Randomness to Human Motion Simulations . . . 99

Chapter 7
Classification of Micro-Doppler Signatures **107**
7.1 Support Vector Machines . . . 107
7.2 Classification Results . . . 110
7.3 Analysis of Classification Accuracy for Measurement Error . . . 121

Chapter 8
Effect of Stopping Criteria on EMD and SVM **130**

Chapter 9
MIMO Doppler for Detecting Target Orientation **137**
9.1 MIMO Doppler Background 138
9.2 Theoretical Results 139
9.3 Experimental Results 147
9.4 Classification of MIMO Doppler Signals 151

Chapter 10
Conclusions and Recommendations for Future Work **159**
10.1 Conclusions 159
10.2 Future Work 160

Bibliography **162**

List of Figures

2.1 One-way attenuation of EM waves (in dB) through various materials [1]. 14
2.2 Maximum detectable range for a given loss (relative to $L = 1$). . . . 18
2.3 Maximum detectable range versus Γ. 19
2.4 Theoretical DC offset versus range to the wall as a fraction of λ. . . 21
2.5 Experimental DC offset versus range to the wall as a fraction of λ. . 21
2.6 Spectrogram of a human walking toward a radar [2]. 23
2.7 Spectrogram of a human walking toward a radar [3]. 24
2.8 Spectrogram of a human walking using an S-band, non-coherent, micro-Doppler radar. 25
2.9 Spectrogram of a horse walking toward a Sonar [4]. 26
2.10 Spectrogram of a Pit Bull walking toward a Sonar [4]. 27
2.11 Spectrogram of a human walking away from a Sonar [4]. 28
2.12 Spectrogram of a horse walking [5]. 29

3.1 Block diagram of S-band noise radar. 32
3.2 Photograph of the S-band noise radar. 33
3.3 Diagram of helical antenna with important parameters highlighted. 36
3.4 Final design of the helical antennas. 38
3.5 S11 measurements of the helical antennas. 39
3.6 Range profiles of a 4 inch thick brick wall that is 6 feet from the radar with (Top) no target behind it and (Bottom) a small trihedral target 4 feet behind the brick wall. 40
3.7 Range profile of a 5-inch thick wall made of concrete slabs. The wall is 5 feet from the radar and (Top) no target is placed behind the wall and (Bottom) a small trihedral target is placed 6 feet behind the wall. 41
3.8 Range profile of a 4-inch thick concrete wall located at 5 feet from the radar and (Top) with no target behind the wall and (Bottom) with a small trihedral target placed 5 feet behind the wall. 42

3.9 Range profile of a trihedral target located 6 feet behind a 4 inch thick brick wall (Top) without additional signal processing and (Bottom) after background subtraction. 43

4.1 Atmospheric absorption vs. frequency. 45
4.2 Block diagram of the mm-wave radar system. 47
4.3 Photograph of the completed mm-wave radar system. 48
4.4 L-band waveform consisting of a 500 MHz bandwidth noise waveform with an embedded CW tone. 50
4.5 Dielectric horn antennas used with the mm-wave radar. 52
4.6 Beam pattern of the dielectric horn antennas for (Top) E-Plane and (Bottom) H-Plane. 53
4.7 Correlation plot of human target standing at 700 feet (213 meters) prior to background subtraction. 55
4.8 Correlation plot of human target standing at 700 feet (213 meters) after background subtraction. 56
4.9 Correlation plots of the bush at 100 feet (a) without leaves and no target behind it, (b) without leaves and with a corner reflector behind it, (c) with leaves and with a corner reflector behind it, and (d) without leaves and with a human target behind it. 57

5.1 EMD algorithm flowchart. 62

6.1 (Left) Experimentally measured micro-Doppler of a pendulum and (Right) STFT of the micro-Doppler signal for an S-band radar. . . 69
6.2 (Left) Experimentally measured micro-Doppler of a pendulum and (Right) STFT of the micro-Doppler signal for a mm-wave radar. . . 70
6.3 (Left) Experimentally measured micro-Doppler of a person swinging their arms and (Right) STFT of the micro-Doppler signal for an S-band radar. 71
6.4 (Left) Experimentally measured micro-Doppler of a person swinging their arms and (Right) STFT of the micro-Doppler signal for a mm-wave radar. 72
6.5 (Left) Experimentally measured micro-Doppler of a person breathing and (Right) STFT of the micro-Doppler signal for an S-band radar. 73
6.6 (Left) Experimentally measured micro-Doppler of a person breathing and (Right) STFT of the micro-Doppler signal for a mm-wave radar. 74

6.7 (Left) Experimentally measured micro-Doppler of a person picking up an object and (Right) STFT of the micro-Doppler signal for an S-band radar. . . . 75
6.8 (Left) Experimentally measured micro-Doppler of a person picking up an object and (Right) STFT of the micro-Doppler signal for a mm-wave radar. . . . 76
6.9 (Left) Experimentally measured micro-Doppler of a person transitioning from crouching to standing and (Right) STFT of the micro-Doppler signal for an S-band radar. . . . 77
6.10 (Left) Experimentally measured micro-Doppler of a person transitioning from crouching to standing and (Right) STFT of the micro-Doppler signal for a mm-wave radar. . . . 78
6.11 Micro-Doppler characteristics of various human activities [6]. . . . 79
6.12 (Left) Simulated micro-Doppler of a pendulum and (Right) STFT of the simulated micro-Doppler signal of the pendulum for an S-band radar. . . . 81
6.13 (Left) Simulated micro-Doppler of a pendulum and (Right) STFT of the simulated micro-Doppler signal of the pendulum for a mm-wave radar. . . . 82
6.14 (Left) Simulated micro-Doppler of swinging arms and (Right) STFT of the simulated micro-Doppler signal for an S-band radar. . . . 84
6.15 (Left) Simulated micro-Doppler of swinging arms and (Right) STFT of the simulated micro-Doppler signal for a mm-wave radar. . . . 85
6.16 (Top) Simulated chest displacement for a human breathing and (Bottom) illustration of chest expansion and contraction. . . . 86
6.17 (Left) Simulated micro-Doppler of breathing and (Right) STFT of the simulated micro-Doppler signal for an S-band radar. . . . 87
6.18 (Left) Simulated micro-Doppler of breathing and (Right) STFT of the simulated micro-Doppler signal for a mm-wave radar. . . . 88
6.19 (Top) Simulated angular trajectory of a human picking up an object and (Bottom) side view of the motion. . . . 89
6.20 (Left) Simulated micro-Doppler of picking up an object and (Right) STFT of the simulated micro-Doppler signal for an S-band radar. . . . 90
6.21 (Left) Simulated micro-Doppler of picking up an object and (Right) STFT of the simulated micro-Doppler signal for a mm-wave radar. . . . 91
6.22 (Top) Simulated angular trajectory of a human standing up from a crouching position and (Bottom) side view of the motion. . . . 93
6.23 (Left) Simulated micro-Doppler of transitioning from crouching to standing and (Right) STFT of the simulated micro-Doppler signal for an S-band radar. . . . 94

6.24 (Left) Simulated micro-Doppler of transitioning from crouching to standing and (Right) STFT of the simulated micro-Doppler signal for a mm-wave radar. 95
6.25 Comparison of the micro-Doppler signal of a pendulum (Top) without a wall barrier and (Bottom) with a wall barrier. 96
6.26 Comparison of the micro-Doppler signal of a pendulum (Top) without a wall barrier and (Bottom) with a wall barrier. 97
6.27 Comparison of the energy of each IMF produced by EMD for a pendulum (Top) without a wall barrier and (Bottom) with a wall barrier. 98
6.28 Comparison of the energy of each IMF produced by EMD for a person swinging arms (Top) without a wall barrier and (Bottom) with a wall barrier. 99
6.29 (Top) original angular trajectory for the pendulum simulation and (Bottom) angular trajectory for a pendulum after randomization. . 101
6.30 (Left) Simulated micro-Doppler of a pendulum with randomness added to the angle and (Right) STFT of the simulated micro-Doppler signal for a mm-wave radar. 102
6.31 (Left) Simulated micro-Doppler of a human swinging arms with randomness added to the upper arm angle and (Right) STFT of the simulated micro-Doppler signal for a mm-wave radar. 103
6.32 (Left) Simulated micro-Doppler of a human picking up an object with randomness added in the form of swaying and (Right) STFT of the simulated micro-Doppler signal for a mm-wave radar. 104
6.33 (Left) Simulated micro-Doppler of a human standing up from a crouching position with randomness added in the form of swaying and (Right) STFT of the simulated micro-Doppler signal for a mm-wave radar. 104
6.34 (Top Left) Simulated micro-Doppler signature of a human breathing after including swaying motions, (Bottom Left) STFT of the simulated breathing signature, (Top Right) experimentally measured breathing signature for a human subject who remained standing, and (Bottom Right) STFT of the experimentally measured breathing signature. 106

7.1 ROC curve for 6-Class classification (100 trials averaged). 111
7.2 Classification accuracy after adding zero mean, uniformly distributed random noise to each feature with test subject 1 used for the data in the test set. 122

7.3 Classification accuracy after adding positive, uniformly distributed random noise to each feature with test subject 1 used for the data in the test set. . . . 123
7.4 Classification accuracy after adding negative, uniformly distributed random noise to each feature with test subject 1 used for the data in the test set. . . . 123
7.5 Classification accuracy after adding normally distributed random noise to each feature with test subject 1 used for the data in the test set. . . . 124
7.6 Classification accuracy after adding zero mean, uniformly distributed random noise to each feature with test subject 4 used for the data in the test set. . . . 125
7.7 Classification accuracy after adding positive, uniformly distributed random noise to each feature with test subject 4 used for the data in the test set. . . . 125
7.8 Classification accuracy after adding negative, uniformly distributed random noise to each feature with test subject 4 used for the data in the test set. . . . 126
7.9 Classification accuracy after adding normally distributed random noise to each feature with test subject 4 used for the data in the test set. . . . 126
7.10 Classification accuracy after adding positive, uniformly distributed random noise to each feature with test subject 4 used for the data in the test set. The horizontal axis has been expanded beyond 100%. 127
7.11 Classification accuracy after adding zero mean, uniformly distributed random noise to each feature with test subject 1 used for the data in the test set. . . . 128
7.12 Classification accuracy after adding positive, uniformly distributed random noise to each feature with test subject 1 used for the data in the test set. . . . 128
7.13 Classification accuracy after adding negative, uniformly distributed random noise to each feature with test subject 1 used for the data in the test set. . . . 129
7.14 Classification accuracy after adding normally distributed random noise to each feature with test subject 1 used for the data in the test set. . . . 129

8.1 Decimation factor vs. EMD and SVM Completion Times. . . . 131
8.2 Decimation factor vs. SVM accuracy. . . . 132
8.3 Threshold1 value vs. EMD and SVM Completion Times. . . . 132

8.4 Threshold1 value vs. SVM accuracy. 133
8.5 Threshold2 value vs. EMD and SVM Completion Times. 133
8.6 Threshold2 value vs. SVM accuracy. 134
8.7 Tolerance factor vs. EMD and SVM Completion Times. 134
8.8 Tolerance factor vs. SVM accuracy. 135
8.9 Maximum number of EMD inner loop iterations vs. EMD and SVM Completion Times. 135
8.10 Maximum number of EMD inner loop iterations vs. SVM accuracy. 136

9.1 Diagram of a bistatic Doppler radar. 139
9.2 Diagram of the multiple radar sensor configuration. 140
9.3 (Left) Measured angle θ using $k_1 = \frac{\max(f_{d2})}{\max(f_{d1})}$ and (Right) k_1 for a simple oscillating target. 142
9.4 (Left) Measured angle θ using $k_2 = \frac{\max(f_{d2}) - \max(f_{d1})}{\max(f_{d1}) + \max(f_{d2})}$ and (Right) k_2 for a simple oscillating target. 144
9.5 Measured angle θ based on a simulated oscillating target. 145
9.6 Measured angle θ based on a simulated oscillating target with poor STFT frequency resolution. 146
9.7 Simplified block diagram of the 2-sensor radar system. 147
9.8 (Top) STFT of the experimentally measured Doppler signal from receiver 1 and (Bottom) STFT of the experimentally measured Doppler signal from receiver 2 using a pendulum. 148
9.9 Experimentally measured angle using a pendulum as the target. . . 149
9.10 Experimentally measured angle for a human swinging their arms. . 149
9.11 Experimentally measured angle for a human picking up an object. . 150
9.12 Experimentally measured angle for human transitioning from crouching to standing. 150
9.13 Experimentally measured angle for a human breathing while standing. 151
9.14 Setup for collecting MIMO Doppler data for classification. 152
9.15 Setup for collecting MIMO Doppler data for classification. 156

List of Tables

2.1 Attenuation and relative permittivity of some selected materials at 100 MHz [7]. 13
2.2 Attenuation of typical wall materials at 500 MHz [8]. 13

3.1 Helical Antenna Parameters 37

7.1 Comparison of the 1-a-a Method and Decision Tree Method of Multi-Class Classification 112
7.2 Classification results - S-band radar without wall barrier. 114
7.3 Classification results - S-band radar through laboratory wall. 115
7.4 Classification results - S-band radar through brick wall. 115
7.5 Classification results - S-band radar through cinder block wall. . . . 116
7.6 Classification Results - mm-Wave Radar at a Range of 100 feet. . . 117
7.7 Classification Results - mm-Wave Radar at a Range of 200 feet. . . 118
7.8 Classification Results - mm-Wave Radar at a Range of 300 feet. . . 118
7.9 Confusion Matrix for the Classification of S-Band micro-Doppler signals Through a Cinder Block Wall. 119
7.10 Confusion Matrix for the Classification of mm-wave micro-Doppler signals at a Distance of 91 m. 120

9.1 Description of classification scenarios when the antennas are placed linearly. 153
9.2 Classification results using a multi-sensor radar with human targets facing in two different directions when the receive antennas are placed linearly as in Figure 9.2. 154
9.3 Description of classification scenarios when the total path lengths are equal for both sensors. 155
9.4 Classification results using a multi-sensor radar with human targets facing in multiple directions when the total path lengths are equal for both sensors. 156

9.5 Confusion Matrix for the Classification of Scenario #1 (Monostatic radar with the target at an angle of 0°). 158
9.6 Confusion Matrix for the Classification of Scenario #2 (Monostatic radar with the target at an angle of 45°). 158
9.7 Confusion Matrix for the Classification of Scenario #5 (Bistatic radar with the target at an angle of 45°). 158

Acknowledgments

I would first and foremost like to thank my Lord and Savior Jesus Christ to whom I owe everything. Apart from Him I can do nothing.

This work was supported by the U.S. Army ARDEC Joint Service Small Arms Program (JSSAP) under Contract #W15QKN-09-C-0116. I appreciate fruitful discussions with E. Beckel, W. Luk, J. Patel, and G. Gaeta.

I would also like to express my gratitude to my advisor, Dr. Narayanan, for his knowledge and guidance. Also to Dr. Kane, Dr. Young, and Dr. Madduri for serving as members of my committee. I would also like to thank my parents, Dan and Lisa, my sister, Whitney, my brother, Eric, and all of the rest of my family for their love and support. Also, thanks to everyone in the Radar and Communications Laboratory for their assistance and willingness to volunteer to help collect data and especially to Kyle Gallagher and Sonny Smith, who worked alongside me on this project.

"For You have been my help, And in the shadow of Your wings I sing for joy" (Psalm 63:7).

"I can do all things through Him who strengthens me" (Philippians 4:13).

Chapter 1

Introduction

The detection of human targets and the ability to identify their movements is a growing area of interest recently. The ability to sense human targets through walls, at long ranges, and through light foliage is a challenging problem which has many potential applications in a diverse range of areas. Some applications for the deployment of this radar sensor include areas such as surveillance, search and rescue, and medical sensing where contact sensors are undesirable. One such example of a medical application where contact sensors cannot be used is for monitoring the respiration of burn victims.

The primary motivation for the work described in this dissertation is to provide the warfighter with additional information that will improve safety and effectiveness. To accomplish this goal, we propose the development of a lightweight sensor that can be mounted on small arms platforms such as rifles and pistols. It is desired that the sensor be capable of detecting targets concealed behind walls and light foliage. It should be able to operate when the wall barrier is constructed from materials that are commonly used in homes and commercial buildings, such as brick, concrete, wood, and drywall. Additionally, it is desired that both the range to the target and the target's micro-Doppler signature be extracted. Additional signal processing techniques can then be implemented to analyze the micro-Doppler signature to infer additional information about the target.

Because target localization is desired, ranging information alone is not adequate. In order to localize the target in azimuth, the antenna beamwidths must be appropriately chosen so as to isolate the width of a typical human target and

avoid illuminating two targets simultaneously. If only one human target can be within the antenna beam, then the above-mentioned capability of ensuring maximum lethality can be achieved. Otherwise, if more than one human target is within the antenna beam, the warfighter cannot be confident that the radar sensor will aid in hitting the target and the warfighter may not even be aware of the presence of a second target.

For this radar sensor to be mounted directly onto small arms platforms it is necessary to operate the radar at high frequencies. The higher the frequency, the smaller the antenna footprint. Using as small and as light a system as possible is desired because the warfighter is limited in the amount of weight that can be carried. In order to achieve a small size, microwave or millimeter-wave (mm-wave) frequencies should be chosen. High frequencies such as mm-wave, however, are not suitable for through-wall operation because of the high losses that are involved. However, mm-wave frequencies are desired because the system is capable of being smaller and the Doppler frequency shifts from moving targets will be much greater than that of a system operating in microwave frequencies. If the radar sensor is to be operated in situations where the target is concealed behind light foliage, then mm-wave frequencies may be used because the loss will not be as great since the barrier is not as thick or dense as a wall barrier.

For the reasons described above, two covert, multi-modal radar systems have been developed at the Radar and Communications Laboratory at The Pennsylvania State University. Both radar systems utilize a composite waveform consisting of a noise waveform that is used for target ranging and a single, continuous wave (CW) tone for detecting micro-Doppler signatures that arise from human motions. The micro-Doppler signals that are detected are processed separately from the noise waveform so that the radar operator can identify the type of movement that the target is performing. For ranging, a noise waveform is utilized, which permits the radar to be covert and have low probability of intercept and anti-jamming capabilities.

The first radar operates in the S-band so that wall barriers can be penetrated. This radar is designed with close range scenarios in mind, where a target is concealed behind a wall barrier. At close ranges, reasonable antenna apertures can be designed that will localize a single human target and Doppler frequencies will be

observable.

The second radar operates at mm-wave frequencies, more specifically in the W-band. This radar is designed with longer range applications in mind or possibly for scenarios where the target is concealed behind light foliage. The high frequency of operation allow the antenna beamwidths to be narrow enough to localize a single human target, while still having a reasonably small aperture size to be mounted on small arms. In addition to this, the higher transmit frequency will result in larger Doppler frequency shifts that will improve the identification of human movements.

Noise radar systems have been around for a long time now. The theory for noise and noise-like waveforms for radar began in the 1950's and by the 1960's, Cooper [9, 10] constructed some of the first noise radar systems. Noise radar systems have some unique advantages over traditional radar waveforms due to their being inexpensive to generate, having covert properties, and their low probability of intercept and anti-jamming capabilities. Covertness arises from the signal having no distinguishable features and also because the power is spread over a large bandwidth. This means the spectral density is low across the entire bandwidth of the noise waveform and this is difficult to detect. Anti-jamming and low probability of intercept capabilities are due to the random nature of the signal. White noise is independent and uncorrelated, therefore a correlation receiver can pick up the noise waveform despite the presence of any additional interference or background noise. In addition to this, because noise is uncorrelated, multiple noise radars can operate at the same time and over the same frequency bandwidth without interfering with each other much.

The most popular method for generating a noise waveform is to heat up diodes and amplify their thermal noise. Filters are then used to achieve the desired noise bandwidth. Another method is to use arbitrary waveform generators (AWGs) to produce a noise waveform. Using an AWG costs more than amplifying thermal noise; however, if you wish to adapt your noise waveform, an AWG allows for more flexibility in selecting the bandwidth.

In order to measure Doppler frequency shifts from targets that are moving, a noise signal alone is not appropriate. Doppler measurements rely on comparing the phase of the transmitted and received signals and a noise waveform does not have any measurable phase. In order to detect Doppler, a single CW tone is

embedded within the noise waveform. By embedding this tone within the noise waveform, covertness is maintained and the radar can now detect Doppler from human movements. The term micro-Doppler is used to refer to signals where there are additional, time-varying components in the Doppler signal in addition to Doppler that arises from translational movement. Micro-Doppler is produced by target vibrations and rotations. Over the past 15 years, both the theoretical and experimental aspects of micro-Doppler have been investigated. The primary focus of past research has been on human gait and simple vibrating and rotating targets such as cylinders [2, 5, 11, 12, 13, 14, 15].

Others have performed research on vital signs monitoring with micro-Doppler radar. Sasan Bakhtiari has built a 94 GHz sensor for the monitoring of vital signs. His work resulted in a system that was capable of remotely monitoring human vital signs such as respiration and heart beat by measuring the displacement of the target's chest [16, 17]. David Tahmoush and Victor Lubecke are two other researchers who have also worked in this area [18, 19, 20]. Previous work has been constrained to cooperative targets, where the human target is seated or laying down. This allows breathing or heartbeat signals to be detected more easily, whereas if the person is standing, additional movements will obscure the vital signs signals.

In addition to studying micro-Doppler signatures due to human gait or vital signs. Some work has been performed on the classification of human gait signatures. This work has been primarily by Hao Ling. In his work, Ling has human targets perform various gait movements such as walking, running, crawling, etc. He is able to accurately classify the type of movement using micro-Doppler signatures [2].

One other area of interest that will be discussed in this dissertation is the bistatic micro-Doppler effect and also the use of multiple sensors for determining the orientation of oscillating targets. Some previous work with bistatic Doppler has been performed by various researchers and here, many of these concepts will be built upon. Additionally, bistatic micro-Doppler radar and multiple sensors can be employed for the classification of human micro-Doppler signatures.

The remainder of this dissertation is organized as follows. Chapter 2 describes background material on radar design principles, the attenuation of electromagnetic waves through wall materials, the Doppler frequency shift, the effects a wall bar-

rier has on Doppler signals, and a summary of previous work with micro-Doppler signatures. These works focus on human gait and some animal signatures, with which we are not as concerned. We are primarily concerned with human targets that do not have a translational velocity due to their desire to remain concealed, but still exhibit small micro-motions. Chapter 3 describes the S-band radar in detail and Chapter 4 describes the mm-wave radar in detail. Chapter 5 discusses commonly used time-frequency transforms and also the Hilbert-Huang transform and Empirical Mode Decomposition, which play a prominent role in the algorithm for classification of human gestures. Chapter 6 describes in detail simulations of human gestures of interest and compares the simulated micro-Doppler signatures to experimentally measured micro-Doppler signatures using both the S-band and mm-wave radars. Chapter 7 describes the human activity classification algorithm in detail. Chapter 8 discusses the effect of modifying the EMD stopping criteria on the classification results and also on the time that it takes to complete EMD and classification. Chapter 9 describes work that has been done to expand the micro-Doppler signature work to multiple sensors. Chapter 10 summarizes the conclusions and puts forth some recommendations for future work.

Chapter 2

Background

2.1 Noise Radar

2.1.1 Radar Basics

Radar systems operate on the basic principle of transmitting an electromagnetic wave and detecting the electromagnetic wave that is backscattered off of a target. The radar transmits an electromagnetic wave, receives the backscatter from the target, and processes the reflected signal to extract information about the target. Among the important design considerations for any radar is the selection of frequency, bandwidth, transmit power, and the type of waveform to transmit. Waveform design is a broad area, which involves selecting the best transmit waveform for a given application. Radar systems can transmit continuously or they can transmit short pulses. They can transmit a single frequency or a wide band of frequencies. For this system, a continuously transmitted noise waveform has been chosen for its covertness and the desirable properties of low probability of intercept and anti-jamming. A single frequency CW tone is embedded within the noise waveform for Doppler detection. Our approach involves generating this composite noise-plus-single-tone signal at low frequencies and mixing up to a higher frequency. Another consideration for radar systems is the location and number of transmitters and receivers. Many radars share a single antenna for transmitting and receiving and are called monostatic radars. These radars often transmit short pulses so that a circulator and switches can be used to select either the transmit chain or the

receive chain to turn on. In cases where the transmit and receive antennas are not co-located, the radar is said to be operating in a bistatic configuration. Because our radar sensor is intended to be mounted on small arms weapons, a bistatic configuration cannot be utilized. In addition to this, a monostatic configuration also cannot be used because the noise waveform is transmitted continuously and will leak into the receive chain, causing saturation of the receiver. To remedy this, a quasi-monostatic configuration is used. This means that the radar uses separate antennas for transmitting and receiving, which are closely spaced. For all intents and purposes, this configuration acts exactly like a monostatic radar.

The most fundamental and well-known equation for radar is the Radar Range Equation (RRE). The RRE has many forms, but most common form is shown in Equation 2.1 [21].

$$P_r = \frac{P_t G_t G_r \lambda^2 \sigma}{(4\pi)^3 R^4 L} \tag{2.1}$$

Here, P_t is the transmitted power, P_r is the received power, G_t is the gain of the transmit antenna, G_r is the gain of the receiving antenna, λ is the wavelength of the transmit waveform, σ is the target's radar cross section (RCS), R is the range to the target, and L represents additional losses/gains that the radar may experience. These additional losses/gains include atmospheric attenuation, attenuation due to penetration through materials, or signal processing gain.

2.1.2 Range Resolution

Another important radar equation is the equation for range resolution. This describes how closely two targets can be placed and still be detected by the radar as two separate targets. If the targets are spaced closer than the range resolution, the radar detects them as a single target. For a single frequency, pulsed radar the range resolution is:

$$\Delta R = \frac{c\tau}{2} \tag{2.2}$$

where c is the speed of light and τ is the pulse width (in seconds) of the transmit waveform [21]. The range resolution from a single frequency pulsed radar is

generally large, so by transmitting a wide bandwidth, the range resolution can be improved. The range resolution for a wideband waveform is:

$$\Delta R = \frac{c}{2B} \tag{2.3}$$

where B is the bandwidth of the waveform.

2.1.3 Target Ranging and Matched Filtering

In order to determine the target range using a noise waveform, a matched filter receiver must be used. Essentially, a matched filter receiver measures the similarity between two signals and for a noise radar is identical to cross correlation between the received signal and a stored copy of the transmitted signal. Because we are using a random noise signal, it will not correlate strongly with any other signals except for itself. Matched filtering can be done in either hardware or software, but software implementation is most common. To implement matched filtering in hardware, a mixer and a low-pass filter are used [22]. To implement matched filtering in software, a copy of the transmitted noise waveform is digitized and saved. The received signal is also digitized and saved. The two waveforms are multiplied together and averaged. Then, the transmit waveform is delayed by one sample and the process is repeated. This is done repeatedly for all delay values until the two waveforms no longer overlap. The time delay can then be related to the range to the target using $R = \frac{c\tau}{2}$, where c is the speed of light and τ is the time delay. The result is the range profile for the noise radar. Large amplitude peaks in the range profile correspond to target locations because, at those delays, the two waveforms are scaled copies of each other.

The matched filter receiver can be expressed mathematically and is briefly described now [21]. The matched filter is represented by $h(t)$ in the time domain and $H(\omega)$ in the frequency domain. The received signal is represented by $x(t)$ and $X(\omega)$ in the time and frequency domains respectively. The matched filter output is represented by $y(t)$.

The filtering process can be represented mathematically in the frequency domain by multiplication, so

$$Y(\omega) = X(\omega) \times H(\omega). \tag{2.4}$$

Taking the inverse Fourier transform of this Equation produces the matched filter output in the time domain:

$$y(t) = \frac{1}{2\pi} \int b \exp(j\phi) X(\omega) \exp(-j\omega t_d) H(\omega) \exp(j\omega t), \tag{2.5}$$

where $b \exp(j\phi) X(\omega) \exp(-j\omega t_d)$ is the spectrum of the received signal that is backscattered from a point target, t_d is the time delay, b is the amplitude of the received signal, and ϕ is the measured phase of the received signal. There is also thermal noise that is present in the received signal. Here we assume this to be white Gaussian noise, so the power spectrum (N_0) is constant across all frequencies. The expected value of the noise after filtering is then given by:

$$E[n^2(t)] = \frac{N_0}{2\pi} \int |H(\omega)|^2 d\omega \tag{2.6}$$

and the output of the matched filter (without noise) at time t_d is:

$$y(t_d) = \frac{b \exp(\phi t)}{2\pi} \int X(\omega) H(\omega) d\omega. \tag{2.7}$$

The matched filter is selected to maximize the signal to noise ratio at the output of the filter, so

$$SNR = \frac{b^2 |\int X(\omega) H(\omega) d\omega|^2}{2\pi N_0 \int |H(\omega)|^2 d\omega} \tag{2.8}$$

The Schwartz inequality is then applied to the numerator, yielding:

$$\left| \int X(\omega) H(\omega) d\omega \right|^2 \leq \int |X(\omega)|^2 d\omega \int |H(\omega)|^2 d\omega. \tag{2.9}$$

In order to maximize the SNR, we must have equality in Equation 2.9 and this means that $H(\omega) = aX^*(\omega)$ or $h(t) = ax^*(-t)$, where a is an arbitrary scaling factor. This means the matched filtering process is equivalent to the cross correlation of the received signal with a delayed copy of the transmit signal [21].

2.2 Doppler

When an electromagnetic wave is scattered off of a moving target, the initial frequency of the electromagnetic wave is shifted by an amount that is directly proportional to the velocity of the target and is inversely proportional to the initial frequency of the electromagnetic wave. The Doppler equation is given by Equation 2.10. Another form of the Doppler equation relates the phase of the backscattered signal to the time-varying range to the target. This form is given by Equation 2.11.

$$f_d(t) = \frac{2v(t)}{\lambda} \tag{2.10}$$

$$\varphi_d(t) = \frac{4\pi r(t)}{\lambda} \tag{2.11}$$

In the equations above, v is the radial velocity of the target, λ is the wavelength of transmitted signal, and r is the radial range to the target. Because the Doppler shift is measured by the phase difference between the transmitted and received signals, noise waveforms are not well-suited for Doppler processing.

Any movement by the target will produce a shift in frequency and often different locations along a target produce different Doppler shifts. This results in a complex return Doppler signal. This is evident in human motions, where the torso, arms, legs, and head all move at different velocities and thus, produce different Doppler shifts. In addition to this, each location along the arms will be moving at different velocities, which only adds to the complexity of the returned Doppler signal. Because the Doppler shift depends on wavelength, higher frequency transmit waveforms will produce larger Doppler shifts. This means that higher frequencies will allow more detail to be observed in the micro-Doppler signature. This will be clearly demonstrated later in this dissertation.

The noise waveforms that we use for target ranging have the desired properties of covertness, anti-jamming, and low probability of intercept; however, white Gaussian noise waveforms do not have a measurable phase. Thus, CW radars are ideal for Doppler processing because their phase can be easily ascertained and compared to the received signal.

2.3 Through-the-Wall Radar Considerations

Due to the very nature of electromagnetic propagation through various types of media, through-the-wall sensing poses additional challenges that must be considered and overcome in the design of any through-the-wall radar system. Micro-Doppler radars are no exception to these challenges. Once the radar has been designed appropriately, the limitations imposed by the wall barrier can be minimized and a through-wall micro-Doppler radar system can be operated in much the same manner as a barrier-free radar system. Some of the considerations that must be taken into account include reflections from the front and back faces of the wall (and possibly resonant cavities within the wall), attenuation of electromagnetic waves through different materials, and the dispersive characteristics of the media.

It is well established that higher frequencies exhibit much larger losses than lower frequencies. For this reason through-wall radars typically operate at frequencies of 5 GHz or less. Wall losses also reduce the signal-to-noise ratio of the radar returns, thus limiting the maximum range of the radar. This also means that some walls may induce too great a loss to detect some targets due to their material properties or simply because of the thickness of the wall itself.

The electromagnetic properties of building materials are critical in through-the-wall radar design and data analysis. Attenuation, dispersion, reflection, and refraction all are important considerations when dealing with through-wall micro-Doppler signatures. The type of building material may not pose a considerable challenge if it is wood, glass, or drywall where the attenuation is relatively small. On the other hand, materials such as concrete, cinder block, or brick may cause significant attenuation of the signal to the point where the signal cannot be detected. As we would expect, the material properties are frequency dependent, therefore selecting appropriate frequencies will alleviate some of the challenges that arise due to barrier effects.

2.3.1 Wall Attenuation

The attenuation of electromagnetic waves through materials depends on the material properties of the material. The permittivity (ϵ), permeability (μ), and conductivity (σ) all vary depending on the type of material in question and they also

vary depending on the frequency of the incident wave. If these material properties are known, then the attenuation constant can be approximated as:

$$\alpha = \frac{\sigma}{2}\sqrt{\frac{\mu}{\epsilon}}. \tag{2.12}$$

Here we are assuming that the wall is made of a dielectric material because conducting walls act as opaque barriers for through-the-wall radars. Often, the loss tangent ($\tan\delta$) is reported instead of the attenuation constant, where $\delta = \frac{1}{\alpha}$. Because ϵ and σ are frequency dependent, the attenuation constant is also frequency dependent. Table 2.1 shows the attenuation as measured experimentally in [7] for some selected materials at 100 MHz. Table 2.2 shows the attenuation measured experimentally in [8] for some common wall materials at 500 MHz. Because the loss increases as the frequency increases, through-the-wall radars are limited to lower frequencies. The loss that is encountered may not be significant for many materials; however, when considering a material such as concrete or cinder block the loss can have a crippling effect on the received power by the radar. It is also important to remember that the losses that are reported in Table 2.1 are one-way loss factors. The loss experienced by the radar system is two-way and the loss factor must be doubled.

A more complete plot of the attenuation through various materials at frequencies ranging from 4 GHz to 100 GHz is shown in Figure 2.1 [1]. Because through-wall radars are often desired to work in worst-case scenarios, the radar operating frequency is chosen to be less than 5 GHz so that the total attenuation due to 2-way propagation through concrete block is less than 15 dB.

Table 2.1: Attenuation and relative permittivity of some selected materials at 100 MHz [7].

Material	Attenuation (α in dBm^{-1})	Relative permittivity (ϵ_r)
Air	0	1
Asphalt	2-15	2-4
Dry Concrete	2-12	4-10
Wet Concrete	10-25	10-20
Sandy dry soil	0.1-2	4-6
Sandy wet soil	1-5	15-30

Table 2.2: Attenuation of typical wall materials at 500 MHz [8].

Wall	2-Way Attenuation (dB)
Typical Interior Wall (two 1/2-in. gypsum panels filled with wood)	8
Reinforced concrete wall (6-in. deKhotinsky concrete with 1/2-in. rebar on 3-ft. centers)	11
Stucco/concrete wall (1-in. 22AWG chicken-wire with 1/2-in. concrete)	19
Chain-link (cyclone) fence	11

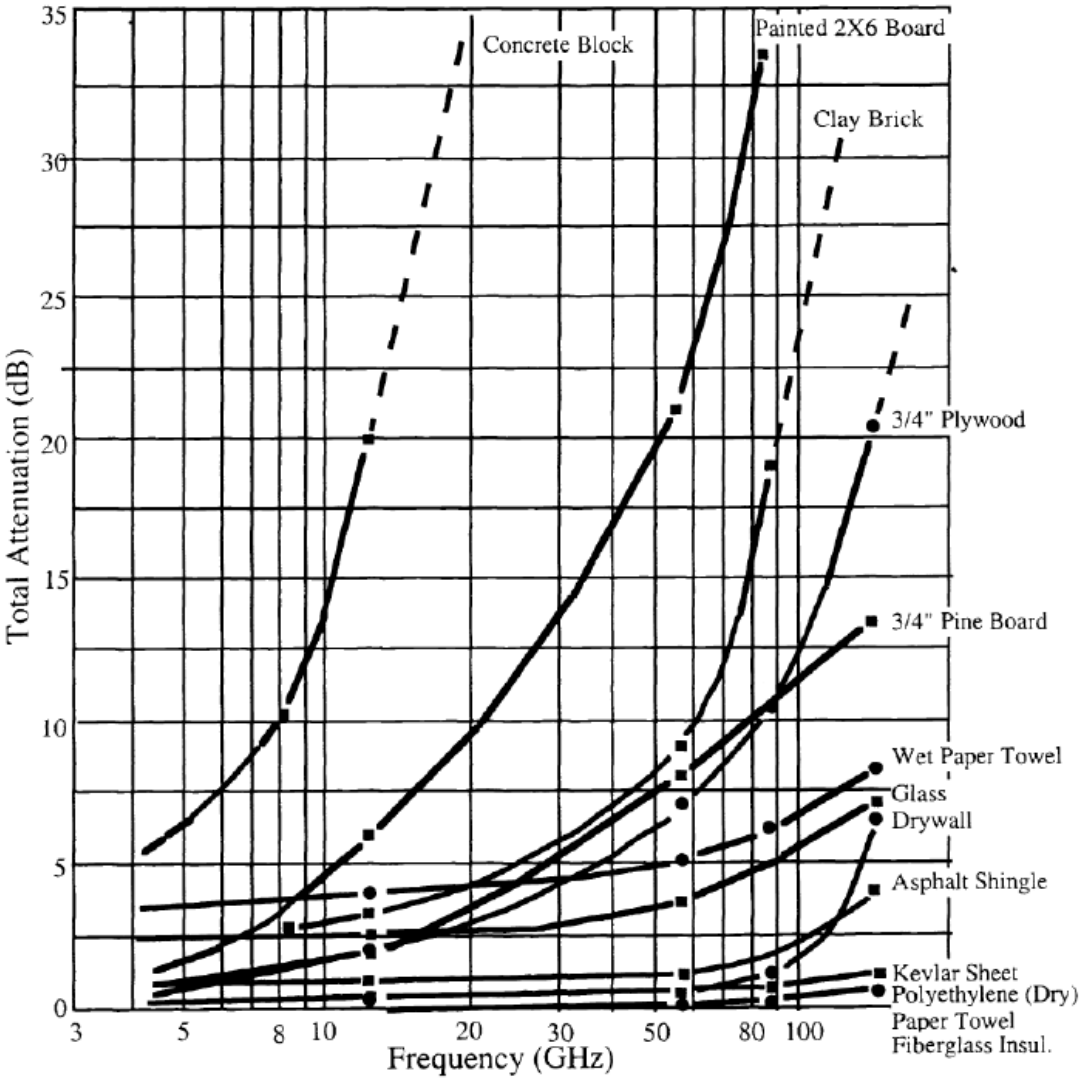

Figure 2.1: One-way attenuation of EM waves (in dB) through various materials [1].

Additional measurements by [23] for 20 cm thick concrete and wooden walls at a frequency of 2.4 GHz show a transmission loss at the air-wall interface of 3.9 dB and 0.9 dB, respectively. The through-wall propagation loss was found to be 1.2 dB and 0.7 dB for 20 cm thick concrete and wooden walls, respectively. Many other resources can be found which discuss attenuation through wall materials. A sampling of some of these resources can be found in [24, 25, 26].

2.3.2 Wall Reflection

As discussed in the previous section, the material properties determine the loss due to propagation through lossy media, such as a wall. These same material properties are responsible for reflecting part of the incident wave back to the radar without penetrating the wall. The reflections are caused by the discontinuity in the intrinsic impedance of the material through which the wave is traveling. The reflection coefficient Γ and the transmission coefficient T (assuming normal incidence) for a wave traveling from Medium 1 into Medium 2 are well known and are given in Equations (2.13) and (2.14) respectively, where $\eta = \sqrt{\frac{j\omega\mu}{\sigma+j\omega\varepsilon}}$ is the material intrinsic impedance. Because transmission through conductive materials is not practical due to high losses, we can assume that the wall material is a good dielectric, for which the intrinsic impedance can be approximated as $\eta \approx \sqrt{\frac{\mu}{\varepsilon}}$.

$$\Gamma = \frac{\eta_2 - \eta_1}{\eta_1 + \eta_2} \tag{2.13}$$

$$T = \frac{2\eta_2}{\eta_1 + \eta_2} = 1 + \Gamma \tag{2.14}$$

The average reflected and transmitted power densities S^r_{avg} and S^t_{avg}, respectively are given by:

$$|S^r_{avg}| = |\Gamma|^2 S^i_{avg} \tag{2.15}$$

and

$$|S^t_{avg}| = (1 - |\Gamma|^2) S^i_{avg}. \tag{2.16}$$

Because a large fraction of the power is reflected and never reaches the other side of the wall, reflections are another source of losses in through-wall radars.

2.3.3 Dispersion

Many Doppler radars utilize a CW wave that consists of a single frequency. For these radars, dispersion obviously does not play a role. However, for pulsed Doppler, multi-frequency, or ultra wideband (UWB) radars, dispersion can have

some degrading effects on radar performance. Dispersion is caused because the individual dipoles created by an induced electric field take some small amount of time to align themselves in the direction of the electric field. In the presence of an oscillating electric field, the response time of the dipoles will depend on the frequency of the electric field oscillations. This will cause the different frequency components of a UWB signal to travel at different speeds. Because of this, dispersive media will have the effect of broadening pulses and distorting the signal. The broadening of the pulse will effectively decrease the signal bandwidth.

Most materials can be assumed to follow classical models such as the well-known Debeye equation. This model can be used to calculate the complex permittivity as a function of frequency. Using the Debeye equation, the complex permittivity of a material is:

$$\dot{\varepsilon_r}'(\omega) = \varepsilon_r'(\omega) - j\varepsilon_r''(\omega) = \varepsilon_{r\infty}' + \frac{\varepsilon_{rs}' - \varepsilon_{r\infty}'}{1 + j\omega\tau_e} \tag{2.17}$$

where ε_{rs}' and $\varepsilon_{r\infty}'$ are the real parts of the complex permittivity at zero frequency and at a very large frequency (optical frequency), respectively, and τ_e is a new relaxation time constant that is related to the original relaxation time constant τ by

$$\tau_e = \tau \frac{\varepsilon_{rs}' + 2}{\varepsilon_{r\infty}' + 2} \tag{2.18}$$

For a more complete and thorough discussion of dispersion, including the Lorentz model, which accounts for multiple resonances, see [27, 28]. (The Debeye model only accounts for a single resonance). Our through-wall radar performs well despite the fact that we did not counteract dispersive effects. This demonstrates that, even if the signal is slightly distorted due to a wall barrier, noise waveforms still correlated well.

2.3.4 Signal-to-Noise Ratio and Maximum Detectable Range

As with all radar systems, micro-Doppler radars have a maximum detectable range that depends on SNR. Because of the attenuation that electromagnetic waves experience when traveling through wall materials, the SNR will decrease and thus

decreasing the maximum detectable range of a micro-Doppler radar. Equation (2.19) shows the radar range equation in a form that shows the maximum detection range at which a target with a given RCS can be detected with a given SNR.

$$R_{max} = \left[\frac{P_t G_t G_r \lambda^2 \sigma}{(4\pi)^3 \mathrm{SNR}_{min} L} \right]^{1/4}. \tag{2.19}$$

In Equation (2.19), P_t is the transmit power, G_t is the gain of the transmitting antenna, G_r is the gain of the receiving antenna, λ is the wavelength, σ is the Radar Cross Section (RCS), and SNR is the signal-to-noise ratio. Here all of the losses from wall attenuation are included in $L \geq 1$. This means that the maximum detectable range of the radar will decrease significantly as L increases. However, due to reflections, not all of the power is transmitted through the wall, so Equation (2.19) must be modified according to the transmission power from Equation (2.16). Because of 2-way transmission, Equation (2.19) becomes:

$$R_{max} = \left[\frac{P_t G_t G_r \lambda^2 \sigma \left(1 - |\Gamma|^2\right)^2}{(4\pi)^3 SNR_{min} L} \right]^{1/4}. \tag{2.20}$$

As an example, let us consider a two-way wall loss of 20 dB and a maximum range of 50 meters when operating in an environment without a wall ($L = 1$). For now, neglect the effect of wall reflections and only consider wall losses. A 20 dB wall attenuation is a loss factor of 100 and will decrease our maximum range by a factor of $(1/100)^{1/4} = 1/\sqrt{10} \approx 0.32$. This means that our radar can only detect targets up to a range of $50 \times 0.32 = 15.8$ meters. At higher frequencies for materials such as concrete, cinder block, or brick, the losses may be significant enough that it is impossible to detect micro-Doppler signals at any distance.

The distances from the radar to the wall and from the radar to the target are also important. Using our previous example, suppose that the wall is located at 20 meters from the radar. This would mean that it is necessary for the target to be in front of the wall in order to detect the micro-Doppler. In this case the wall no longer has an effect and the wall losses are irrelevant.

Now, let us consider a target that is located 10 meters behind a wall. The

two-way wall loss is again 20 dB. In order to detect this object, the radar must be located closer than 5.8 meters from the wall. This ensures that the target is within the maximum detectable range of 15.8 meters.

Figure 2.2 illustrates the effect of attenuation on the maximum range. It is clear that the maximum range is halved for every additional 12 dB of loss.

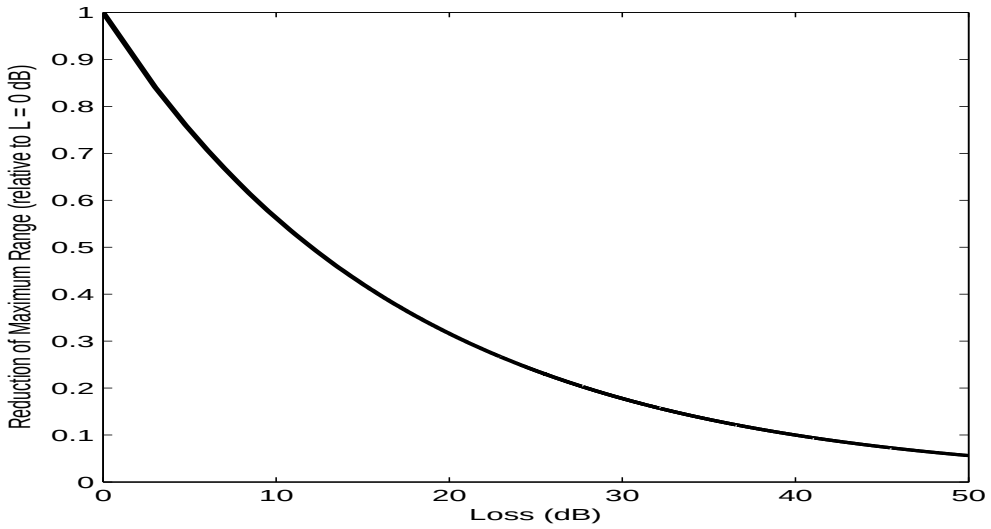

Figure 2.2: Maximum detectable range for a given loss (relative to $L = 1$).

As another example, consider the first scenario once again, except we will now include a reflection coefficient of $|\Gamma| = 0.5$. The $\left(1 - |\Gamma|^2\right)^2$ term is equal to 0.5625, which corresponds to an additional 2.5 dB of loss. Figure 2.3 illustrates the effect of the wall reflections on maximum range. Larger values for the magnitude of Γ will increase the loss significantly and if we have a perfect conductor ($|\Gamma| = 1$) then, as should be expected, the target cannot be detected.

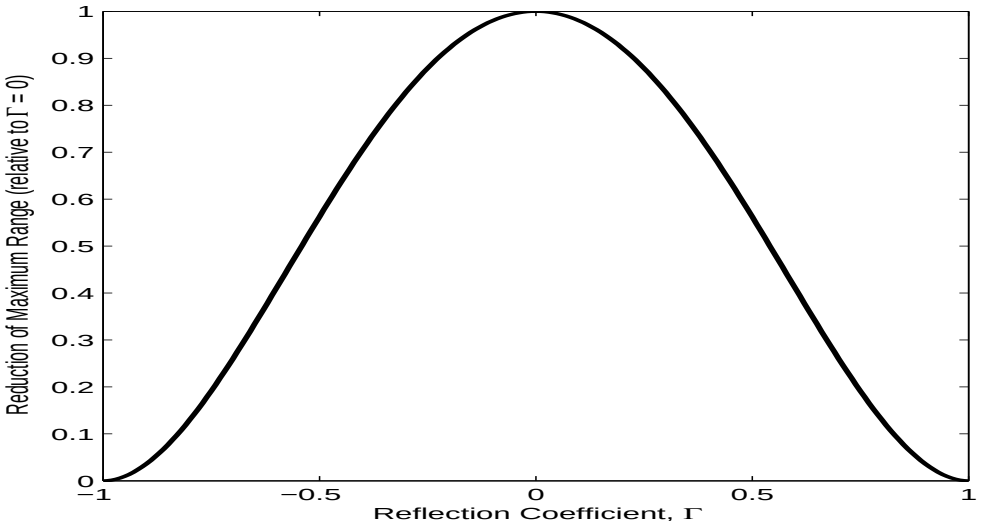

Figure 2.3: Maximum detectable range versus Γ.

2.3.5 Wall Effects on Micro-Doppler Signatures

As discussed in Chapter 2, electromagnetic waves that travel through media will experience the effects of attenuation, dispersion, and limitations on the maximum range. These effects are non-specific to micro-Doppler signatures. Aside from these effects, a constant phase offset occurs because of the stationary wall.

2.3.5.1 Constant Phase Offset

The familiar expression for the Doppler frequency shift and Doppler phase shift are shown in Equations 2.10 and 2.11 respectively.

Each scatterer in the radar beam will introduce a component to the total received radar signal, some of which will have a micro-Doppler component and some of which will not. If, for simplicity, we assume a single frequency continuous wave Doppler radar system and that the received radar signal consists of only two components, one from a wall and another from an object that exhibits micro-Doppler motion, the received signal can be expressed as:

$$r_x(t) = a_{wall}\cos\left[2\pi f_c t + \varphi_{wall}\right] + a_{obj}(t)\cos\left[2\pi f_c t + \varphi_{obj}(t)\right]. \tag{2.21}$$

where a_{wall} and a_{obj} are the amplitudes of the received component due to the wall and the moving object respectively, φ_{wall} and φ_{obj} are the phase shifts due to the path lengths to the wall and the object respectively, and f_c is the transmitted frequency.

Because the range to the wall is constant, it does not produce a time-varying phase shift. Conversely, the object that exhibits micro-Doppler motion will have a range to the target, $r(t)$ that will vary with time and therefore the Doppler phase shift will vary with time. In addition to this, the amplitude of the wall will not vary with time because its RCS remains constant. The amplitude of the object, however, will generally vary with time because its RCS will depend on its orientation relative to the radar. Typically the carrier signal is removed via frequency mixing and filtering, which will simplify Equation (2.21) to:

$$r_x(t) = a_{wall}\cos\left(\varphi_{wall}\right) + a_{obj}(t)\cos\left(\varphi_{obj}(t)\right). \tag{2.22}$$

The first term of Equation (2.22) shows that there will be a DC component present in the micro-Doppler signature because of the wall. This DC component depends on the magnitude of the wall component and also on the distance to the wall as a fraction of the carrier wavelength. Because the phase can be represented by Equation (2.11) and because the cosine function repeats every 2π, the DC offset will repeat when the distance from the radar to the wall is a multiple of $\lambda/2$. This is illustrated in Figure 2.4 and experimentally verified by measurements shown in Figure 2.5. Because the wavelength for the experiments was small (on the order of a couple of centimeters) it was very difficult to measure the exact distance to the wall and led to some error in the measurements; however, these experiments show that the phenomenon of a constant offset due to a stationary barrier will have an effect on the radar micro-Doppler returns. Based on Figure 2.4, the DC offset should achieve negative values for some distances. This is not the case in Figure 2.5 and this is due to antenna coupling and other additional components. In the development of the theoretical DC offset, only a single constant phase term was considered for simplicity. In general, this is not realistic. In practical measurements, multipath, antenna coupling, and clutter will all produce constant phase terms contributing to the DC offset. In Figure 2.5 the combined DC value of the other components caused the DC offset to remain positive for all

but a single distance to the wall. It should also be noted that if a target exhibits micro-motions, but is otherwise remaining stationary, the distance to the target can be expressed as: $R_0 + r(t)$. This constant distance will also produce a constant DC term, which will add together with the wall's DC component.

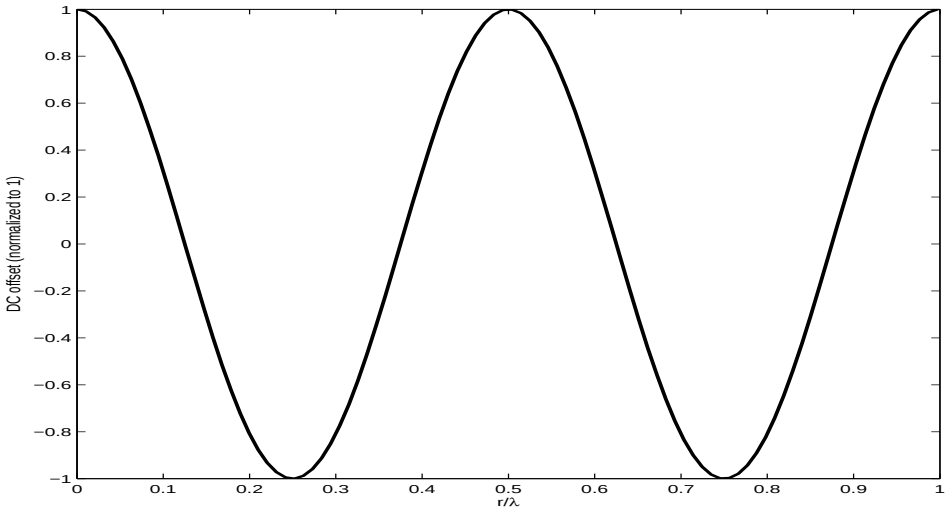

Figure 2.4: Theoretical DC offset versus range to the wall as a fraction of λ.

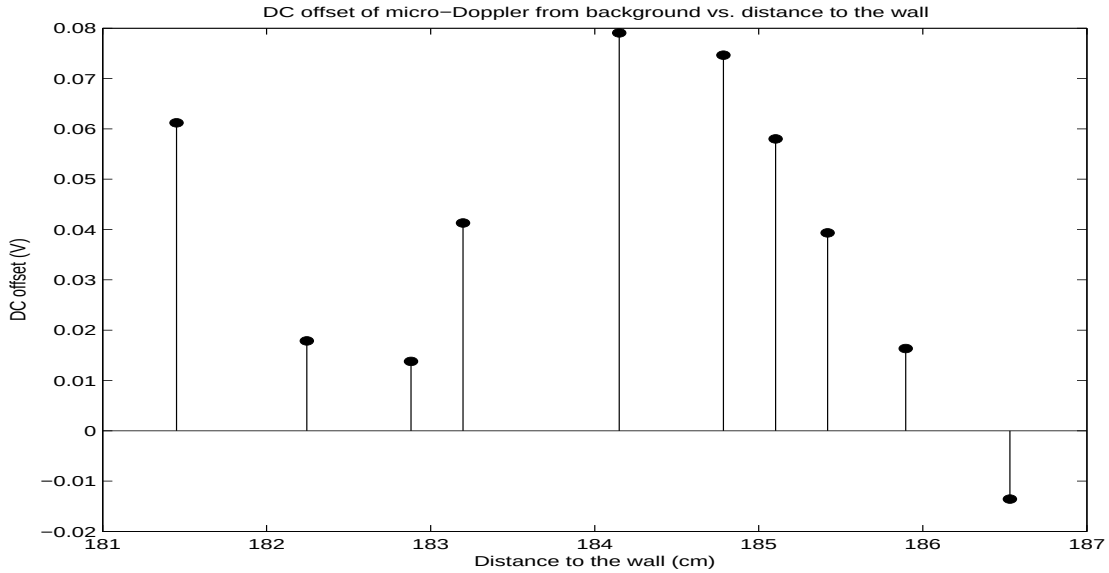

Figure 2.5: Experimental DC offset versus range to the wall as a fraction of λ.

The DC component does not have a great effect on the micro-Doppler signature; however, when viewing the signal using a time-frequency representation, low frequency signals may be obscured by a very strong, constant DC offset. This can be remedied by simply subtracting the DC offset from the signal.

2.4 Micro-Doppler Signals of Targets with a Translational Velocity

Some common applications of micro-Doppler radar include identification of signatures from human gait, vehicles, and animals. If vehicles or animals are to be considered, in many cases a through-wall environment is not considered. However, in some cases it may be desirable to sense objects in an outdoor environment from within a building. In these cases, a through-wall environment is applicable.

Under normal circumstances, vehicle micro-Doppler will include some translational velocity, in which case the micro-Doppler will be centered around the constant Doppler frequency that arises from the translational motion. This is also true for human gait, where the translational velocity of the human will shift the micro-Doppler from the legs, arms, etc. away from being centered at DC.

In the case of a signal with a constant translational velocity combined with a micro-Doppler frequency component, the radar received signal can be simulated as:

$$x_r(t) = a(t)\cos\left(2\pi f_c t + 2\pi f_{d0} t + \varphi(t)\right). \tag{2.23}$$

where $a(t)$ is the time-varying amplitude of the received signal, f_c is the carrier frequency of the transmitted wave, f_{d0} is the Doppler frequency shift of the target's constant velocity, and φ is the time-varying micro-Doppler phase shift that is produced by micro-motions (vibrations and rotations) of the target. As was the case in Section 2.3.5, the carrier is usually removed and the micro-Doppler signature is:

$$x_r(t) = a(t)\cos\left(2\pi f_{d0} t + \varphi(t)\right). \tag{2.24}$$

Here the constant velocity produces a constant frequency according to Equation

(2.10) in addition to a micro-Doppler component with a time-varying phase.

2.4.1 Walking Humans

A common area of current research is in the analysis and identification of human gait movements. The motion of walking is a complex motion that consists of many different components, all of which are moving in sync with other parts of the body. An example of the micro-Doppler signature of a human walking is described in [3]. The micro-Doppler of a human walking toward a radar and moving from about 8 meters from the radar to about 2 meters from the radar is shown in Figure 2.6 [2]. This time-frequency representation shows a strong response from the torso and weaker responses due to the arms and legs. The torso is restricted to a small bandwidth, whereas the arms and legs exhibit larger Doppler shifts. The mean frequency of the walking signature is shifted in the positive direction, indicating a translational velocity toward the radar.

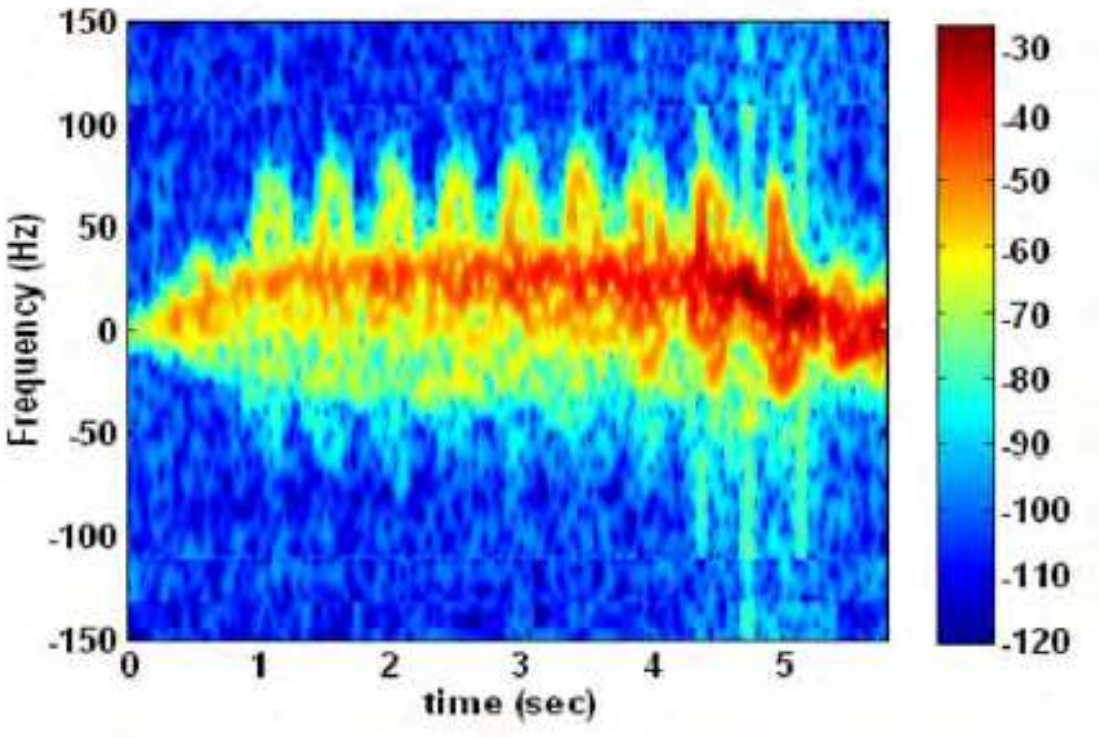

Figure 2.6: Spectrogram of a human walking toward a radar [2].

In [29], the human walking movement is simulated. This simulation is shown in Figure 2.7 and clearly shows some of the distinct Doppler traces that arise from each moving part of the body (left toe, left ankle, torso, right ankle, right toe, etc.).

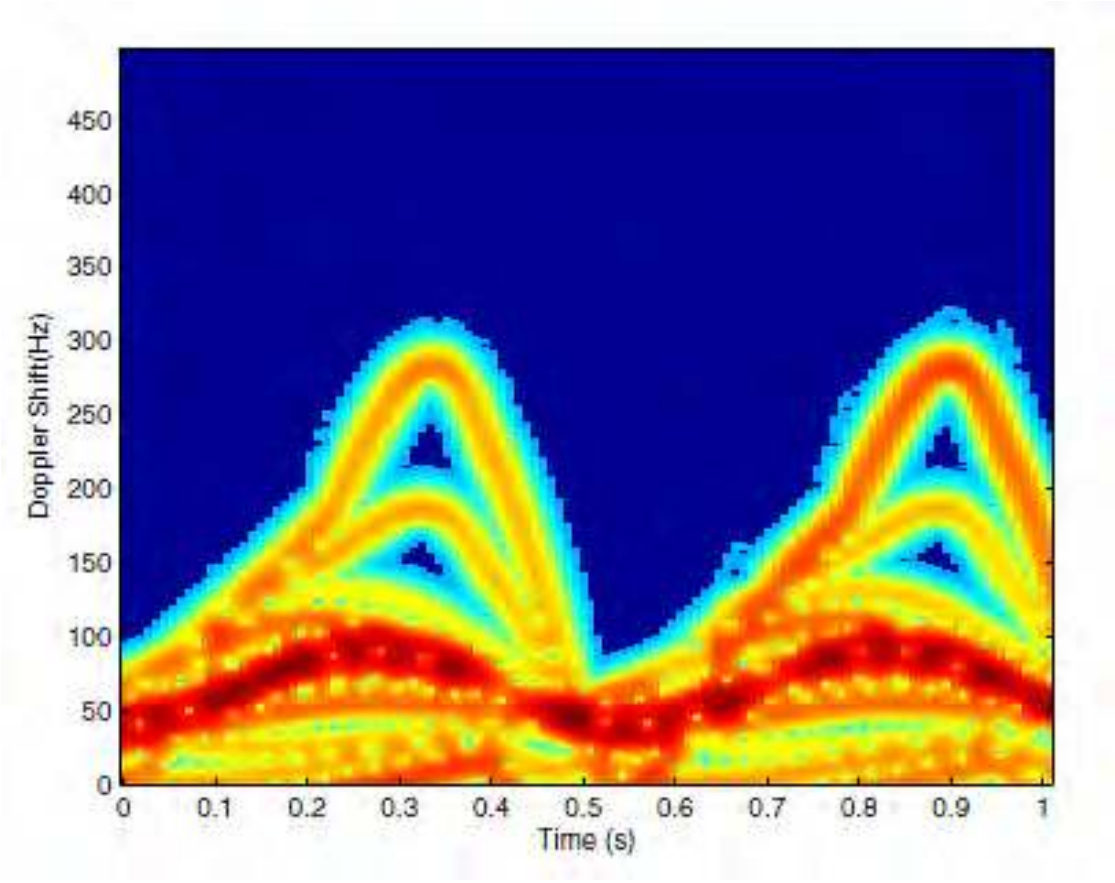

Figure 2.7: Spectrogram of a human walking toward a radar [3].

Figure 2.8 shows a human walking toward a non-coherent micro-Doppler radar operating in the S-Band. The person was located behind a 4-inch thick brick wall. Because the radar is non-coherent, only positive frequencies can be observed. Nonetheless, many of the same features can be clearly seen in the time-frequency representation of the walking signal and, in fact, the walking signature appears very similar to the walking signature of Figure 2.6 that was reported in [2].

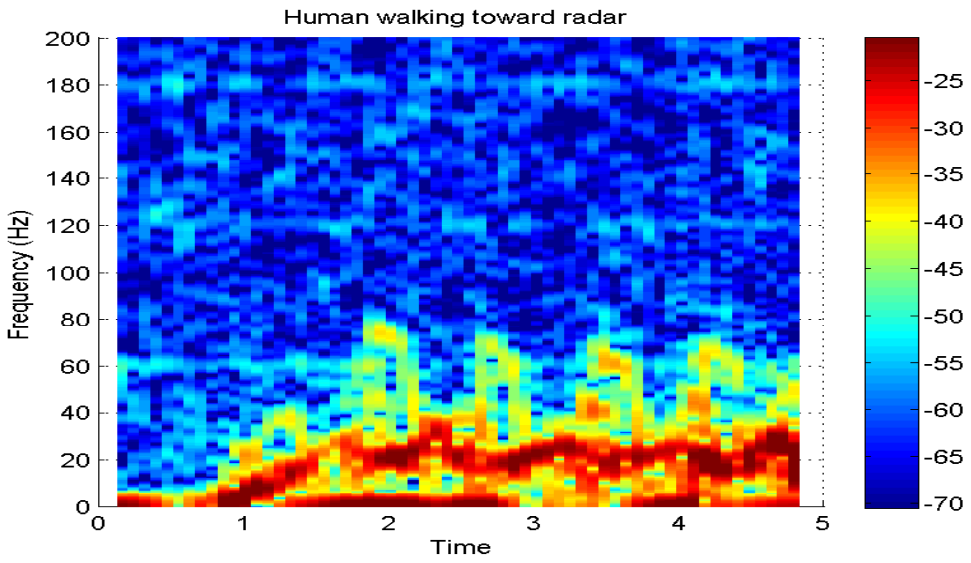

Figure 2.8: Spectrogram of a human walking using an S-band, non-coherent, micro-Doppler radar.

For additional information with more detail on human gait micro-Doppler, see [2, 3, 11, 30, 31, 32, 29].

2.4.2 Animals

The ability to differentiate human signatures from the signatures of animals is another ongoing research topic. This is especially important in surveillance and security applications, where animals do not pose a threat and it is wished to ignore their signatures. Animals move in such a way that their movements are much different than that of humans. For example, consider dogs, horses, and birds. Dogs and horses both walk on four legs and birds have wings. These micro-Doppler signatures are all much different than human movements and in fact, the motions of dogs and horses are also different from each other (albeit much more subtle differences).

Below are some examples of micro-Doppler signatures due to various animals, as reported in the literature. Figure **??** shows experimentally measured micro-Doppler of a horse walking using acoustic waves [4]. The principle for measuring micro-Doppler with acoustic waves is the same as that for electromagnetic micro-Doppler except the frequency shifts are relative to the speed of sound instead of

the speed of light for radar. Figure 2.10 shows micro-Doppler of a dog (Pit Bull) walking. Figure 2.11 shows the micro-Doppler from human walking away from the acoustic system as a reference. The micro-Doppler signature from a horse exhibits a slow repetition frequency which corresponds to the stride rate of the horse. For dogs, we observe a much faster stride rate. Intuitively, this makes sense because a horse has very long legs and takes longer strides, whereas a dog has shorter legs and a faster stride rate. Both of these signatures can be distinguished from a human walking. Not only does a human being have different body part proportions, but because the animals walk on four legs, the Doppler components will be much different from that of a human [4].

The motion of a walking horse has also been simulated in [5]. This simulation is shown in Figure 2.12.

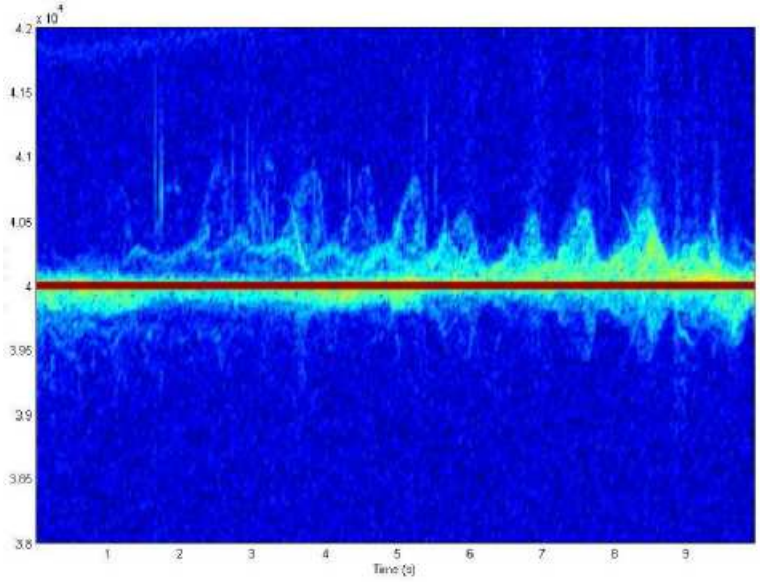

Figure 2.9: Spectrogram of a horse walking toward a Sonar [4].

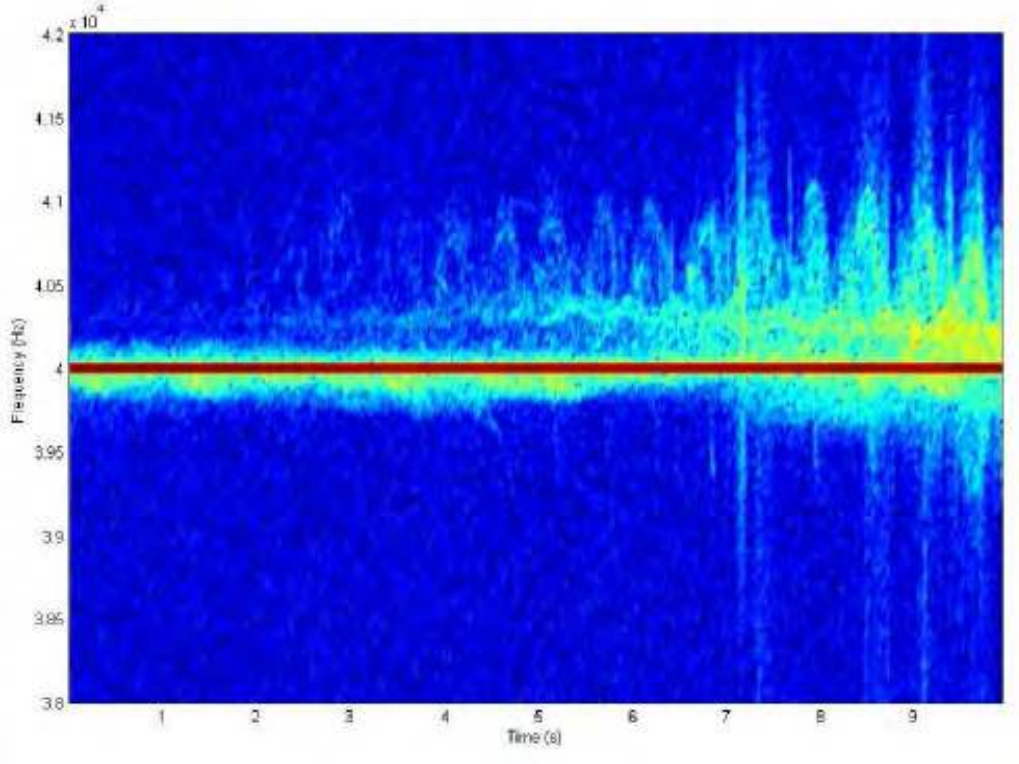

Figure 2.10: Spectrogram of a Pit Bull walking toward a Sonar [4].

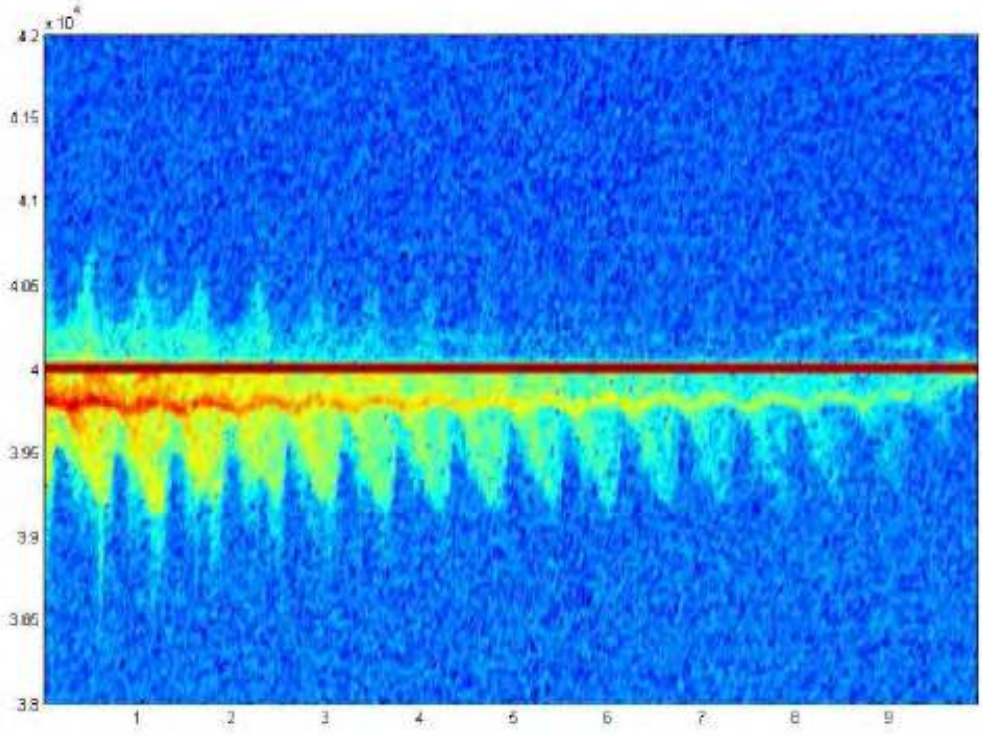

Figure 2.11: Spectrogram of a human walking away from a Sonar [4].

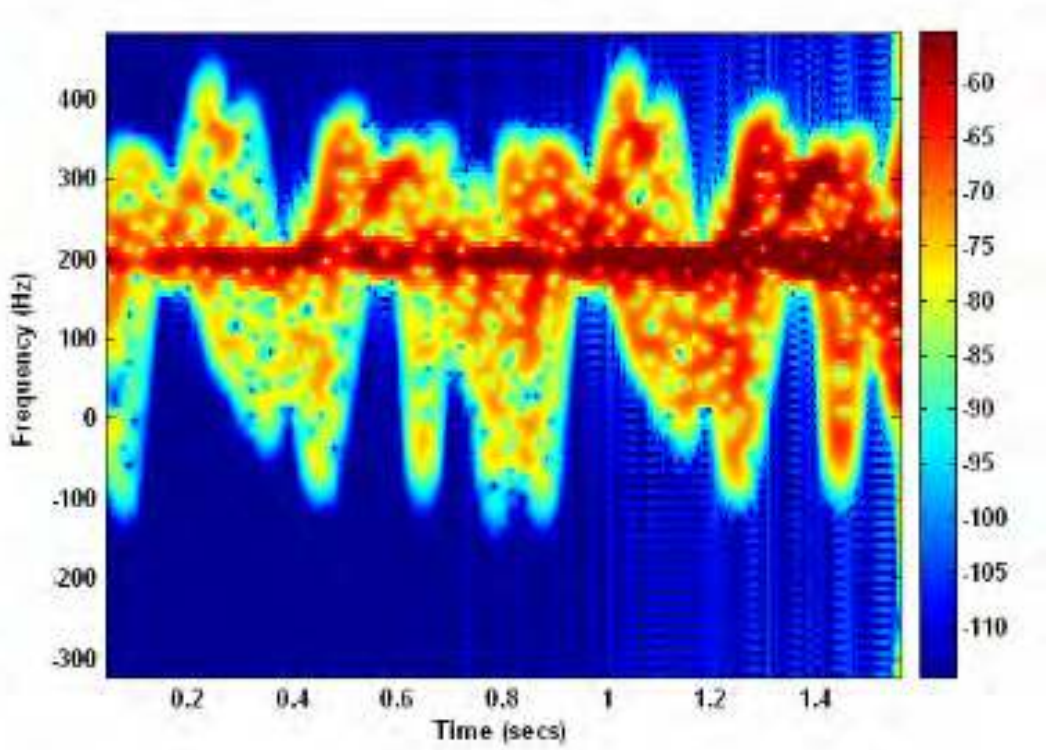

Figure 2.12: Spectrogram of a horse walking [5].

Chapter 3

S-Band Radar Design

Two separate radar systems were designed for ranging and Doppler detection of human targets. Each radar was designed with different operational environments in mind. The first radar system that I will discuss is the S-band radar. This radar system is intended for through-the-wall environments, where the target is located behind some barrier and is at close distances from the radar. To achieve signal covertness, low probability of intercept, and anti-jamming capabilities, a noise radar architecture was chosen. The noise waveform is desirable to use because it has no distinct features and is non-repeating. Because of the random nature of noise, the signal is covert, difficult to jam, and has a low probability of intercept.

3.1 Design Considerations

Because of the intended operational environment, the main design consideration is the selection of the transmitted frequency. As discussed in section 2.3.1, high frequencies experience higher loss when penetrating materials. For this reason, through-the-wall radars typically operate at frequencies less than 5 GHz. The lower the frequency, the less loss and the better the radar can range targets behind walls. Another consideration is the size of the components, specifically the size of the antennas. When operating at low frequencies, the size of the components and the antennas are large. For this reason, higher frequencies are desired to keep the size reasonable. The main reason for wanting to keep the size as small as possible is that the system should have the potential of being modified to fit onto

small arms weapons in future applications of the radar. Soldiers are limited in how much weight they can carry and adding large, bulky components will limit their maneuverability and effectiveness in combat.

Another design consideration is the range resolution. We desired to be able to isolate human targets, so we chose a noise bandwidth of 500 MHz to allow us to isolate the width of an average human. With a bandwidth of 500 MHz, the range resolution is 0.3 meters (approximately 1 foot).

In addition to the ranging considerations, we also desire to detect micro-Doppler signals from human gestures. The Doppler frequency shift is directly proportional to the transmit frequency. This means that in order to detect small human movements, it is desired to operate at as high a frequency as possible.

Because of all of these design considerations, we chose to transmit a 500 MHz noise waveform in the S-band for ranging and a continuous wave (CW) tone, also in the S-band, for Doppler detection. A switch is used to select between the two modes of operation: ranging and Doppler measurement. The switch will select either the noise waveform or the CW tone to transmit.

3.2 System Description

Here I will describe the S-band radar system in some detail. Figure 3.1 shows the block diagram of the S-band radar system and Figure 3.2 shows a photograph of the final system.

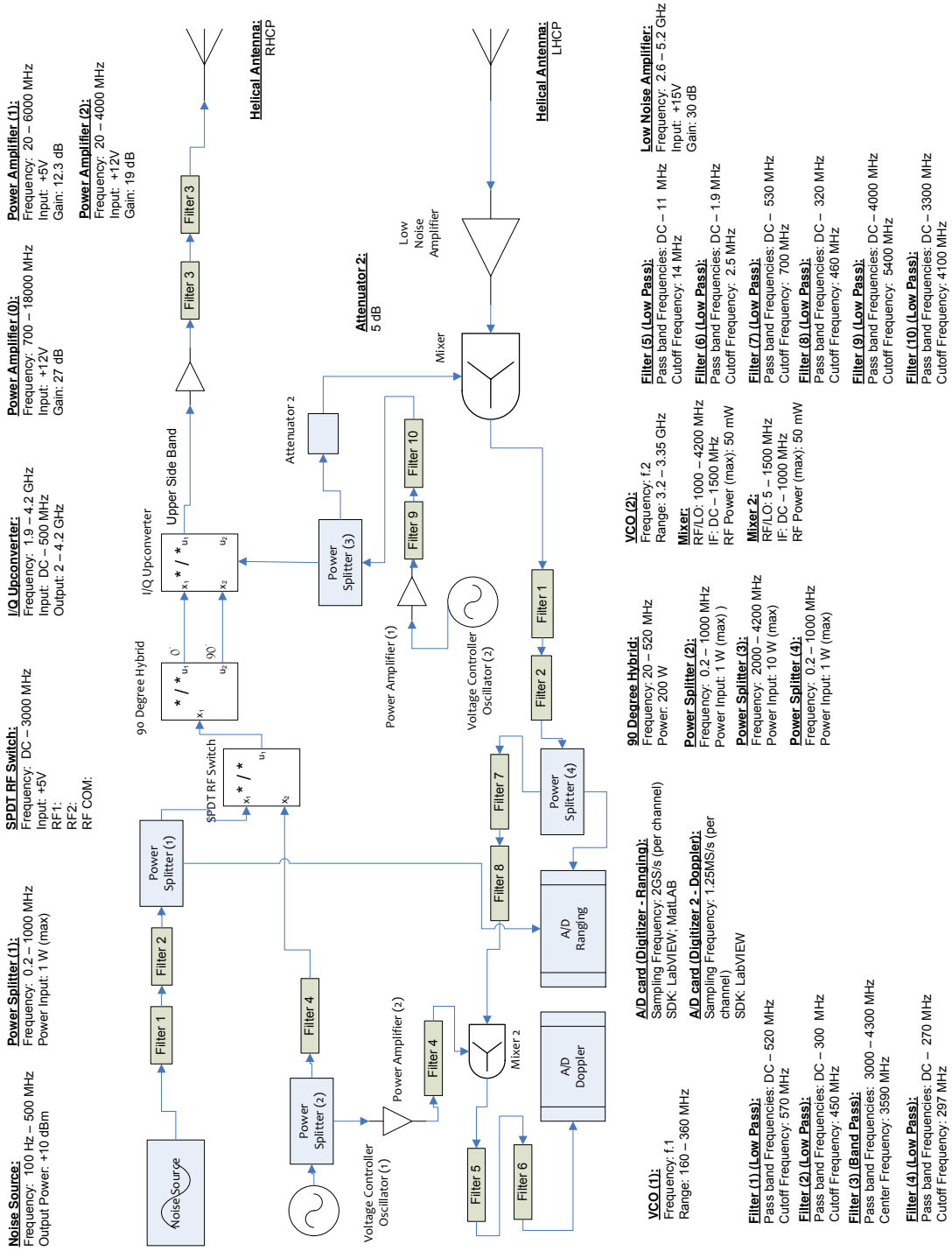

Figure 3.1: Block diagram of S-band noise radar.

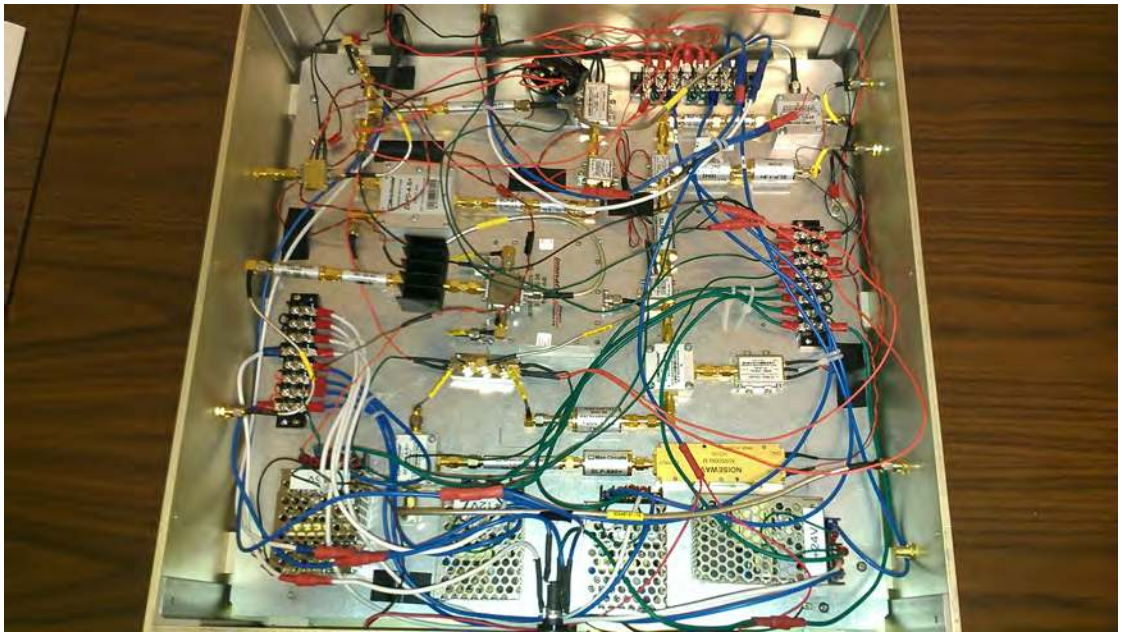

Figure 3.2: Photograph of the S-band noise radar.

3.2.1 Transmit Chain

The transmit chain depends on the mode of operation for the radar. If ranging is desired, the RF switch is set so that only a noise waveform is transmitted, whereas if Doppler mode is selected, a CW tone is transmitted. The frequency of the CW tone corresponds to the center frequency of the noise bandwidth that was selected for ranging. Regardless of which mode is selected, the remainder of the transmit chain is the same. The signal is split using a 90° splitter. This step is necessary because a single-sideband I/Q upconverter is used to mix the frequency of the transmitted signal to the S-band. The single-sideband upconverter requires the use of both in-phase and quadrature signals to operate properly and produces only the upper sideband. After amplification and filtering, the signal is transmitted using a helical antenna.

When ranging, the transmitted noise power is -68 dBm/Hz. Integrating over the 500 MHz noise bandwidth gives a total noise power of $-68 + 10\log_{10}(500 \times 10^6) = 19$ dBm. When operating in Doppler mode the power in the CW tone is 17 dBm.

To ensure the safety of the radar operator and anyone who is downrange from

the radar, the IEEE Maximum Permissible Exposure (MPE) limits were checked. At 3 GHz, the MPE limit is $f/30$ W/m^2 for controlled environments and 10 W/m^2 for uncontrolled environments [33]. Even if the lower limit of the S-band is used for calculations, this means that it is permissible for a human to be exposed to up to 66.7 W/m^2. The transmitted power for this radar operating in either of its two modes is therefore well below the allowed limits.

3.2.2 Receive Chain

The receive chain begins with the receiving antenna, which is also helical, but is opposite in polarization from the transmit antenna. Right-hand circularly polarized incident waves will be reflected off of objects as either left-hand circularly polarized or left-hand elliptically polarized waves. Because of this, the helical antennas used for transmission and reception must be wound in opposite directions to achieve opposite polarizations.

After this, the received signal is amplified with a low noise amplifier and is downconverted back to baseband for digitization. The signals are filtered again to remove the high frequency components that arise from the downconverter mixer. Next, the signal is split and one of the outputs is filtered to isolate only the DC-500 MHz noise signal and the other output of the splitter is filtered separately to isolate only the Doppler tone. Because of the switch that was used in the transmit chain, only one of these splitter outputs are relevant, but because all of the components are passive, another switch was not necessary to select which one to use. If the radar is used for ranging the signal is digitized using a GaGe Cobra CompuScope digitizer. If the radar is used for Doppler detection the signal is digitized using a National Instruments M Series Multifunction DAQ (USB-6251). The maximum sample frequency of the GaGe digitizer is 2 GS/s per channel. Because we are digitizing two channels, the digitizer can sample these signals at 1 GS/s, which is the Nyquist rate of the noise signal. The sampling rate for the National Instruments DAQ is set to 2 kS/s, which is suitable for digitizing the expected Doppler signals due to typical human behavior. In fact, this sampling rate is greater than is necessary for the S-band radar, but is set to be the same as the sampling rate for the millimeter-wave radar. The reasons for selecting a 2 kHz

sampling rate will be discussed in Chapter 4.

3.2.3 Antennas

As discussed above, this system is designed for through-the-wall operation. One additional consideration in the design of this radar system is the possibility of encountering wall materials containing rebar. If this is the case, the radar results will be degraded when using antennas with either horizontal or vertical polarization. If there is vertical rebar, using antennas with horizontal polarization would be desired and vice versa. However, because we may not know the orientation of the rebar, circularly polarized antennas are desirable. Because of this, helical antennas were chosen for this system. A diagram of a helical antenna with the important parameters labeled is shown in Figure 3.3 [34]. In this figure D is the diameter of the helix, S is the spacing between turns, $\alpha = \arctan \frac{S}{\pi D}$ is the pitch angle, L is the length of one turn, n is the number of turns, $A = nS$ is the axial length, d is the diameter of the conducting wire, and $C = \pi D$ is the circumference of the helix.

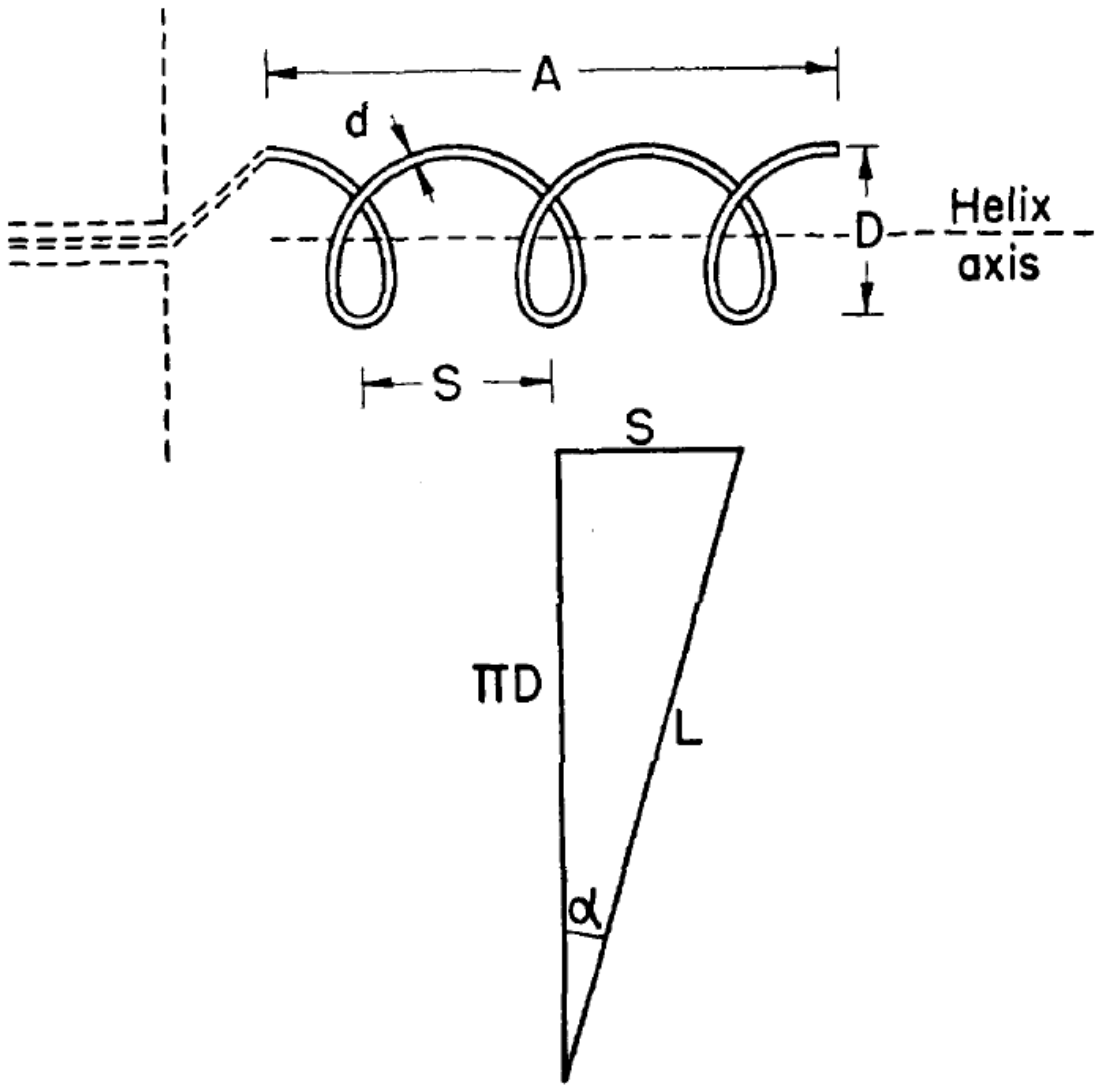

Figure 3.3: Diagram of helical antenna with important parameters highlighted.

For our antennas, we desire that the antenna operate in axial mode, which will produce an end fire beam pattern. Although there is some minor discrepancies in the literature, the antenna beamwidth (measured in degrees) and the antenna gain can be approximated by the equations given by [35]. These equations are:

$$HPBW = \frac{65^\circ}{\frac{C}{\lambda}\sqrt{N\frac{S}{\lambda}}} \tag{3.1}$$

and

$$G = \frac{26000}{HPBW^2} = 6.2\Big(\frac{C}{\lambda}\Big)^2 N\frac{S}{\lambda}. \tag{3.2}$$

The parameters for the helical antenna that was designed for this radar system are summarized in Table 3.1. Using these values the half-power beamwidth is approximately 29° and the gain is approximately 14.8 dB.

Table 3.1: Helical Antenna Parameters

Parameter	**Value**
Diameter (D)	0.028 (m)
Spacing (S)	0.022 (m)
Pitch Angle (α)	14.1°
N	19
Axial Length (A)	0.353 (m)

In addition to the design of the helix, an additional conical backplane was added to reduce the back lobe of the antenna beam so that the radar (especially when considering the micro-Doppler) did not pick up signals from the radar operator. This will also serve to increase the antenna's actual Gain and reduce the antenna's actual half-power beamwidth. An image of the final antenna design is shown in Figure 3.4 and a plot of the antenna's S11 parameters are shown in Figure 3.5.

Figure 3.4: Final design of the helical antennas.

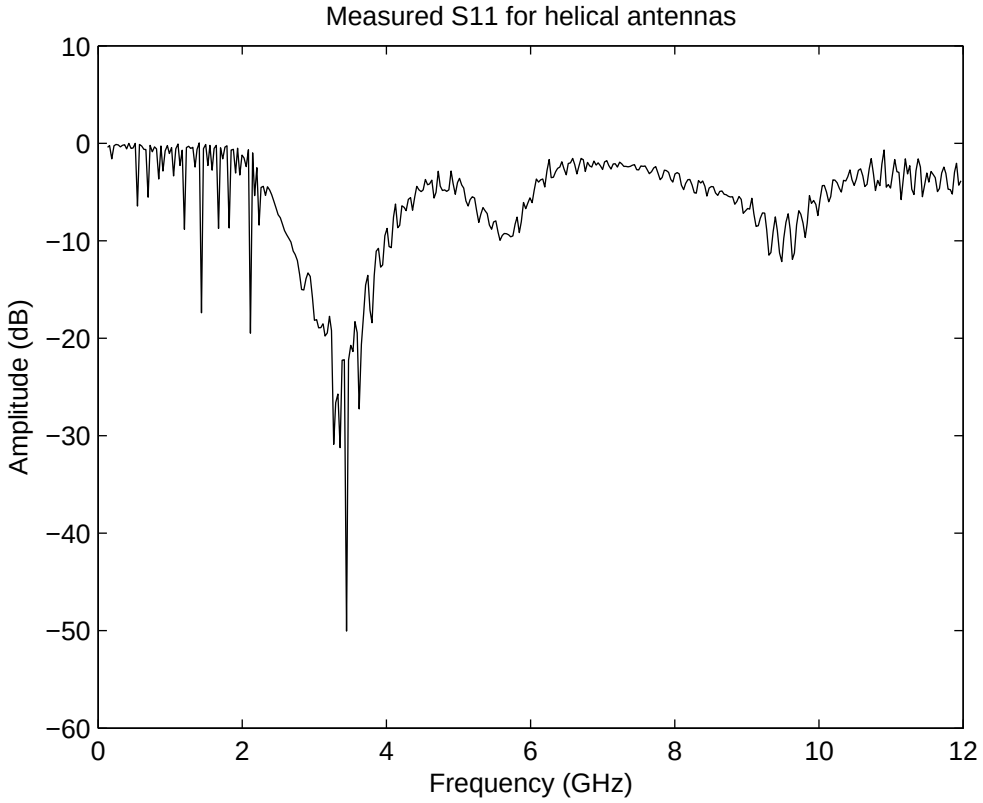

Figure 3.5: S11 measurements of the helical antennas.

3.3 Through-wall Ranging Results

The S-band radar system is capable of ranging targets behind common wall materials such as brick and concrete. Figure 3.6 shows a comparison of ranging plots both with and without a trihedral target placed 6 feet behind a 4-inch thick brick wall. As is typical in all of our through-wall experiments, the antenna coupling appears first, followed by a strong peak representing the wall barrier. In addition to this there is some additional delay time in the system, which causes the ranging plot to shift to the right. This can be canceled by measuring the delay time and subtracting it out.

In the top plot of Figure 3.6, there is not a target behind the wall, but another correlation peak can be clearly seen after the wall. This is due to the reflection coefficient of the brick wall. Energy is reflected back toward the radar operator and

our experimental setup produced an undesired correlation peak. The appearance of all of these correlation peaks (antenna coupling, wall, and other clutter targets) can be mitigated by collecting background data and subtracting the saved background from new data. The bottom plot of Figure 3.6 shows that when a trihedral target is placed behind the wall, the target can be detected by the radar. In the top plot of Figure 3.6 the largest peak represents the reflection from the wall and the next, smaller peak represents a clutter target. In the bottom plot of Figure 3.6 a peak is present in between the wall peak and the clutter peak, which represents a reflection from a trihedral corner reflector.

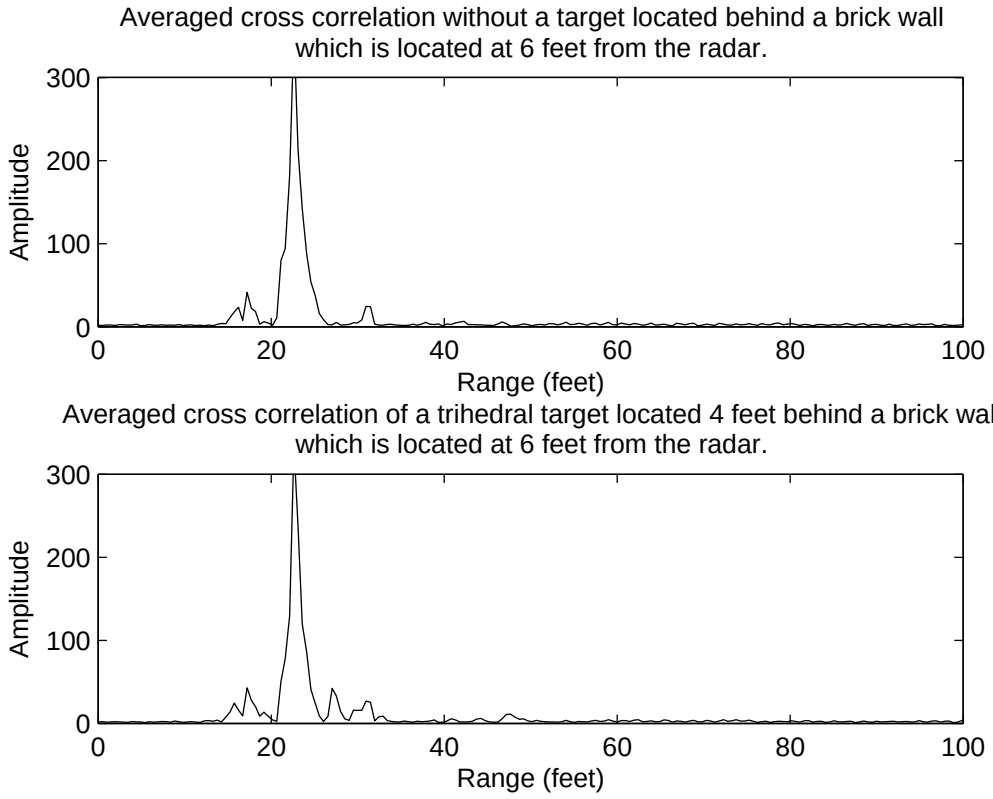

Figure 3.6: Range profiles of a 4 inch thick brick wall that is 6 feet from the radar with (Top) no target behind it and (Bottom) a small trihedral target 4 feet behind the brick wall.

Figure 3.7 shows another comparison of ranging plots when the wall barrier is constructed of 5 inch thick concrete slabs. The top plot shows the scenario where a target was not placed behind the wall and the bottom plot shows the scenario

where a trihedral target was placed approximately 5 feet behind the concrete wall. Because electromagnetic waves experience large attenuation when passing through concrete material, the radar has much more difficulty detecting the trihedral target behind the wall. However, when comparing the two range profiles, a small peak can still be identified in the bottom plot, which represents the trihedral target.

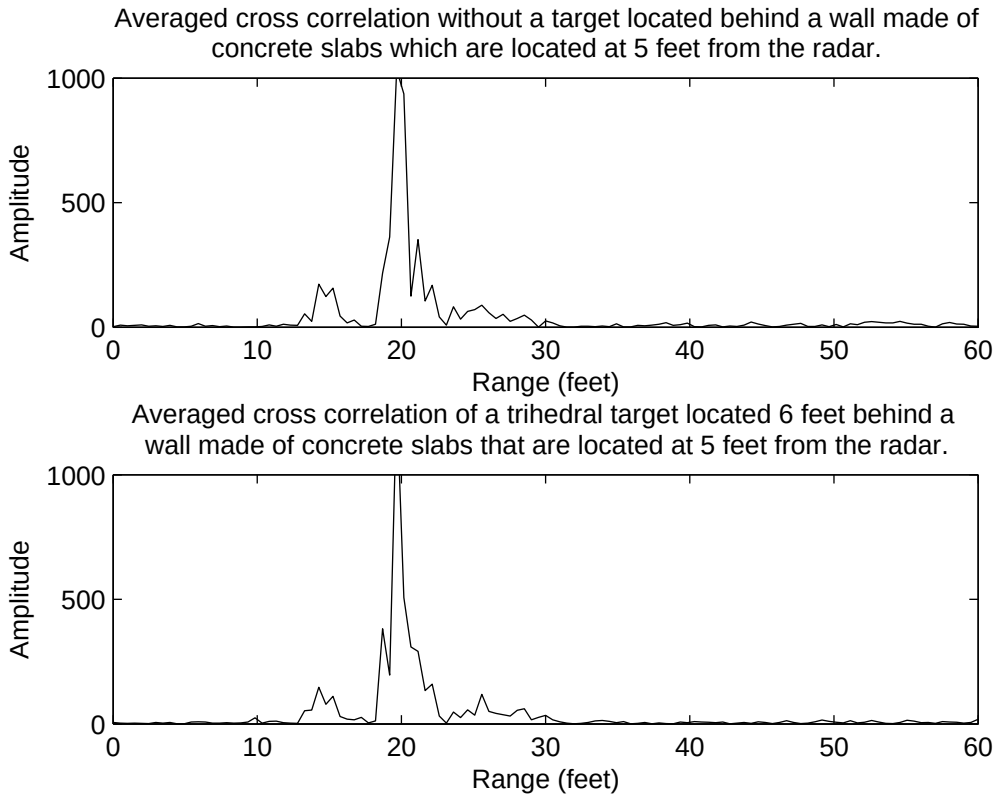

Figure 3.7: Range profile of a 5-inch thick wall made of concrete slabs. The wall is 5 feet from the radar and (Top) no target is placed behind the wall and (Bottom) a small trihedral target is placed 6 feet behind the wall.

Figure 3.8 shows ranging plots with and without a trihedral target for sensing through a laboratory wall. This scenario clearly indicates that the target can be detected. The left plot shows the range profile without a target present and the right plot shows the range profile when a trihedral target is placed between 4 and 5 feet behind the laboratory wall. This scenario involved placing a trihedral target in a room containing clutter from shelves and the other walls of the room. This clearly illustrates that targets can be detected in cluttered environments at close

range.

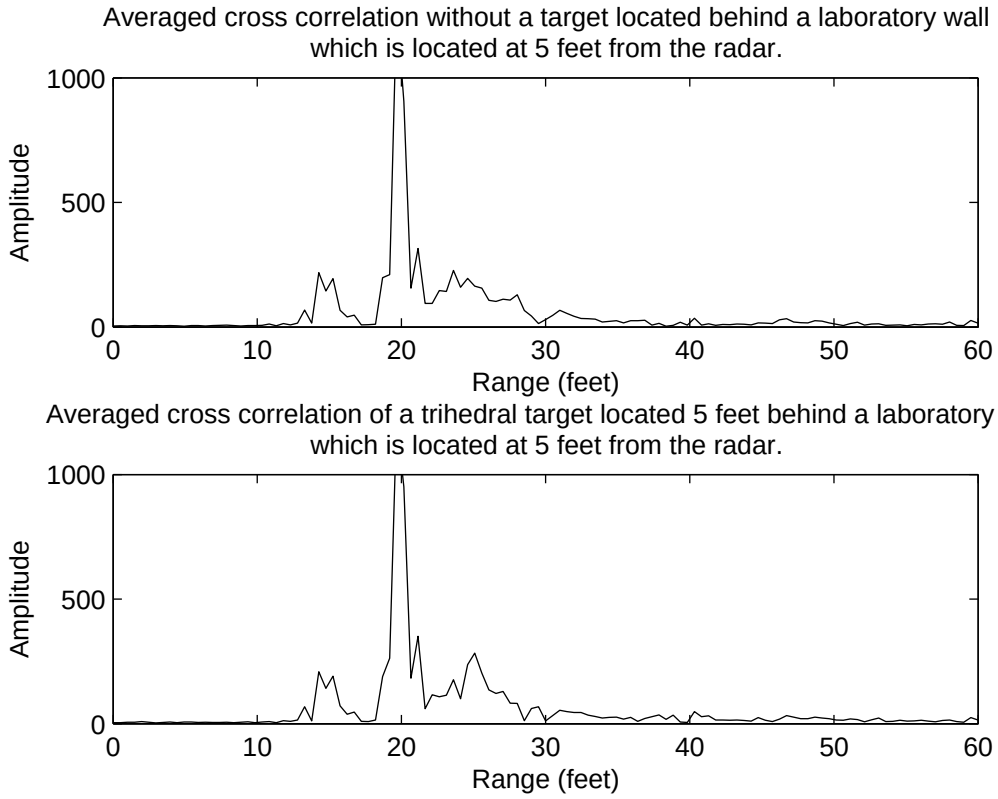

Figure 3.8: Range profile of a 4-inch thick concrete wall located at 5 feet from the radar and (Top) with no target behind the wall and (Bottom) with a small trihedral target placed 5 feet behind the wall.

As mentioned above, by collecting data on the background, clutter targets can be removed from the range profiles by subtracting the average background range profile from new range profiles. If no target is present, the ideal result of background subtraction is that the range profile is nearly flat and no prominent peaks should be visible. If a target is present, after background subtraction it should be the most prominent peak visible in the range profile. This is illustrated in Figure 3.9, where the peaks due to the antenna coupling and background have been reduced and the target peak is now the most prominent peak in the range profile. Even though averaging has been used, small fluctuations in the peaks for the antenna coupling and background result in the background not being entirely eliminated. The peak due to the brick wall is still prominent in the range profile,

but

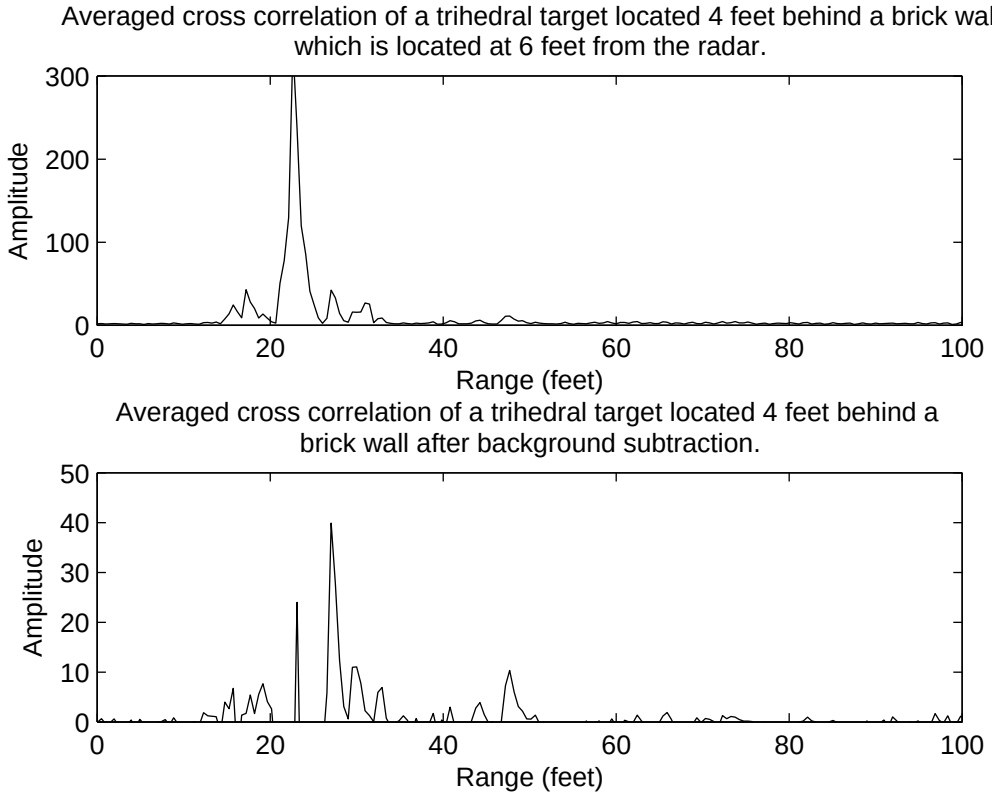

Figure 3.9: Range profile of a trihedral target located 6 feet behind a 4 inch thick brick wall (Top) without additional signal processing and (Bottom) after background subtraction.

Chapter 4

Millimeter-Wave Radar Design

The millimeter-wave radar system was designed with longer range applications in mind. Initially, we desired to detect human targets at ranges of 100 ft and possibly targets concealed by light foliage. In fact, this radar system can range targets at ranges of up to 700 feet and can detect micro-Doppler signatures at ranges of up to 300 feet. Many of the same considerations went into the design of the mm-wave radar system as went into the design of the S-band radar system. A noise waveform was chosen for its covertness, low probability of intercept, and anti-jamming capabilities. The operational environment for this radar system meant that we could choose a different transmit frequency to achieve the system goals. In addition to this, there are slight differences in the transmit waveforms due to slightly different approaches that were taken.

4.1 Design Considerations

Many design considerations for the mm-wave radar are identical to those of the S-band radar. We still desire to transmit a noise waveform with a bandwidth that will give a range resolution that can be used for human detection. For this radar, just like for the S-band radar, a 500 MHz bandwidth is utilized, resulting in a 1 foot range resolution. Because of the longer range application of the mm-wave radar, the antenna beamwidth must be much narrower in order to isolate the width of a single human target (approximately $1.5-2$ feet). In order to achieve this and keep the antenna size as small as possible, high frequency signals must be transmitted.

Another consideration is the atmospheric absorption that the wave will undergo. Figure 4.1 shows the attenuation of the signal through the atmosphere versus frequency. The W-band ($75 - 110$ GHz) is one of the high frequency bands that offer low loss when propagating through the atmosphere. Even though this radar operates at ranges where the atmospheric loss is not a large factor, if we choose a frequency in one of the transmission bands, more manufacturers were available and a larger selection of off-the-shelf components were at our disposal. Even though our minimum detection range was 100 feet, we desired to be able to detect human targets at much longer distances.

If 60 GHz was chosen, Figure 4.1 shows that the attenuation is around 20 dB/km. This will diminish our maximum detectable range by decreasing our signal to noise ratio. As will be seen in Section 4.2, this radar system is capable of ranging human targets at distances of up to 700 feet (91 meters). At this distance, the two-way path length is 181 meters and the loss in the atmosphere would be approximately 3.6 dB at 60 GHz. Referring to Figure 2.2, the maximum detectable range will be reduced by approximately 20%. This would mean that we could only detect targets at ranges of approximately 560 feet. In fact, our maximum detectable range is actually longer than 700 feet because we were limited by the environment and our ability to align our antennas to a target.

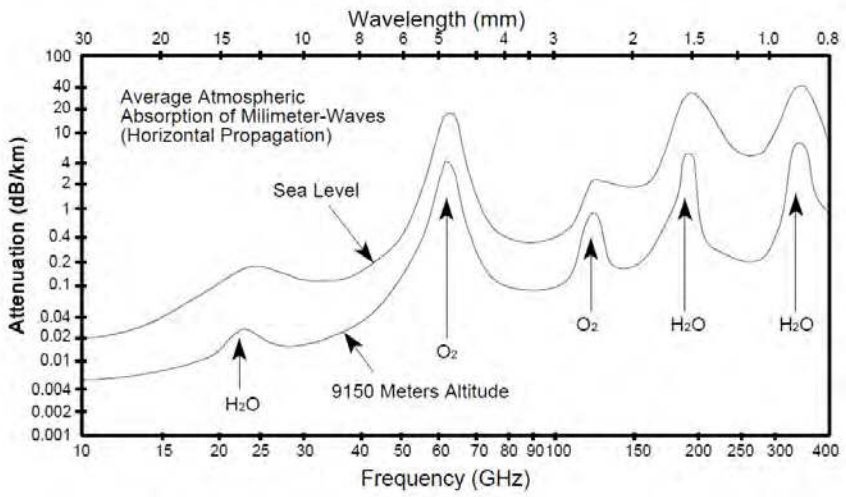

Figure 4.1: Atmospheric absorption vs. frequency.

Another reason for choosing higher frequencies, as discussed in Chapter 3, is

that larger transmit frequencies are desirable when considering Doppler signals. Because human motions are typically small and slow, large transmit frequencies will cause larger Doppler frequency shifts and make Doppler detection more accurate and reliable.

For these reasons, we chose to transmit a 500 MHz, W-band noise waveform for ranging. The CW tone for Doppler detection was also in the W-band, but was transmitted simultaneously with the noise waveform instead of switching between two modes of operation. The frequency of the CW tone slightly less than the lowest frequency of the noise waveform.

4.2 System Description

Here I will describe the mm-wave radar system in some detail. The block diagram of the mm-wave radar system is shown in Figure 4.2 and a photograph of the completed system is shown in Figure 4.3.

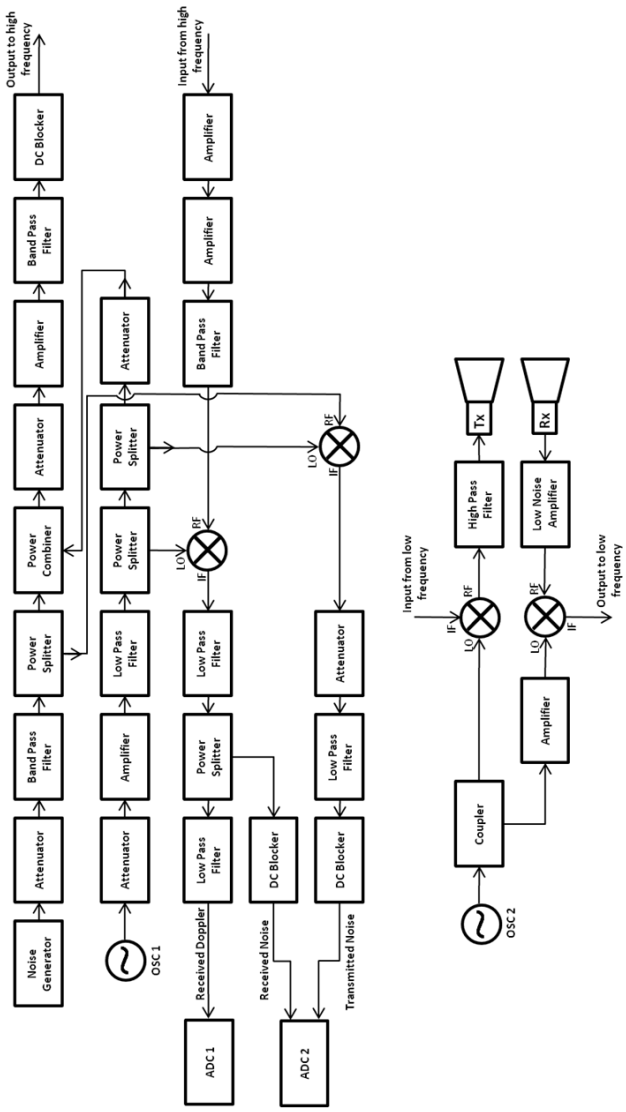

Figure 4.2: Block diagram of the mm-wave radar system.

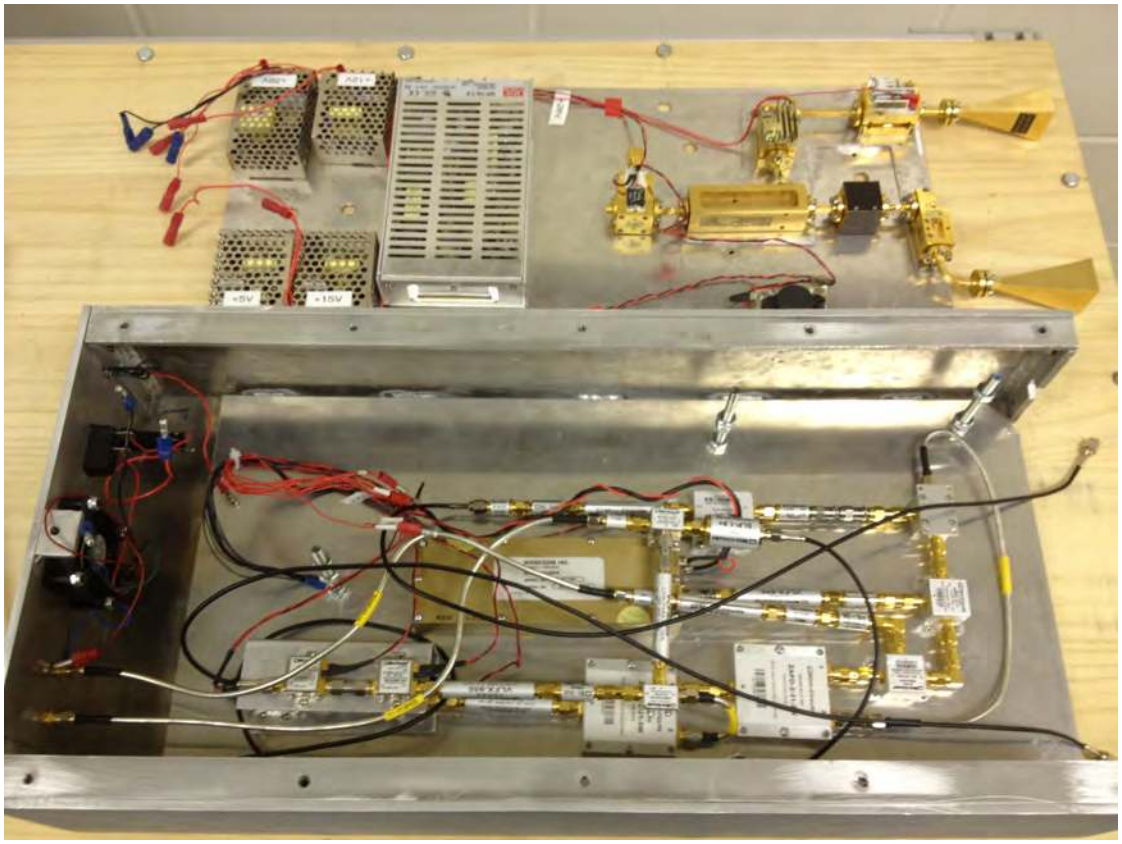

Figure 4.3: Photograph of the completed mm-wave radar system.

4.2.1 Transmit Chain

The system transmit chain consists of an L-band and a W-band section. In the L-band section, the transmit signal is generated by the use of a noise source. The noise signal is filtered to achieve a 500 MHz bandwidth. Rather than generating noise from DC to 500 MHz, the 500 MHz bandwidth is set to $1.1 - 1.6$ GHz. This allows the lower sideband and the local oscillator (LO) leakage to be easily removed via filtering when the signal is upconverted to the W-band. This is because the upper and lower sidebands are separated by 2.2 GHz and the LO leakage is separated from the upper sideband by 1.1 GHz. Filtering easily removes the lower sideband and the LO leakage. Next, the noise waveform is split so that we can digitize a copy of the transmitted waveform for correlation later. One of the splitter outputs is downconverted to DC-500 MHz and digitized for a reference waveform and the other is combined with a continuous wave tone for Doppler detection.

The tone is chosen to be at the beginning of the noise frequency band so that the noise and the single tone can be easily filtered separately for ranging and Doppler detection. The composite signal, consisting of the noise waveform with the embedded CW tone is then upconverted to the W-band. The L-band composite signal is shown in Figure 4.4. The power of the 1.1 GHz CW tone is +7 dBm. The noise waveform has an average power density of −19 dBm/MHz. Because of the 500 MHz bandwidth, this means that the noise waveform has a total power of +8 dBm. The composite signal, consisting of both the noise waveform and the embedded CW tone has a total power of +10.5 dBm.

After the composite waveform has been upconverted to the W-band, it is filtered to remove the lower sideband and the LO leakage and then it is transmitted via a dielectric horn antenna. The composite signal power is reduced by 6 dBm because of the conversion loss of the upconversion mixer, so the final transmitted power is +4.5 dBm, with +1 dBm power in the embedded CW tone and 2 dBm power in the noise waveform.

As was the case with the S-band radar, to ensure the safety of the radar operator and anyone who is downrange from the radar, the IEEE MPE limits were checked [33]. At mm-wave frequencies, the MPE limit is 100 W/m^2 for controlled environments and 10 W/m^2 for uncontrolled environments. The total transmitted power for this radar is clearly well below the allowed limits.

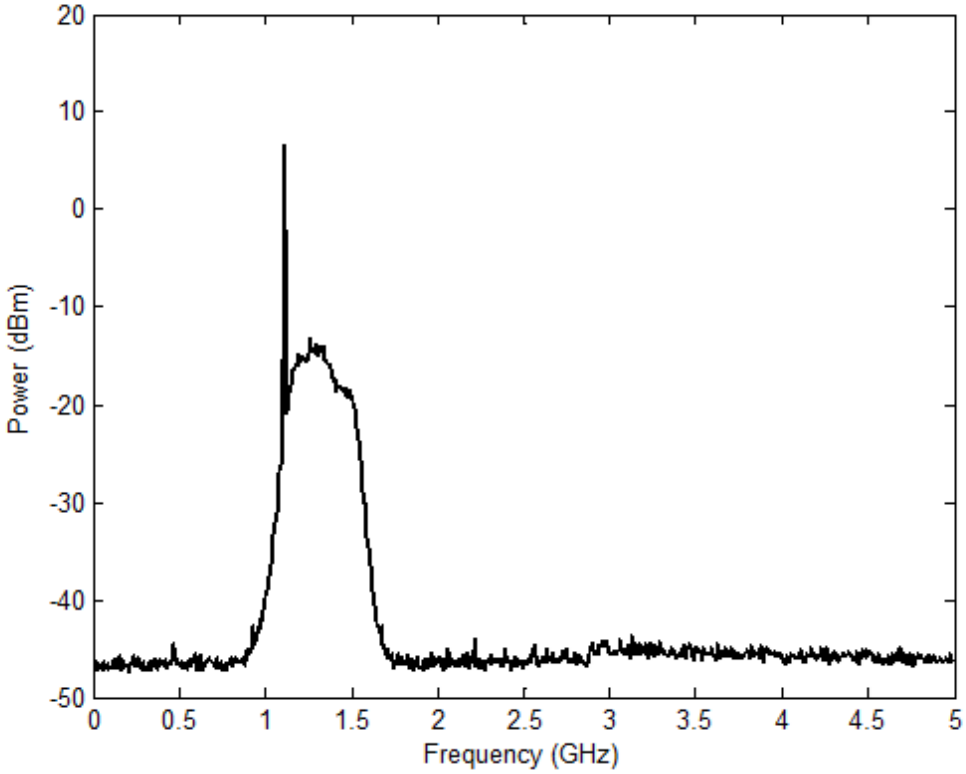

Figure 4.4: L-band waveform consisting of a 500 MHz bandwidth noise waveform with an embedded CW tone.

4.2.2 Receive Chain

The receiver chain also consists of an L-band section and a W-band section. After being received by a second dielectric horn antenna, the signal is passed through a low noise amplifier and is downconverted back to the L-band. After downconversion to the L-band, the signal is downconverted a second time to baseband. Here the signal consists only of a DC-500 MHz signal with a CW tone that has been shifted according to the Doppler equation (Equation 2.10). If the target is not moving, the CW tone will be at DC.

The noise and Doppler signals are processed separately. The baseband receive signal is split and one of the outputs is filtered to remove the Doppler tone and the other is filtered to remove the noise waveform. Once this is completed, the received noise signal and the reference noise signal (a copy of the transmitted noise

signal) is digitized using a GaGe Cobra CompuScope digitizer. The digitizer has a maximum sampling rate of 2 GS/s per channel. Because we are digitizing two channels, the digitizer can sample these signals at 1 GS/s, which is the Nyquist rate of the noise signal. The Doppler signal is digitized separately using a National Instruments M Series Multifunction DAQ (USB-6251). The sampling rate for the National Instruments DAQ is set to 2 kS/s, which is suitable for digitizing the expected Doppler signals due to typical human behavior. If the Doppler signal is equal to half the sample frequency, the velocity of the target would be between 1.35 and 2.0 m/s. For micro-Doppler signals due to human motions, where the human target does not have a translational velocity, the sampling frequency of 2 kHz will be adequate since most human motions are slow.

4.2.3 Antennas

The antennas described for the S-band radar required that we consider the possibility of vertical or horizontal rebar. For the mm-wave radar, this is not necessary, so circular polarization is not needed to ensure good results for any situation. However, because of the longer range of operation, the mm-wave radar antennas must have a very narrow beamwidth in order to isolate the width of a single human target. At 100 feet and assuming a typical human body width of approximately 2 feet, the antenna's beamwidth must be approximately 1.1°. This is achievable because of the large frequency of the mm-wave radar. We chose to use a 6 inch diameter dielectric horn antenna with a theoretical 3 dB beamwidth of 1°. The length of this antenna is 1 foot. This antenna is shown in Figure 4.5. Because of the narrow beamwidth, a red dot scope was added for ease of alignment when performing experiments. The beam pattern of this antenna is shown in Figure 4.6.

Figure 4.5: Dielectric horn antennas used with the mm-wave radar.

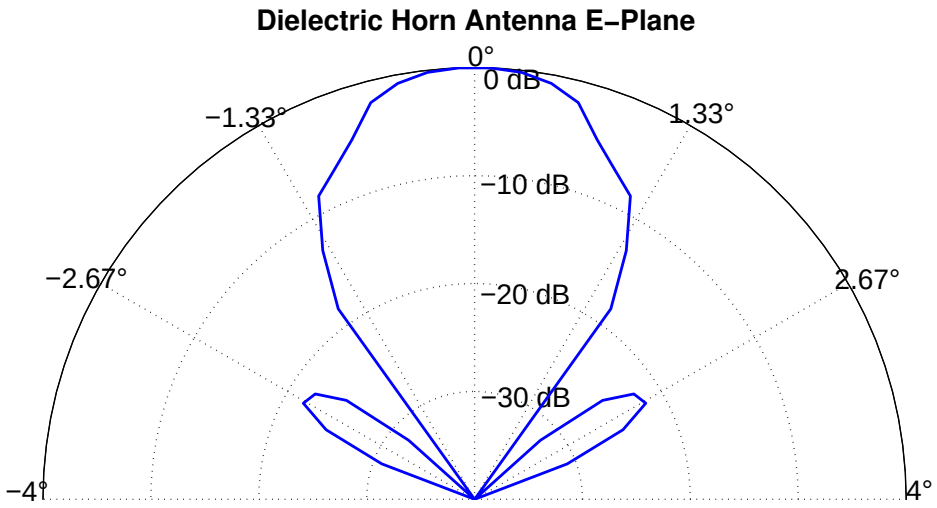

(a)

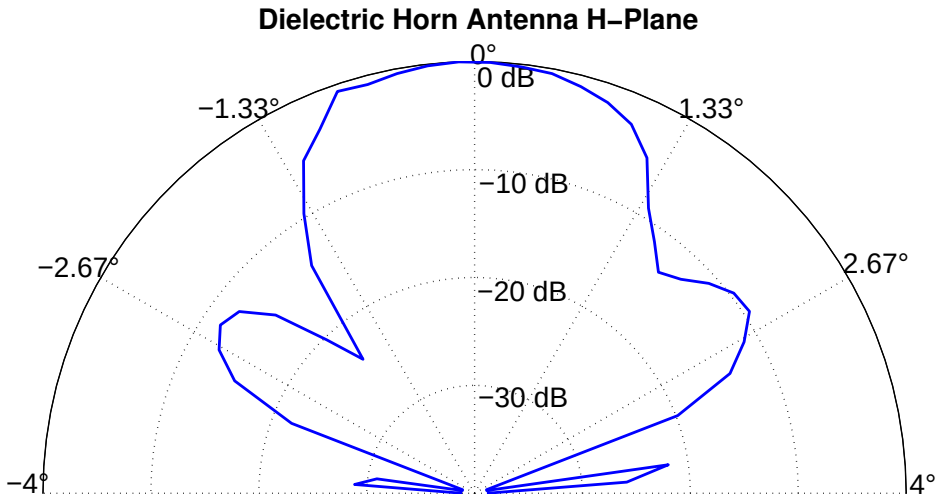

(b)

Figure 4.6: Beam pattern of the dielectric horn antennas for (Top) E-Plane and (Bottom) H-Plane.

4.3 Ranging Results

4.3.1 Long Range Detection

As discussed earlier, the maximum range of this radar system was experimentally measured to be at least 700 feet. Because of the environment and our inability to accurately align the antennas to our target at these long ranges, the theoretical maximum range of the system is much larger. Figure 4.7 shows the ranging plot of a human target standing at 700 feet (213 meters) and Figure 4.8 shows the ranging plot of the data after background subtraction. These ranging plots show some clutter targets that obscure the human target at 700 feet if background subtraction is not performed. After background subtraction, there are still some clutter targets, but the human target at 700 feet is clearly identifiable.

At 213 meters, the SNR of the human target is approximately 13 dB. Signals with a SNR of less than 13 dB can be detected, so if we assume that a 1 dB SNR is required to detect the target, using the radar range equation, the theoretical maximum range of detection is approximately 425 meters (1400 feet).

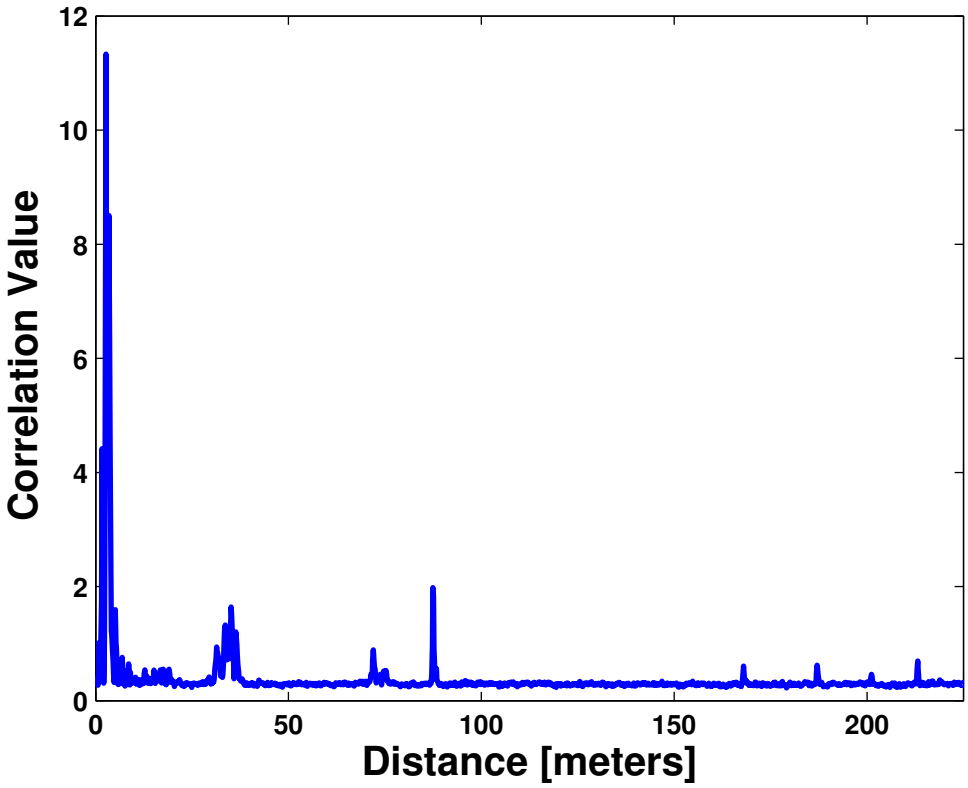

Figure 4.7: Correlation plot of human target standing at 700 feet (213 meters) prior to background subtraction.

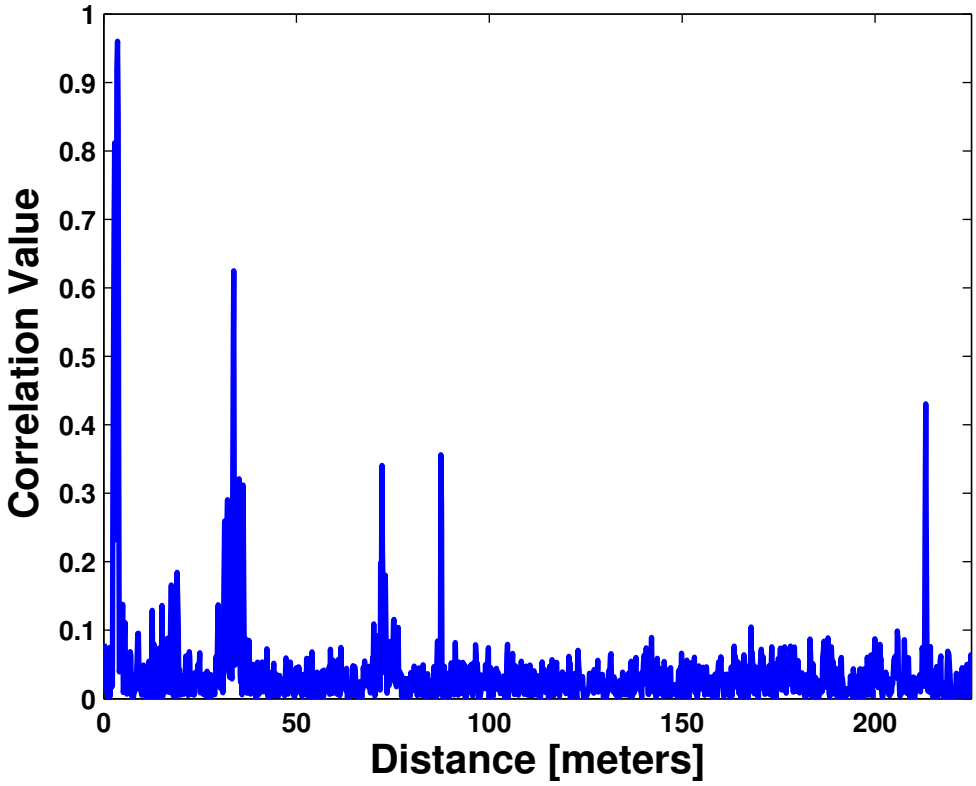

Figure 4.8: Correlation plot of human target standing at 700 feet (213 meters) after background subtraction.

4.3.2 Through Foliage Detection

As discussed earlier, it is desired that this system be capable of detecting targets concealed by light foliage (foliage penetration or FOPEN). Tests have been performed that confirm this capability of the radar. The radar was directed at a Forsythia Intermedia bush located at approximately 100 feet. The dimensions of the bush were approximately 2 m $\times$ 2 m $\times$ 10 m. Ranging data for the FOPEN scenario were collected for both a corner reflector and a human target. The results are shown in Figure 4.9. The top left figure shows the correlation results of a bush without leaves with no target behind it, the top right figure shows the results of a corner reflector target concealed behind the bush without leaves, the bottom left figure shows the correlation results of a corner reflector target concealed behind the bush with leaves, and the bottom right figure shows a human target concealed

behind the bush when it had no leaves on it.

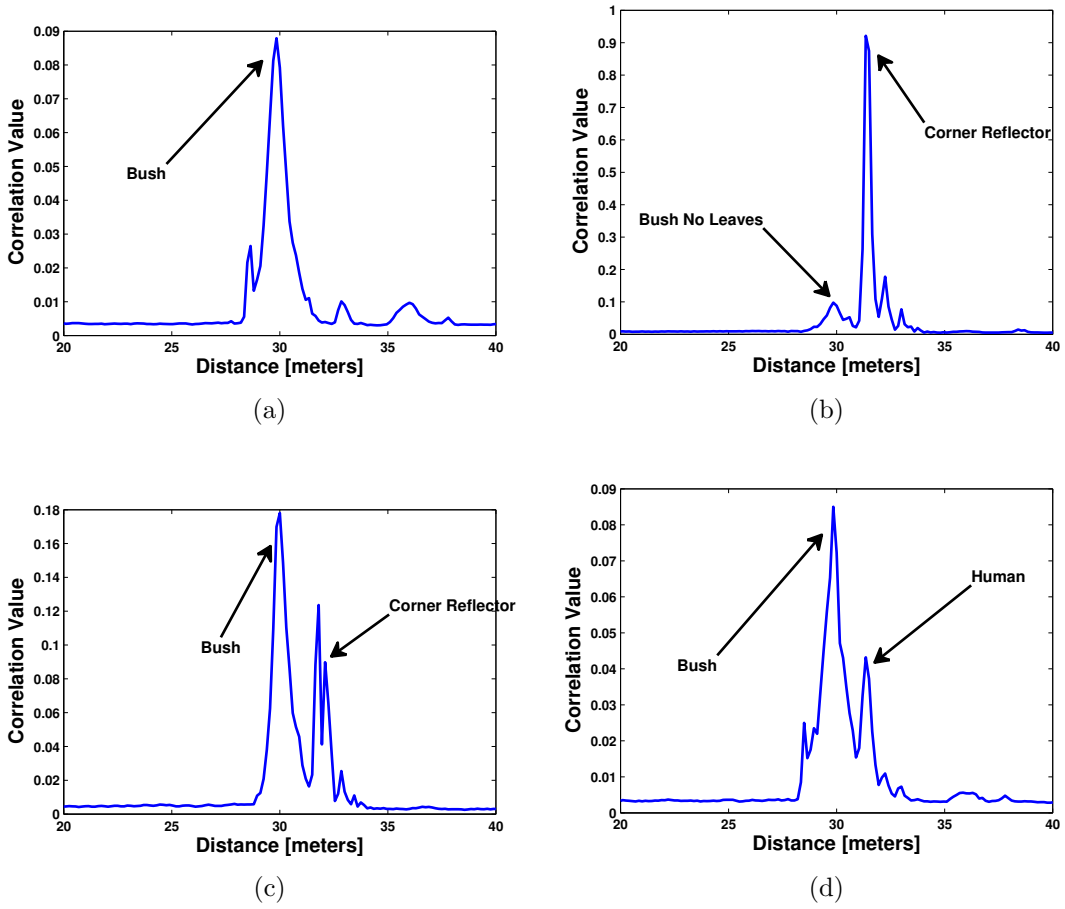

Figure 4.9: Correlation plots of the bush at 100 feet (a) without leaves and no target behind it, (b) without leaves and with a corner reflector behind it, (c) with leaves and with a corner reflector behind it, and (d) without leaves and with a human target behind it.

It is clear from these plots that the presence or absence of leaves has a large effect on the ability of a radar to detect targets concealed in light foliage. Because the corner reflector had a larger RCS than a human, the corner reflector was detectable regardless of whether there were leaves or not. In the bottom right plot of Figure 4.9, the human target is more difficult to detect even without leaves on the bush. When leaves were present, the human target was completely concealed by the bush.

Chapter 5

Time-Frequency Transforms

When analyzing micro-Doppler signals, the time-varying nature of the signal makes traditional analysis techniques such as the Fourier transform inadequate for getting a complete picture of how the target is moving relative to the radar. The Fourier transform assumes a linear time-invariant system. Because the Doppler frequency changes over time, we can easily see how the Fourier transform is not suitable for analyzing micro-Doppler signatures. While the Fourier transform can be useful in many applications to Doppler radar, other techniques must be explored if knowledge of how the velocity of the target changes over time is desired. Among the simplest of these is the Short-Time Fourier Transform (STFT). Many other techniques have also been developed. Wavelet theory has recently been gaining in popularity, and other techniques such as the Wigner-Ville distribution (WVD), Choi-Williams distribution (CWD), and the Hilbert-Huang transform (HHT) are also widely used in practice. For an in-depth discussion of these and other time-frequency transforms, see [36, 37, 38, 39, 40, 41]

5.1 Short-Time Fourier Transform

The Fourier transform is the fundamental signal processing tool today. However, it has drawbacks when analyzing non-linear and non-stationary signals. The Fourier transform projects a signal $x(t)$ onto a set of orthonormal bases that are complex sinusoids with infinite extent, as shown in Equation 5.1. The Fourier transform assumes linearity and time-invariance and these basis functions are formulated

in such a manner that time-frequency information cannot be extracted from the signal. The Fourier transform can only give information as to which frequencies were present within the duration of the signal, but cannot give information as to when they occurred (except that they occurred sometime within the duration of the signal).

$$X(\omega) = \int_{-\infty}^{\infty} x(t)e^{-j\omega t}dt \tag{5.1}$$

In order to evaluate how a function changes over time, the simplest approach is to window the data and slide the window across the entire duration of the signal. This approach is the well-known Short-Time Fourier transform (STFT) and is expressed in Equation 5.2, where $w(t)$ is the window function. Here the signal is projected onto the basis functions: $w(t-\tau)e^{j\omega t}$.

$$STFT(t,\omega) = \int x(\tau)w(\tau - t)e^{-j\omega\tau}d\tau \tag{5.2}$$

By the uncertainty principle $\Delta_t\Delta_\omega \geq \frac{1}{2}$, where Δ_t is the time resolution and Δ_ω is the frequency resolution, the smaller the time window, the poorer the frequency resolution. Because of the windowing operation, in order to gain information on how the signal varies with time, we must sacrifice some of our frequency resolution.

The window function and the width of the window both must be selected appropriately depending on the application. Hanning, Hamming, and rectangular windows are frequently used. Some are selected for their simplicity, others for their sidelobe suppression A Gaussian window, as shown in Equation 5.3 is sometimes chosen because it has the desirable property of achieving the lowest possible time-frequency product ($\Delta_t\Delta_\omega = \frac{1}{2}$).

$$w(t) = \frac{1}{\pi^{1/4}\sqrt{\sigma}}e^{-\frac{t^2}{2\sigma^2}} \tag{5.3}$$

5.2 Continuous Wavelet Transform

In the STFT discussed above, the frequency resolution is a constant. Low frequency signals and high frequency signals alike will have the same frequency resolution. In many cases, this is not desirable. For example, assume that the frequency

resolution of the STFT is 10 Hz and the signal to be analyzed has a frequency of 20 Hz for the first half of the signal duration and a frequency of 1 kHz for the second half of the signal duration. The frequency resolution is 50% of the 20 Hz component but is only 1% of the 1 kHz component. When analyzing this signal, having equally spaced frequency resolution bins is not desirable.

The Continuous Wavelet Transform (CWT) solves this problem by introducing multi-resolution. The mathematical expression for the CWT is shown in Equation 5.4, where a is the scale parameter, b is the translation parameter, and ψ is the mother wavelet. The scale parameter is analogous to frequency and the translation parameter is analogous to time, resulting in a "scale-translation" or time-frequency representation of the signal. Common wavelet functions include the Haar, Daubechies, Symlet, Coiflet, Mexican Hat, Morlet, and Meyer wavelets. The wavelet selection is dependent on the application. In the cases of the Fourier transform and the STFT, the signal was projected onto the basis functions: $e^{j\omega t}$ or $w(t)e^{j\omega t}$. The CWT no longer uses complex exponentials for basis functions, but instead uses scaled and translated versions of the mother wavelet. By scaling the mother wavelet, multi-frequency resolution is attained [40, 41].

$$CWT(a,b) = \frac{1}{\sqrt{|a|}} \int_{-\infty}^{\infty} x(t)\psi^*\Big(\frac{t-b}{a}\Big)dt \tag{5.4}$$

5.3 The Hilbert-Huang Transform and Empirical Mode Decomposition

The Hilbert-Huang transform is an adaptive time-frequency technique that is well-suited for non-linear and non-stationary time series. It combines a sifting process called Empirical Mode Decomposition (EMD) to decompose a signal into its various components with the Hilbert transform to analyze the instantaneous frequency of each signal component. Because of the adaptive nature of EMD, there is not a solid theoretical foundation on which this time-frequency transform is based upon. Instead, empirical testing has shown it to be reliable in decomposing signals into components which are physically meaningful. One advantage that EMD has is that it does not require *a priori* knowledge of the signal and is also not dependent

on the selection of a kernel function like the wavelet transform and others.

EMD will decompose a signal into its intrinsic oscillatory modes (also called Intrinsic Mode Functions), based on the time-scale of the oscillations. The faster oscillations in the signal will be present in the lower-indexed IMFs and the slower oscillations will be present in the higher-indexed IMFs. These oscillatory modes, called Intrinsic Mode Functions (IMF), are components of the original signal and each IMF is orthogonal to all of the other IMFs. The orthogonality of the IMFs allow for EMD to be used in a number of ways. Filtering of the signal can be performed by selectively adding together IMFs of the signal and omitting others. In addition to this, the mechanism that produces the signal can be analyzed by inspecting IMFs that have known properties [42].

The EMD algorithm consists mainly of a sifting process. In this process the extrema of the signal $s(t)$ are identified. From the extrema, the envelope of the minima, $x_{min}(t)$, and the envelope of the maxima, $x_{max}(t)$, are formed by interpolation techniques. Next, the mean of these two envelopes is calculated as:

$$m(t) = \left(\frac{x_{max}(t) + x_{min}(t)}{2} \right) \tag{5.5}$$

and the mean envelope is subtracted from the signal to complete the first iteration of the sifting process. The resulting signal is denoted by $x_j^k(t)$ ($k = 1$, $j = 1$), where k indicates the iteration and j indicates the index of the IMF. This sifting process is repeated until the stopping criteria have been met, meaning $< x_j^k(t) >= 0$ (the mean envelope is equal to zero at all times) and the number of zero crossings of $x_j^k(t)$ differs from the number of extrema by no more than 1. Once this condition has been satisfied, we set $x_j^k(t) = I_j(t)$ and $I_j(t)$ is the j^{th} IMF ($I_1(t)$) of x(t). Next, the residue is calculated as: $x_j^r(t) = x(t) - I_1(t)$. The sifting process is then repeated, where the residue is: $x_j^r(t) = x(t) - \sum_{i=1}^{i=j} I_i(t)$. This process is repeated until the residue is either monotonically increasing or monotonically decreasing (having only a single zero crossing). Figure 5.1 illustrates the process of decomposing a signal into its components using EMD.

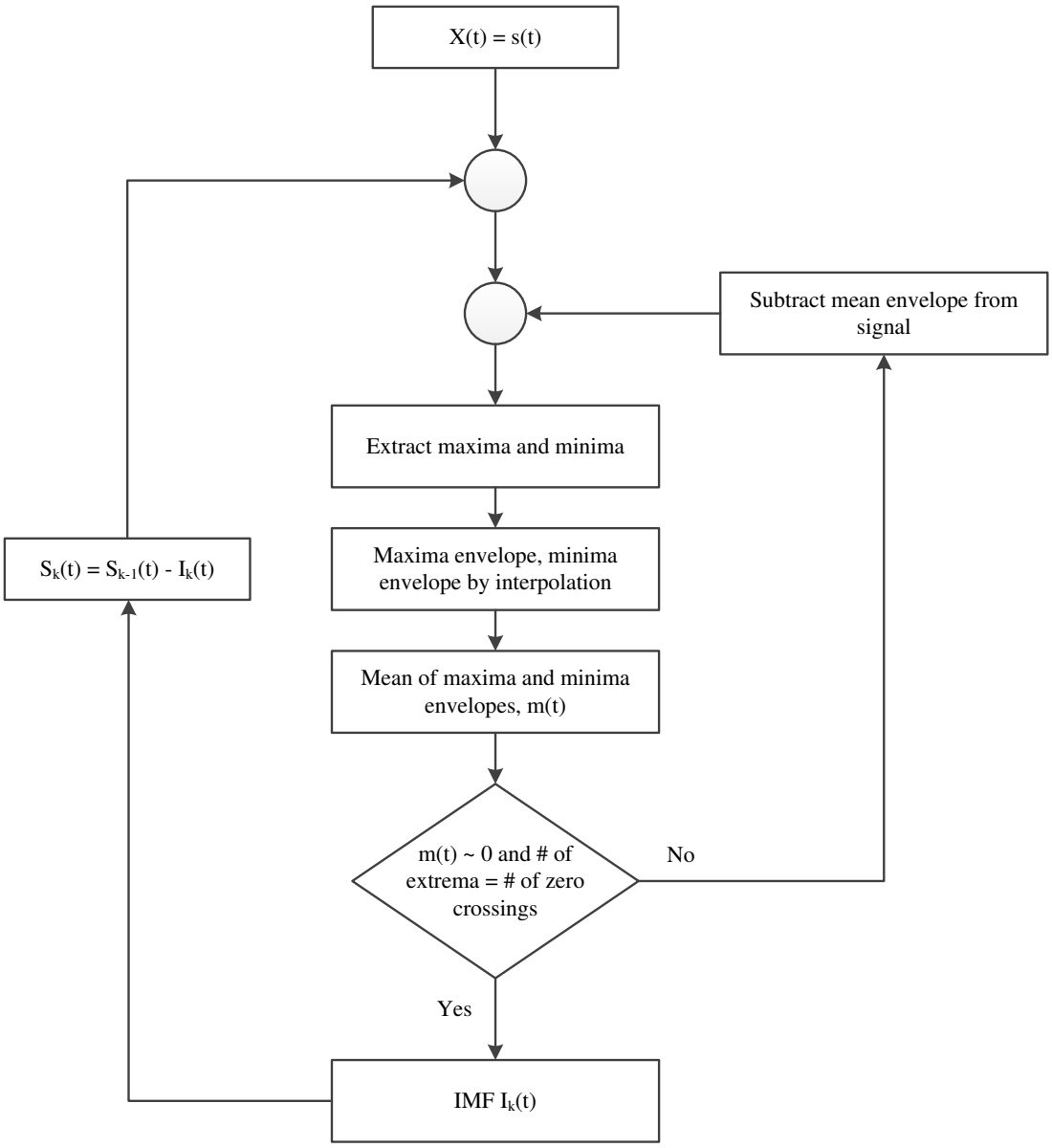

Figure 5.1: EMD algorithm flowchart.

Ideally we would like to meet the stopping criteria exactly; however, the stopping criteria can often be relaxed without decreasing the performance of EMD. In fact, if the stopping criteria are too stringent, the resulting IMFs often no longer have any physical meaning. This is called this "oversifting." To avoid oversifting, instead of requiring $< x_j^k(t) >= 0$ for all time, we require $< x_j^k(t) >\leq C_2$ for all time and $< x_j^k(t) >\leq C_1$ for $(1 - tolerance) * 100\%$ of the time, where $C_1 < C_2$.

By defining two thresholds and a tolerance, the stopping criteria are relaxed. We can also relax the stopping criteria by setting an upper limit to the number of iterations that the inner loop of Figure 5.1 completes. In addition to avoiding the problem of oversifting, by relaxing the stopping criteria, the total time that it takes to complete EMD is reduced, which is desirable in most applications. Reducing the time for EMD to finish can also be achieved by decreasing the number of points in your signal. This can be accomplished by adjusting the parameters for digitization (sampling frequency and number of points) or it can be realized after digitization by decimation. Decimation is the process of downsampling followed by low-pass filtering. Chapter 8 discusses how EMD and classification are affected by changing the various stopping criteria and by varying how much the data is decimated.

The Hilbert transform can then be performed on the collection of IMFs that result from the EMD process. This is the second part of the HHT algorithm. The Hilbert transform is a method of calculating the instantaneous frequency of a real-valued signal and it is related to the number of zero crossings that occur in a given time [37, 43]. The Hilbert transform can be calculated by

$$y(t) = \mathcal{H}[x(t)] = \frac{1}{\pi} PV \int_{-\infty}^{\infty} \frac{x(\tau)}{t-\tau} \mathrm{d}\tau. \tag{5.6}$$

In Equation (5.6), PV denotes the principal value of the singular integral. Once the Hilbert transform has been found, the analytic signal is

$$z(t) = x(t) + jy(t) = x(t) + j\mathcal{H}[x(t)] = a(t)e^{j\theta(t)}. \tag{5.7}$$

The instantaneous amplitude $a(t)$ and instantaneous phase $\theta(t)$ are then found simply by:

$$a(t) = \sqrt{x^2 + y^2} \tag{5.8}$$

and

$$\theta(t) = \arctan \frac{y}{x}. \tag{5.9}$$

The instantaneous frequency can then be determined simply by

$$\omega(t) = \frac{d\theta}{dt}. \tag{5.10}$$

Past applications of the Hilbert transform have been limited to narrowband signals. This is the reasoning behind performing the EMD sifting operation first so that monocomponent signals are considered. The HHT algorithm calculates the instantaneous frequency and instantaneous amplitude of each IMF component separately. After HHT has been performed, if it is desired, the original signal can be represented as in Equation 5.11 based on its instantaneous amplitude and instantaneous frequency components. Compare this to the Fourier representation in Equation 5.12. In the Fourier case, both a_i and ω_i are constants. It is apparent that the IMF represents a generalized Fourier expansion. By permitting the amplitude and frequency to vary with time, HHT allows for non-linear and non-stationary signals to be analyzed.

$$x(t) = \Re\Big\{ \sum_{i=1}^{n} a_i(t) \exp\Big[j \int w_i dt \Big] \Big\} \tag{5.11}$$

$$x(t) = \Re\Big[\sum_{i=1}^{n} a_i e^{j\omega_i(t)t} \Big] \tag{5.12}$$

The procedure that has been described provides us with a time-frequency distribution that relies on the amplitude of each component. This time-frequency transform is called the Hilbert amplitude spectrum.

In addition to the Hilbert spectrum, the energy of the components can be analyzed. The energy of a signal can be easily calculated as the inner product of the signal with itself. When the EMD process is conducted on micro-Doppler signals, the collection of IMF energies provides us with a vector that is unique to the movement that caused the Doppler frequency shift. This allows for the energy vector to be used as a feature vector, on which classification or pattern recognition techniques can be performed.

5.4 Other Time-Frequency Transforms

Other commonly used time-frequency transforms include Cohen's class of time-frequency transforms, which include the Wigner-Ville distribution (WVD) and the Choi-Williams distribution [36, 39, 40]. The expression for the Wigner-Ville distribution is:

$$WVD(t,\omega) = \int x\Big(t+\frac{\tau}{2}\Big)x^*\Big(t-\frac{\tau}{2}\Big)e^{-j\omega\tau}d\tau. \tag{5.13}$$

By inspection of Equation 5.13 it is evident that the WVD is simply the Fourier transform of the autocorrelation function. The expression for the Choi-Williams distribution is:

$$CWD(t,\omega) = \iint \frac{1}{\sqrt{4\pi\alpha(\tau)^2}} e^{-\frac{(t-u)^2}{4\alpha(\tau)^2}} x\Big(u+\frac{\tau}{2}\Big)x^*\Big(u-\frac{\tau}{2}\Big)e^{-j\omega\tau}dud\tau \tag{5.14}$$

Both the WVD and the CWD are special cases of Cohen's class of time-frequency transforms. The general form of Cohen's class is shown in Equation 5.15, where ϕ is a two-dimensional kernel function. The kernel determines the distribution and also the properties of the distribution. If ϕ is chosen to be 1 then it reduces to the WVD.

$$C(t,\omega) = \frac{1}{4\pi^2}\iiint e^{-j\theta t - j\tau\omega + j\theta u}\phi(\theta,\tau)x\Big(u+\frac{\tau}{2}\Big)x^*\Big(u-\frac{\tau}{2}\Big)dud\tau d\theta \tag{5.15}$$

Because θ does not appear in the signal itself, this general form of Cohen's class can be simplified by defining a new kernel, r, which is the Fourier transform of the original kernel, ϕ.

$$r(t,\tau) = \frac{1}{2\pi}\int \phi(\theta,\tau)e^{-jt\theta}d\theta \tag{5.16}$$

Using this new kernel, the general form of Cohen's class becomes:

$$\iint r(t-u,\tau)x\Big(u+\frac{\tau}{2}\Big)x^*\Big(u-\frac{\tau}{2}\Big)e^{-j\omega\tau}dud\tau \tag{5.17}$$

If r is chosen to be

$$r(t,\tau) = \frac{1}{\sqrt{4\pi\alpha(\tau)^2}} e^{-\frac{t^2}{4\alpha(\tau)^2}} \tag{5.18}$$

then Equation 5.17 is the expression for the CWD. As previously mentioned, the kernel function determines properties of the distribution. Because the WVD is simply the Fourier transform of the autocorrelation function, it suffers from having significant cross-term interference (two separate components in the signal present themselves as a new term in the distribution, which is the product of the two components). The kernel for the CWD is chosen to significantly reduce the cross terms.

Chapter 6

Micro-Doppler Signals of Stationary Targets

As is usually the case in through-the-wall applications, the target is located in an indoor environment and is therefore limited to the distances that it can move. For this reason, another class of micro-Doppler movements is considered: targets that have no translational velocity. In this situation, the mean Doppler frequency is zero. Detecting these motions is more difficult than detecting motions due to gait because the movements are much slower and produce much smaller Doppler frequency shifts. The ability to detect these motions is challenging when the target is trying to remain concealed. Here, we develop some simple models to describe some basic human motions. The modeling and experimental results are shown for both the S-band and millimeter-wave (mm-wave) micro-Doppler radar systems [44, 45].

6.1 Experimental micro-Doppler of Human Motions

Before discussing the models for some basic human motions, some experimental results are shown to illustrate the different parts of each movement that must be considered. The four basic human motions that will be considered here are breathing, swinging arms, picking up an object, and transitioning from crouching

to standing. The micro-Doppler signature of a pendulum is also considered. The micro-Doppler signals and the corresponding STFTs of the signals are shown in Figures 6.1 - 6.10. The micro-Doppler time signature is shown on the left and the STFT is shown on the right. These experiments were performed with non-coherent CW Doppler radars. One operating in the S-band and the other operating in the mm-wave frequency range. Because of the non-coherence of the radar, the direction of travel cannot be determined. Any motion that creates a negative Doppler frequency shift will be displayed as a positive frequency because only real-valued signals are collected.

For the human motions in Figures 6.3, 6.5, 6.7, and 6.9, the S-band radar was used and was operating in an indoor environment with the human located at approximately 3 feet behind a 4 inch thick laboratory wall. The radar was located approximately 9 feet in front of the wall.

For the human motions in Figures 6.4, 6.6, 6.8, and 6.10, the mm-wave radar was used and was operating in an outdoor environment with the human located at approximately 100 feet from the radar.

Figures 6.1 and 6.2 show the motion that is exhibited by a swinging pendulum when measured with the S-band and mm-wave radars respectively. The pendulum is a long flat metal plate that swings at a pivot point. The motion is sinusoidal and because the pendulum is not forced, friction causes the pendulum to slow down gradually. This is clearly seen in the STFT plot where the maximum frequency of each successive swing is lower (indicating a slower speed) than the one before it.

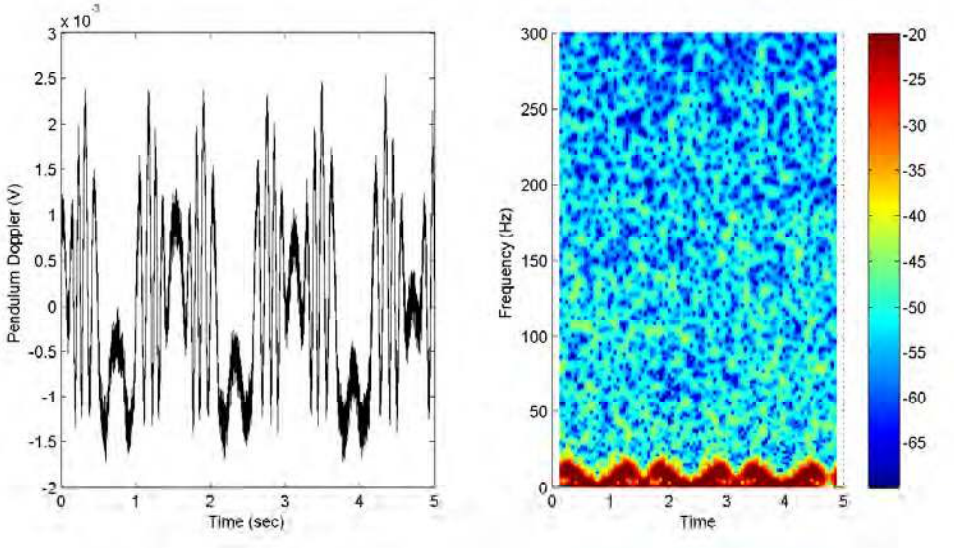

Figure 6.1: (Left) Experimentally measured micro-Doppler of a pendulum and (Right) STFT of the micro-Doppler signal for an S-band radar.

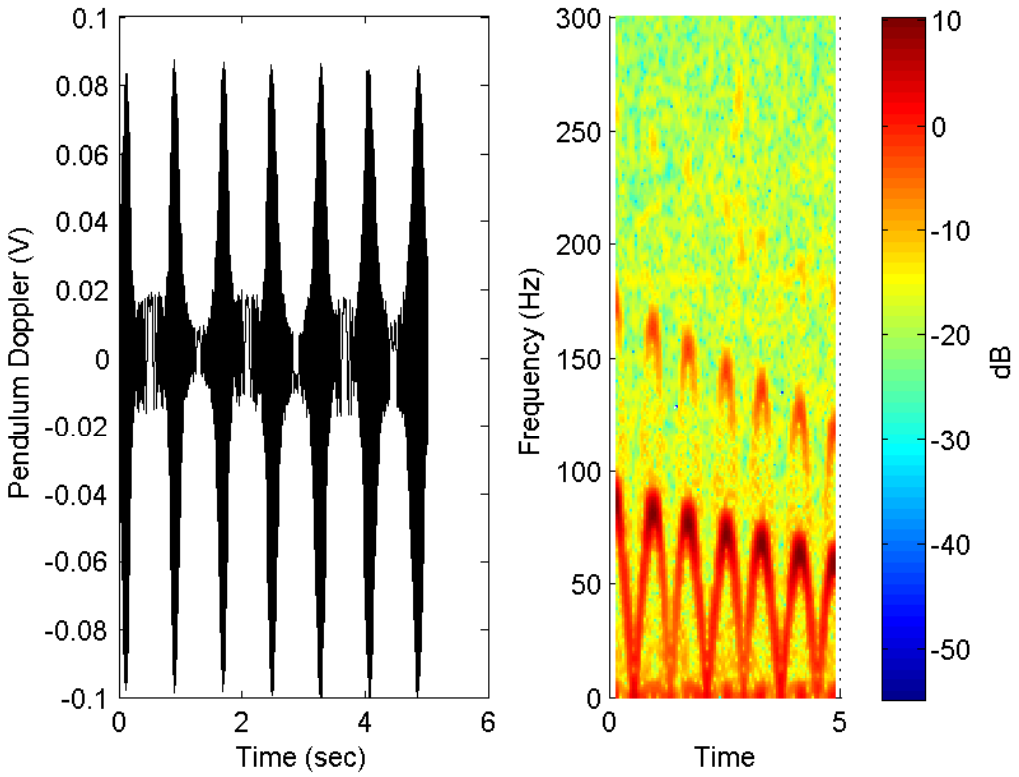

Figure 6.2: (Left) Experimentally measured micro-Doppler of a pendulum and (Right) STFT of the micro-Doppler signal for a mm-wave radar.

Figures 6.3 and 6.4 show the micro-Doppler signature due to a human swinging their arms using the two radars. While this motion is similar to the motion of a pendulum, it is evident from the STFT plot that the arm swinging of a human is more complex and contains more components. The additional components are mainly due to the torso swaying to maintain balance and the fact that each arm must be considered as two separate components, namely the upper arm and the lower arm. The upper and lower arms must be considered as separate components because any bend in the elbow joint will cause the lower arm to travel at a faster angular velocity than the upper arm. In addition to these extra components, the human body cannot be considered as a point scatterer. Each point along the arm will contribute its own Doppler frequency shift and will be proportional to the location of that point on the arm. The components that are closer to the end of the arm will produce larger Doppler frequency shifts because this point on the

arm is traveling faster than a point on the arm that is close to the shoulder joint (where the radial velocity is zero). It is also evident from the plots that the mm-wave radar produces much larger Doppler frequency shifts and also allows more of the motion's details to be captured by the radar.

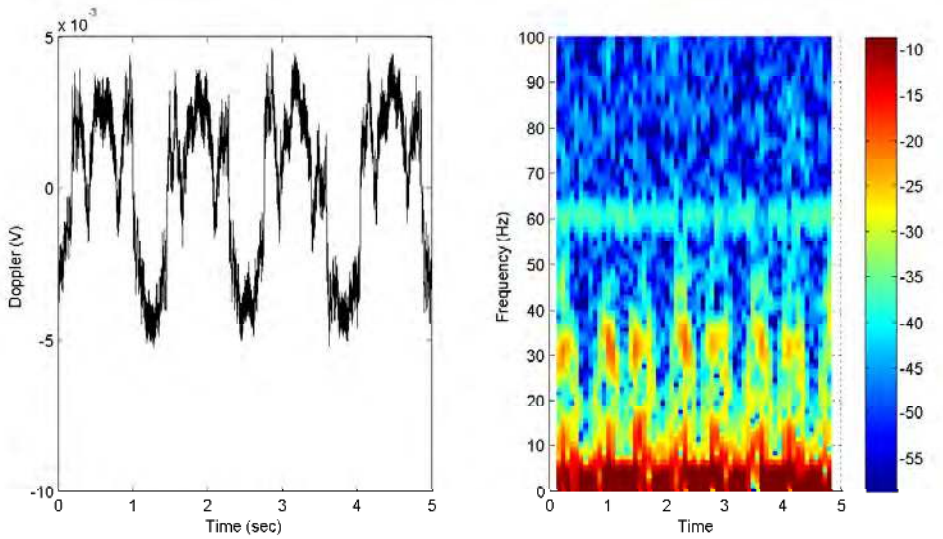

Figure 6.3: (Left) Experimentally measured micro-Doppler of a person swinging their arms and (Right) STFT of the micro-Doppler signal for an S-band radar.

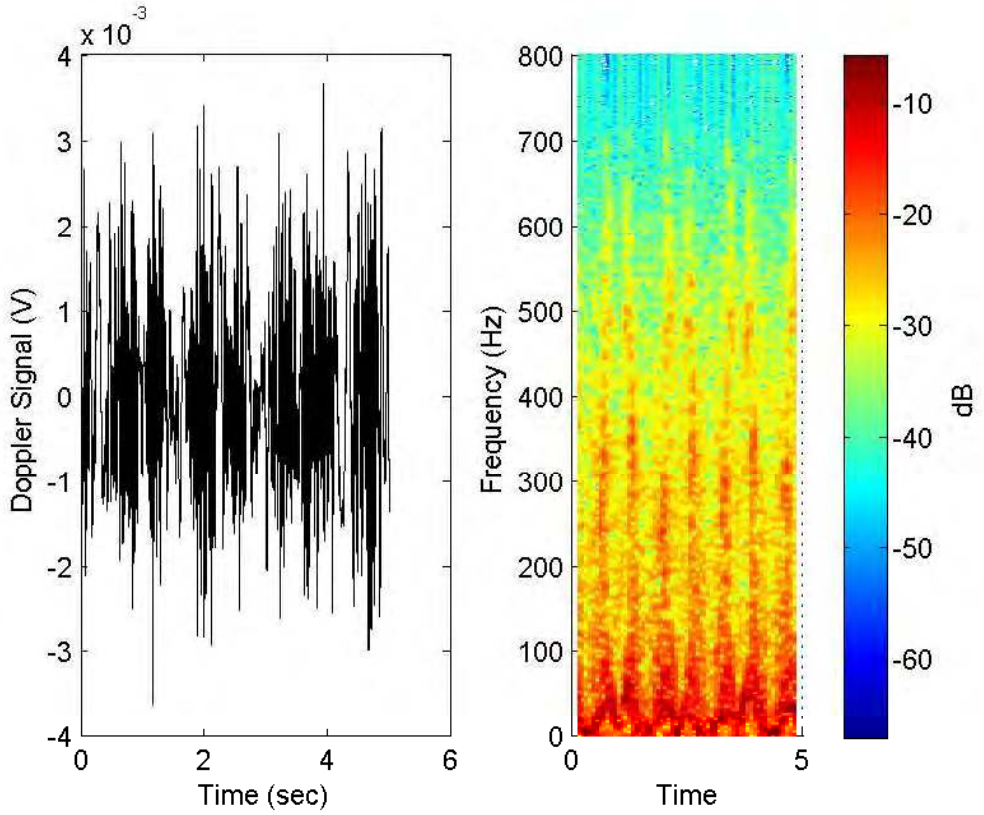

Figure 6.4: (Left) Experimentally measured micro-Doppler of a person swinging their arms and (Right) STFT of the micro-Doppler signal for a mm-wave radar.

Figures 6.5 and 6.6 show the micro-Doppler signature due to a human breathing with the two radars. This motion is very slow and therefore produces only very low frequency micro-Doppler signals. In this case the STFT does not have a high enough resolution to accurately determine the time-frequency characteristics of the signal. However, it is still clear that this motion is distinct from other human motions and is still distinguishable from background noise. The breathing motion mainly consists of a periodic expansion and contraction of the chest cavity. Other non-ideal components may arise from the human subject swaying either in an effort to maintain balance or the swaying may be inadvertent. It is also clear from these figures that breathing signals may be more easily extracted using the mm-wave radar if the time-frequency resolution can be improved by increasing the number of points and reducing the sampling frequency.

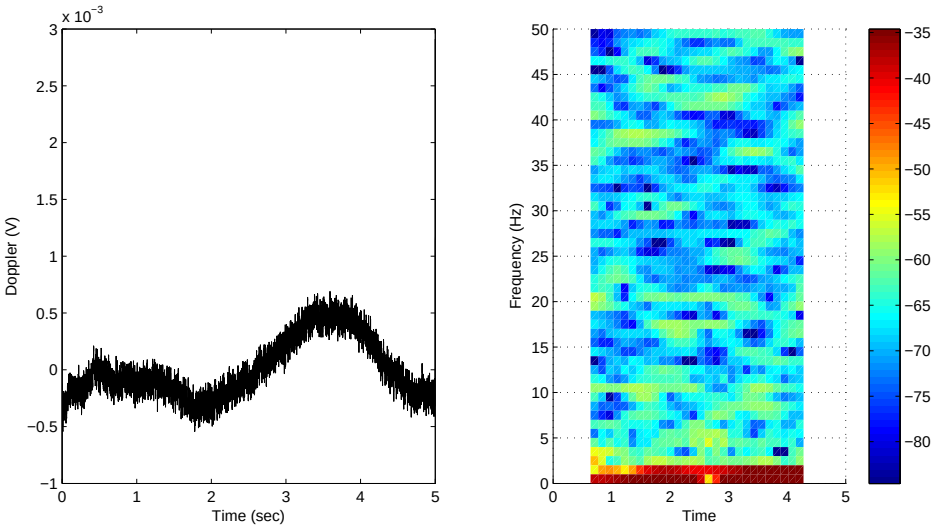

Figure 6.5: (Left) Experimentally measured micro-Doppler of a person breathing and (Right) STFT of the micro-Doppler signal for an S-band radar.

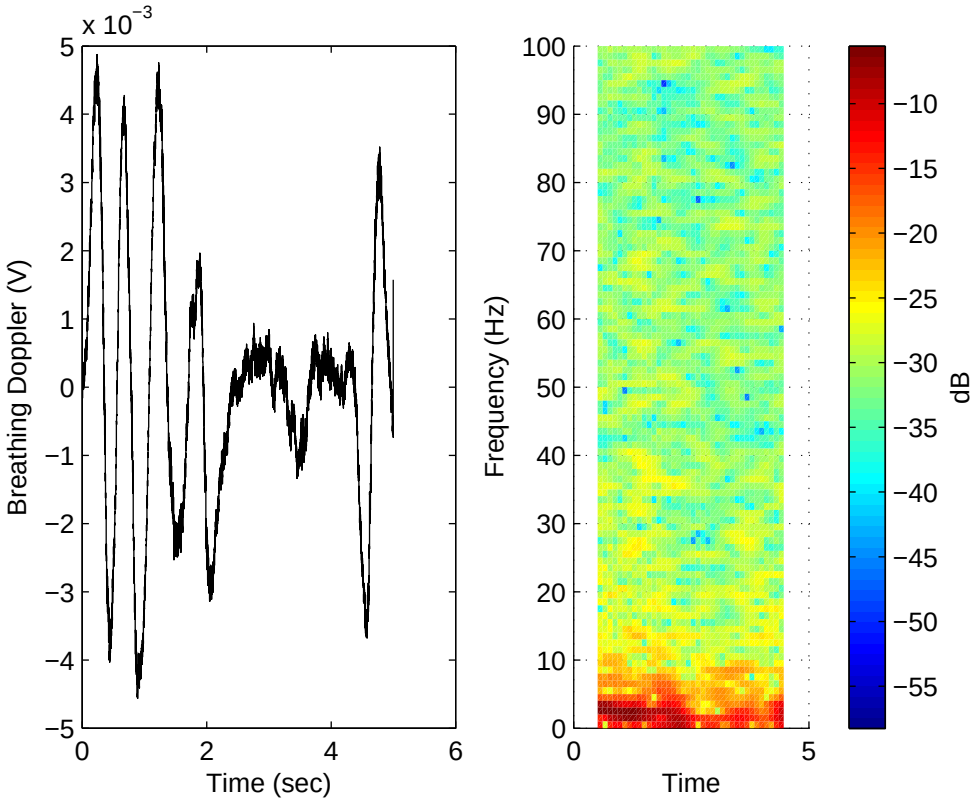

Figure 6.6: (Left) Experimentally measured micro-Doppler of a person breathing and (Right) STFT of the micro-Doppler signal for a mm-wave radar.

Figures 6.7 and 6.8 show the micro-Doppler signature due to a human picking up an object with the two radars. This motion is non-periodic and clearly shows an acceleration phase where the human bends at the waist and begins going toward the ground followed by a deceleration phase where the human eventually reaches zero velocity when they have reached the object on the ground. This acceleration and deceleration is then repeated for when the person returns to an upright position. Intuitively, many components contribute to this motion: bending at the waist, reaching of the arms toward the object, bending of the knees, etc. However, many of these components are small and may not be obvious when viewing the STFT.

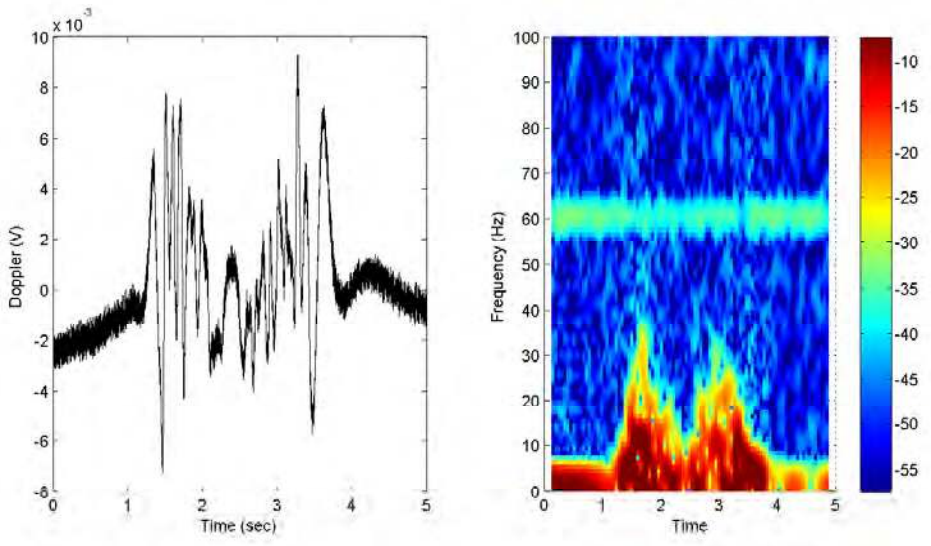

Figure 6.7: (Left) Experimentally measured micro-Doppler of a person picking up an object and (Right) STFT of the micro-Doppler signal for an S-band radar.

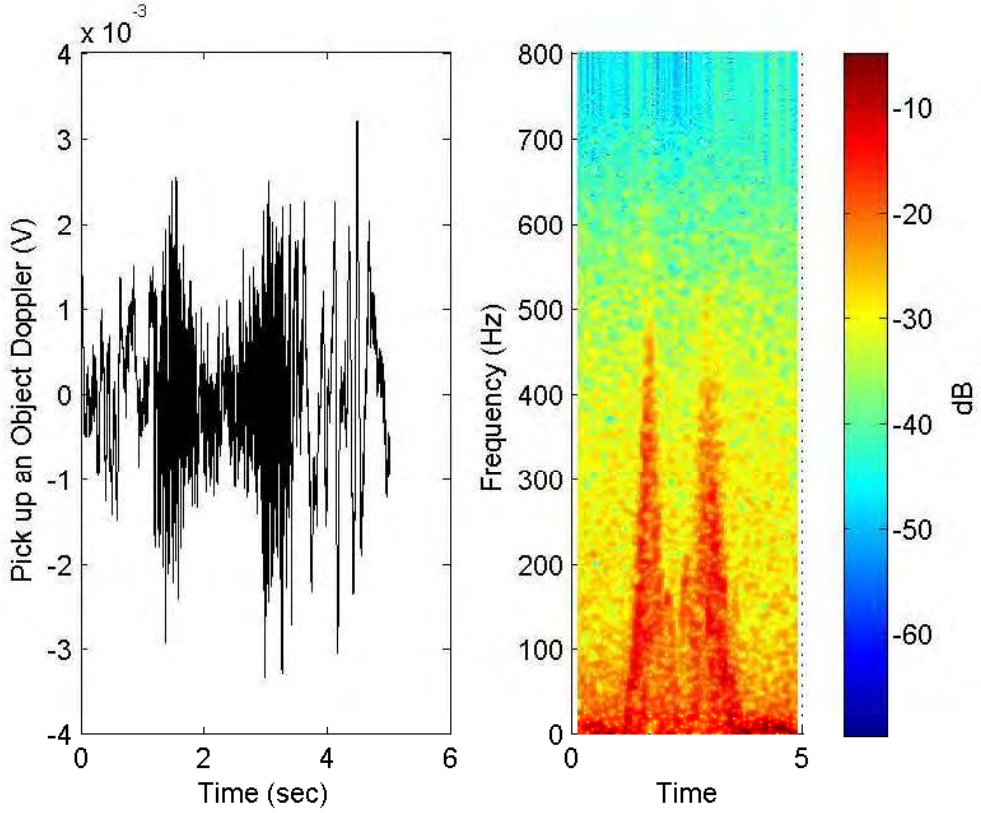

Figure 6.8: (Left) Experimentally measured micro-Doppler of a person picking up an object and (Right) STFT of the micro-Doppler signal for a mm-wave radar.

Figures 6.9 and 6.10 show the micro-Doppler signature due to a human transitioning from a crouching position to a standing position with the two radars. This motion is very similar to the motion of picking up an object, except that the human is already starting at a position close to the ground. Because of this, the human body only goes through one acceleration-deceleration cycle and this is clearly seen in the STFT of the crouching to standing micro-Doppler signal. As in the case of picking up an object, other body motions contribute to the signal, but may not have a large effect. Because the person is crouching, the bending of the knees may play a more significant role in the micro-Doppler signature of transitioning from crouching to standing than in picking up an object. However, this contribution is still small compared to the very large contribution of the torso. As was the case with a human swinging arms, these figures and the figures above for picking up an object demonstrate that more detail can be seen in the mm-wave Doppler signals

than in the S-band Doppler signals.

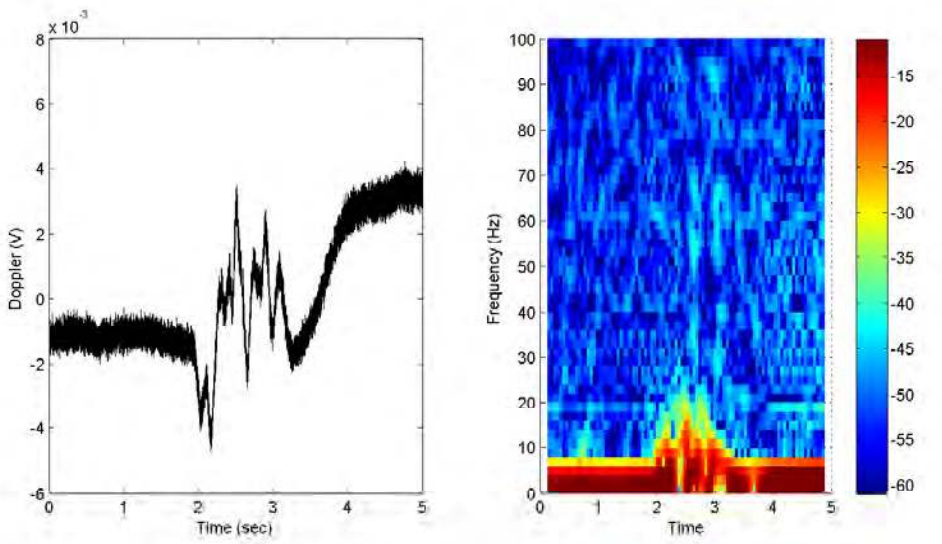

Figure 6.9: (Left) Experimentally measured micro-Doppler of a person transitioning from crouching to standing and (Right) STFT of the micro-Doppler signal for an S-band radar.

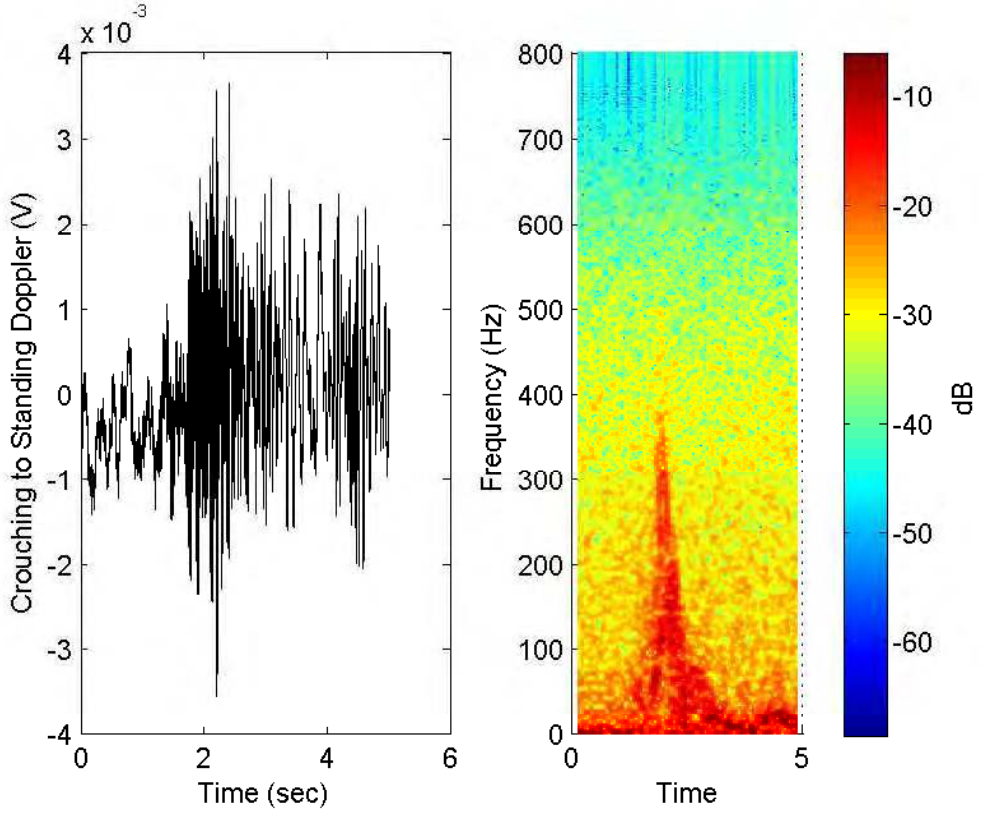

Figure 6.10: (Left) Experimentally measured micro-Doppler of a person transitioning from crouching to standing and (Right) STFT of the micro-Doppler signal for a mm-wave radar.

Similar experimental data has been obtained for various human motions using a 750 MHz radar [6]. The lower carrier frequency means that lower Doppler frequencies are observed; however, similar characteristics are found in these data as was found in the data for the S-band radar above. The results obtained are shown in Figure 6.11. Both the raw micro-Doppler and the energy of each IMF from EMD processing are shown. The micro-Doppler signals of Figure 6.11 also show that the micro-Doppler signatures are similar for different stand-off distances.

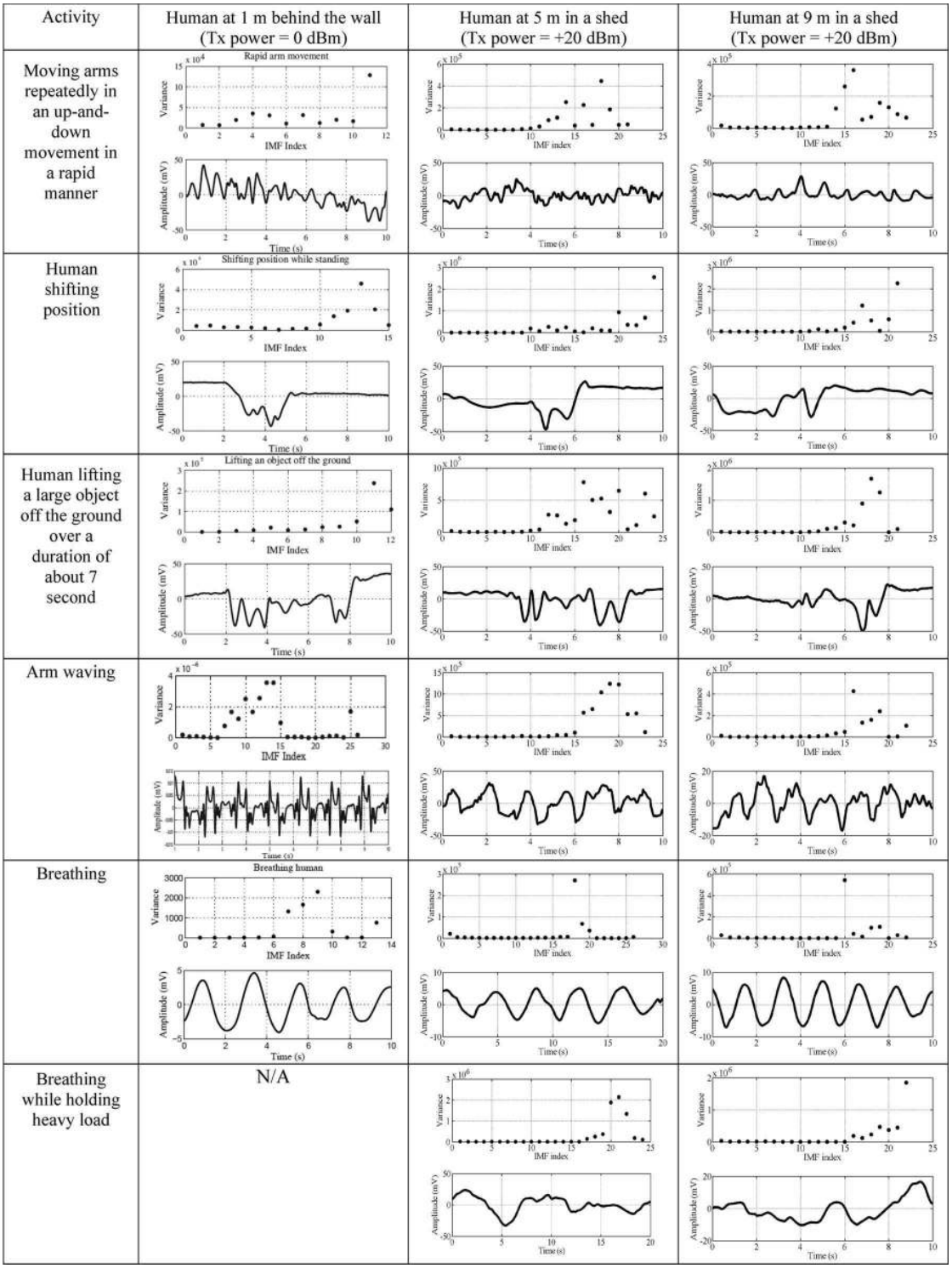

Figure 6.11: Micro-Doppler characteristics of various human activities [6].

Additional information on human motions, including the motions of breathing

and heartbeat, can be found in [19, 46, 47, 48, 49, 50, 51, 52, 53, 54, 55, 56, 57]. Many of these show the ability of radars to detect vital signs for medical applications and many of these specifically are designed to operate in a through-wall environment.

6.2 Models of Simple Human Motions

Micro-Doppler Signal of a Pendulum

The first motion that is considered is that of a person swinging their arms. This motion is similar to that of a pendulum, therefore it will be used as a building block to create the swinging arm model. The pendulum is among the simplest of periodic motions that can be considered when discussing micro-Doppler. The motion of a pendulum is governed by the laws of physics and can be represented by the second order differential equation:

$$f(t) = \frac{d^2\theta}{dt^2} + \frac{\gamma}{ml} + \frac{g}{l}\sin(\theta). \tag{6.1}$$

For the moment, we consider only when the forcing function $f(t)$ is zero. The initial conditions determine the starting angle and velocity of the pendulum, but once these are set, gravity and resistive forces such as friction become the only factors in the motion of the pendulum. The solution to this differential equation is a damped sinusoid of the form: $\exp(-\alpha t)\cos(\omega t)$. The damping coefficient, α is related to the frictional forces acting on the pivot point. Using this equation of motion, the range of the pendulum from the radar is calculated and the Doppler phase shift is calculated using the well-known expression: $\phi(t) = \frac{4\pi r(t)}{\lambda}$. Because the angle of the pendulum is constantly changing and the distance to the radar is also changing as the pendulum swings, the radar cross section (RCS) and the relative receive power must be accounted for (via the radar range equation) in the model. Assuming a monostatic radar configuration, the RCS of a flat plate is:

$$\sigma = 4\pi\left(\frac{ab}{\lambda}\right)^2 \cos\theta_i{}^2 \left[\frac{\sin\left(\beta b\sin\theta_i\right)}{\beta b\sin\theta_i}\right]^2. \tag{6.2}$$

At normal incidence ($\theta = 0°$), this expression reduces to the well-known ex-

pression of the RCS of a flat plate:

$$\sigma = 4\pi \left(\frac{ab}{\lambda} \right)^2 \tag{6.3}$$

Because a flat plate exhibits only a single scattering center, we will consider radar returns occurring from scattering at the antenna height, which in our experiments and for the purposes of this model, is located at half the length of the pendulum from the pivot point. Using a constant height for the scattering center of the pendulum and using simple geometry, the radial distance from the pendulum to the radar is:

$$r(t) = R_0 + \frac{L}{2} \tan\theta \tag{6.4}$$

where R_0 is the distance to the pendulum at normal incidence and L is the length of the pendulum.

The resulting simulated Doppler signal is shown in Figure 6.12. Comparing this signal to the experimentally measured signal in Figure 6.1, we observe good agreement with real data.

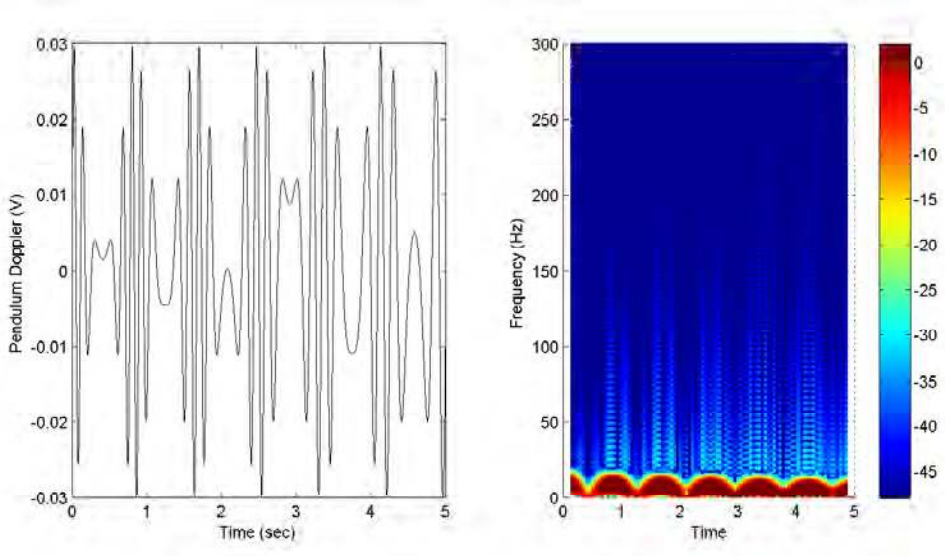

Figure 6.12: (Left) Simulated micro-Doppler of a pendulum and (Right) STFT of the simulated micro-Doppler signal of the pendulum for an S-band radar.

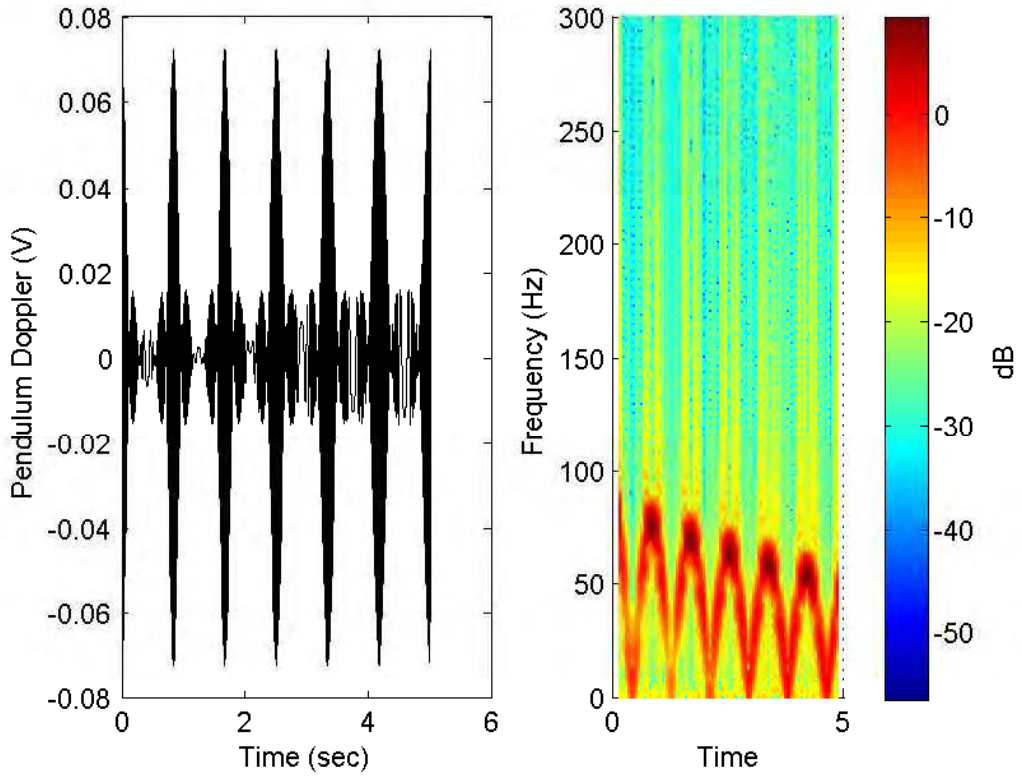

Figure 6.13: (Left) Simulated micro-Doppler of a pendulum and (Right) STFT of the simulated micro-Doppler signal of the pendulum for a mm-wave radar.

Swinging arms

A human swinging their arms performs a more complex motion, which is confirmed based on the time-frequency characteristics of the signal. The swinging arm causes the torso to sway in order for the person to maintain balance. Furthermore, the arm itself contains multiple components due to the shoulder and elbow joints. In [58], arm motion is discussed, where the arm moves vertically from one position to another. This motion is much different than that of a person swinging their arms continuously; however, it allows us to gain some insight into the biomechanics of the human arm. The angle between the upper arm and the vertical is modeled as sinusoidal movement with a frequency of 0.7 Hz, similar to a simple pendulum. The torso is also modeled as swaying sinusoidally, but the torso movements are 180° out of phase with the arm angle. The lower arm angle relative to the upper

arm is modeled as moving in a Gaussian trajectory. Based on our observations on four volunteers with different physical characteristics, this appeared to be a reasonable estimation of the lower arm motion. In most cases, our test subjects kept their arms straight for the majority of the swinging motion and only bent their elbows near the forward most point of the swing. The Gaussian trajectory also allows for the elbow joint to maintain a positive angle relative to the upper arm, keeping with the physical limitations of the human body. Our simulation uses a standard deviation of 0.14 seconds for the Gaussian trajectory of the lower arm. Once the angular trajectory of the arm is established, the Doppler phase shift can then be calculated using the well-known expression: $\varphi_d = \frac{4\pi r(t)}{\lambda}$ where $r(t)$ is the distance to the radar. This distance can be calculated as: $r(t) = L\sin(\theta)$, where L is the length of the arm segment and θ is the angle of the arm relative to vertical. The simulated micro-Doppler signals and the STFTs for both the S-band and mm-wave radars are shown in Figure 6.14 and 6.15.

Because each point on the body causes a Doppler frequency shift, the STFT plot should appear "filled in." To simulate this, 10 randomly located points are selected on the upper arm and 25 random points are selected on the lower arm for calculation of Doppler frequencies. Close inspection of Figure 6.15 shows that each of these points places a line on the STFT plot, and if more points are included, this will cause the simulation to even more closely resemble experimental data.

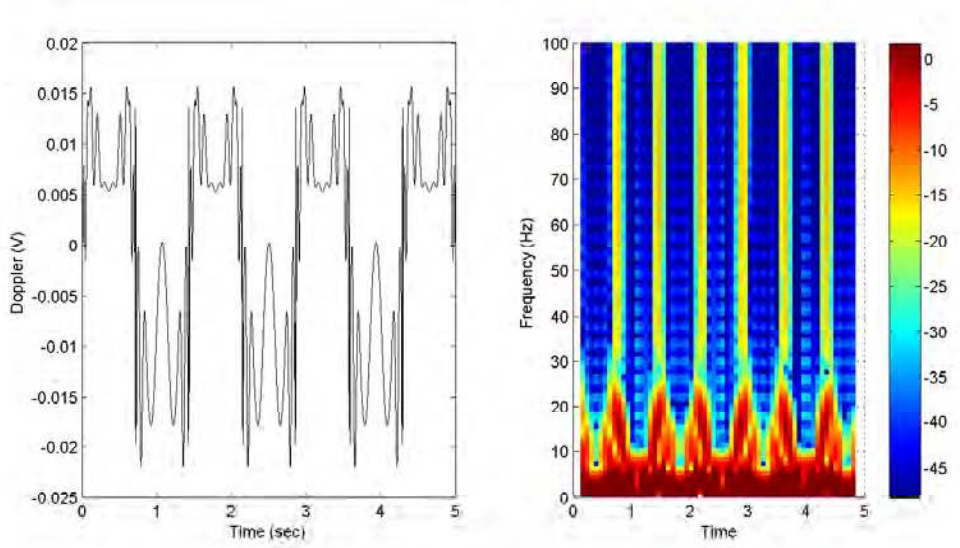

Figure 6.14: (Left) Simulated micro-Doppler of swinging arms and (Right) STFT of the simulated micro-Doppler signal for an S-band radar.

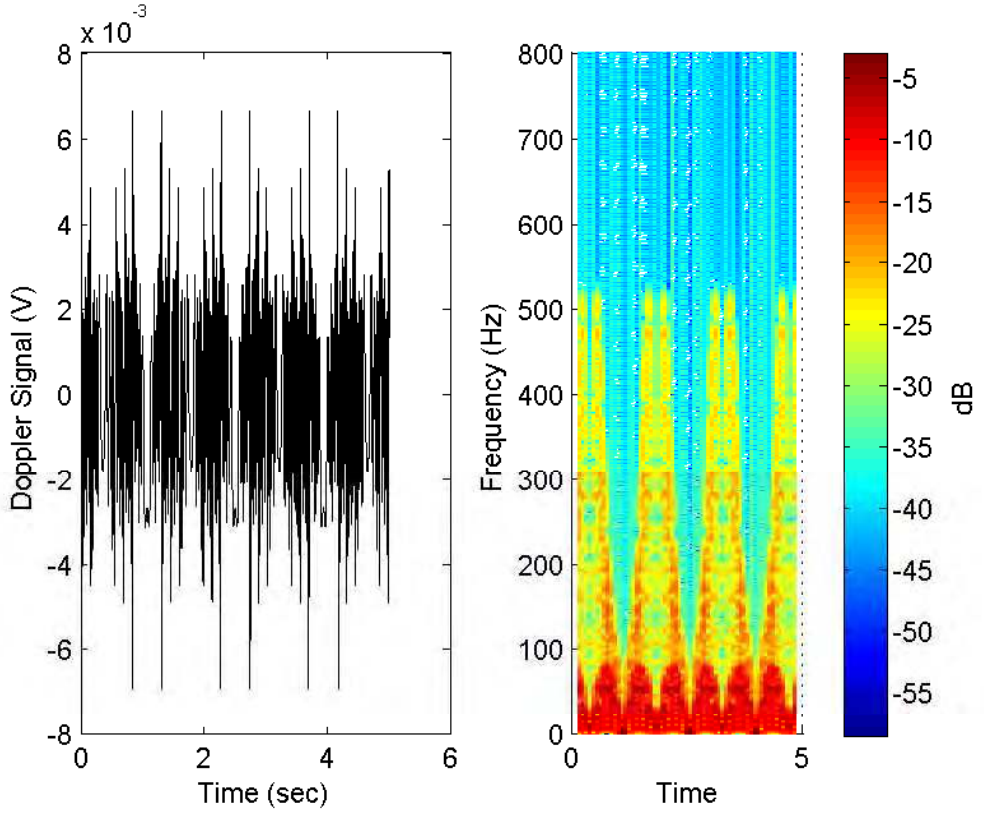

Figure 6.15: (Left) Simulated micro-Doppler of swinging arms and (Right) STFT of the simulated micro-Doppler signal for a mm-wave radar.

Breathing

A human breathing entails a fairly simple periodic motion of the chest cavity with one breathing cycle (inhalation and exhalation) completed in about 5 seconds. The most complex part of simulating the chest cavity expansion and contraction is the fact that breathing does not exhibit purely sinusoidal motion. For a normal person, the chest cavity stops for a short pause after exhaling for about 1 second [59]. In order to simulate this motion, a sine wave was first created, which was "flattened" at a point below a certain threshold (-0.2 in this case). The "flattened signal" was then filtered to produce a smooth motion. The RC filter used for smoothing is has the discrete-time transfer function:

$$H(z) = \frac{\alpha}{z - (1 - \alpha)} \tag{6.5}$$

where $\alpha = \frac{T}{T+\tau}$ and T is the sampling time. By adjusting the time constant, the desired rise time and fall time can be achieved to closely match the motion of a human breathing. This simulation uses a time constant of $\tau = RC = 0.6$ with a time length of 5 seconds. The time constant was adjusted manually so that the transitions during inhalation and exhalation were smooth and the displacement of the simulated chest wall closely matched our observations. Forward and reverse filtering produces symmetry. The resulting chest displacement and an illustration of the chest cavity expansion and contraction are shown in Figure 6.16.

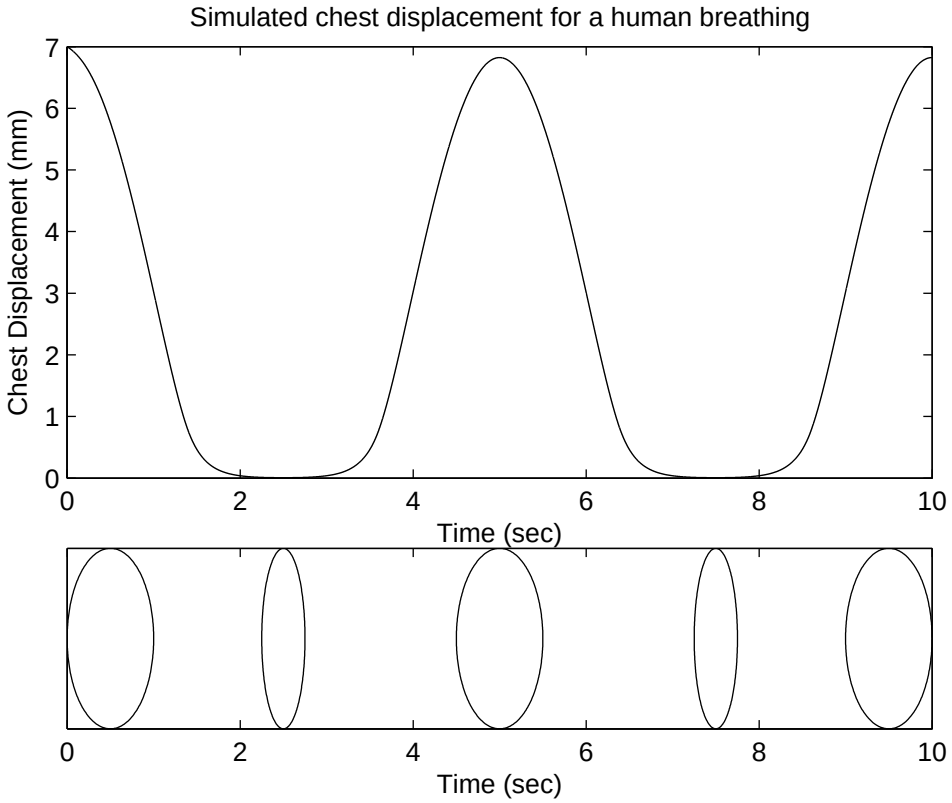

Figure 6.16: (Top) Simulated chest displacement for a human breathing and (Bottom) illustration of chest expansion and contraction.

The simulated micro-Doppler signals and the STFTs of the signals for both the S-band and mm-wave radars are shown in Figures 6.17 and 6.18. The simulation plots clearly show the difficulty of identifying breathing using the STFT. Because breathing contains very small Doppler frequency shifts, the STFT has difficulty in

resolving the frequency changes that occur during this motion.

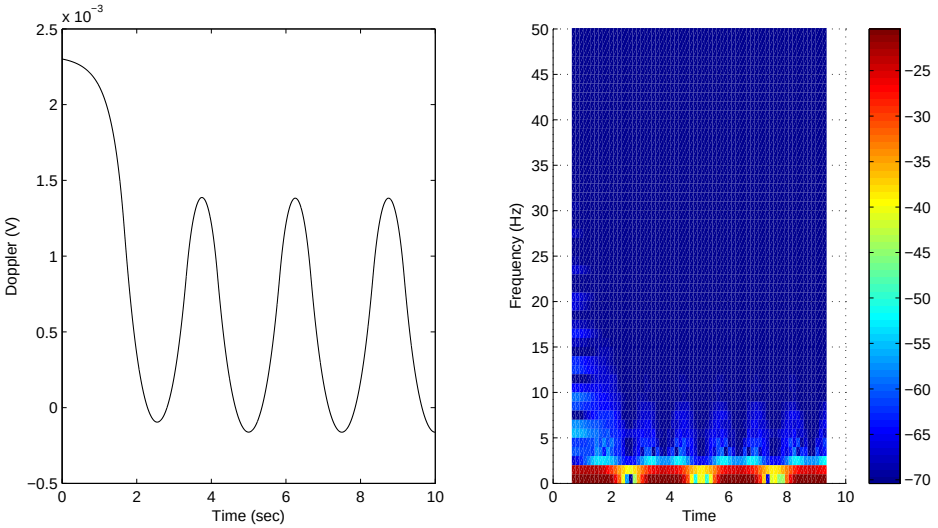

Figure 6.17: (Left) Simulated micro-Doppler of breathing and (Right) STFT of the simulated micro-Doppler signal for an S-band radar.

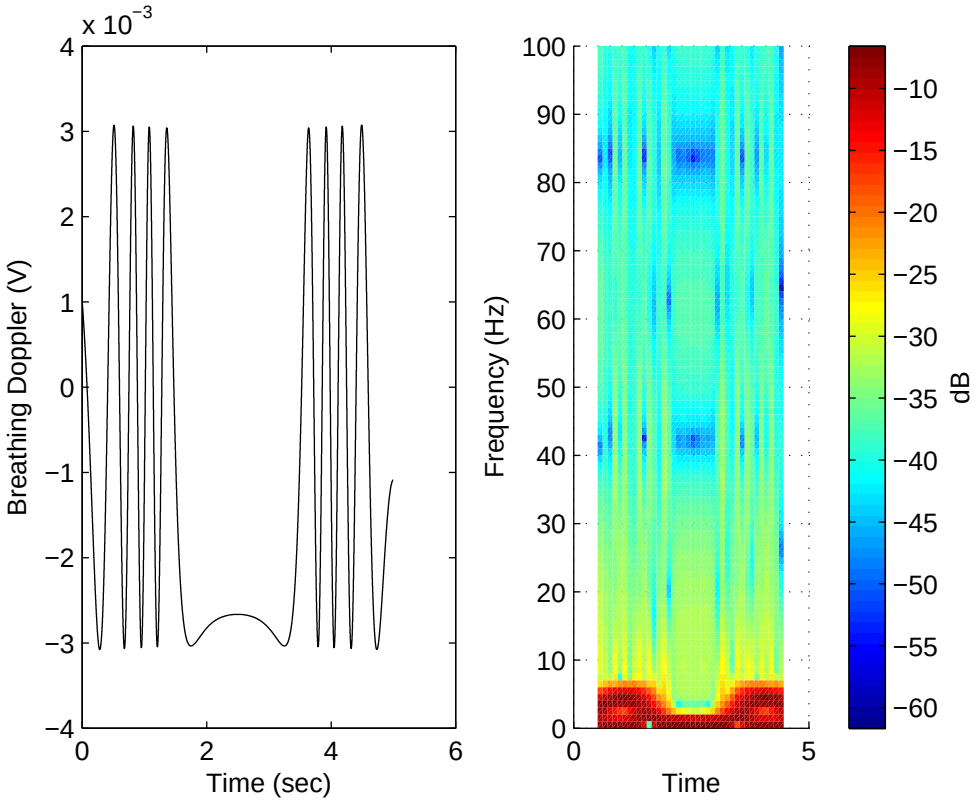

Figure 6.18: (Left) Simulated micro-Doppler of breathing and (Right) STFT of the simulated micro-Doppler signal for a mm-wave radar.

Picking up an object

The motion of picking up an object from the ground differs from the previous motions because it is non-periodic. Due to the complexities of this motion (torso bend, knee bend, ankle bend, arm motion, bending of the back, etc.), we expect wide variability between individuals performing this motion. This is true of all of the motions considered; however, this motion is especially dependent on these intricacies. Even so, for simplicity, the simulation of this motion will consider only the movement of the torso. The time taken between starting from a standing position, bending the torso to a horizontal position to pick up the object, and returning to the standing position is 3 seconds. The angle between the torso and vertical is modeled as Gaussian with a width parameter of 0.5 seconds. A Gaussian representation ensures that the torso begins at 0°, reaches its maximum angle, and

returns to 0°. For the purposes of this simulation, the torso is modeled as straight, bending only at the waist, and achieving a maximum angle of 90°. Figure 6.19 illustrates the simulated angular trajectory of the torso. The simulated micro-Doppler signal and the STFT of the signals for both the S-band and mm-wave radars are shown in Figures 6.20 and 6.21. The STFT plots clearly show the acceleration that occurs on the descending and ascending motions and also the pause that occurs when the torso changes direction. The result is two cycles of acceleration followed by deceleration.

As was the case with swinging arms, each point on the body causes a Doppler frequency shift. Again, 25 randomly located points are selected along the length of the upper torso for calculation of Doppler frequencies. If more points are included this will cause the simulation to even more closely resemble experimental data.

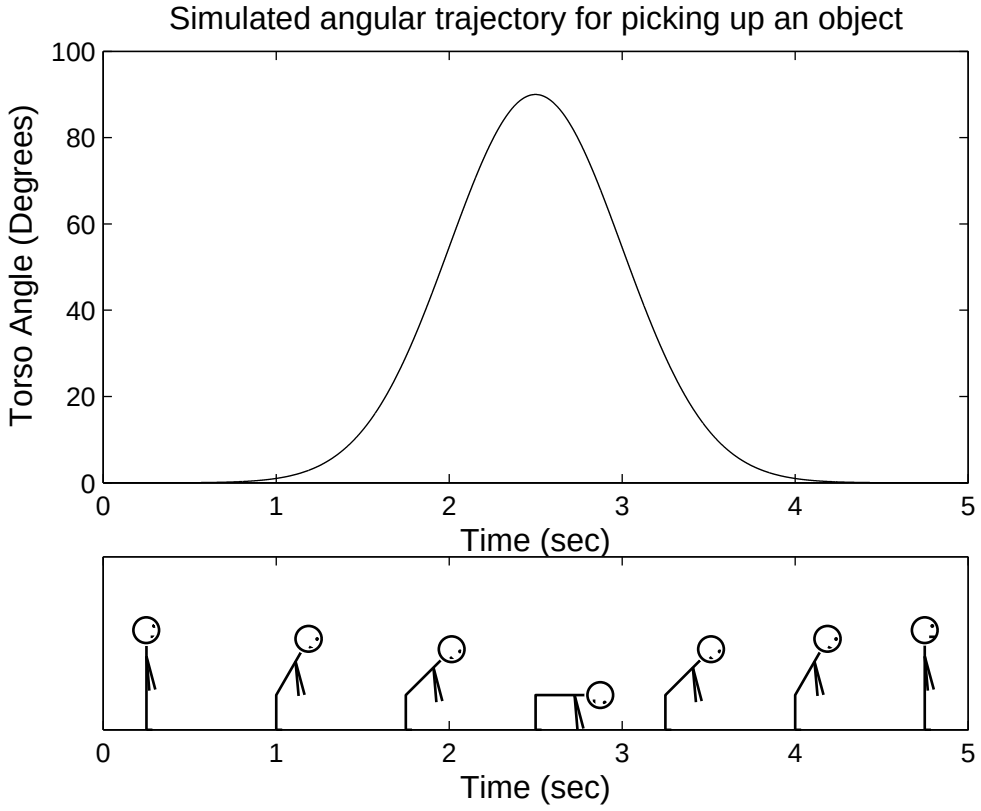

Figure 6.19: (Top) Simulated angular trajectory of a human picking up an object and (Bottom) side view of the motion.

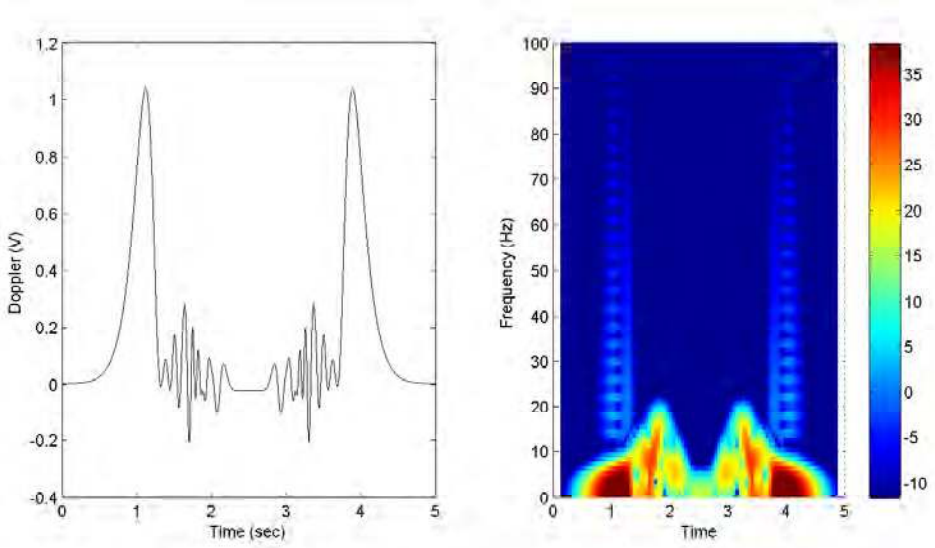

Figure 6.20: (Left) Simulated micro-Doppler of picking up an object and (Right) STFT of the simulated micro-Doppler signal for an S-band radar.

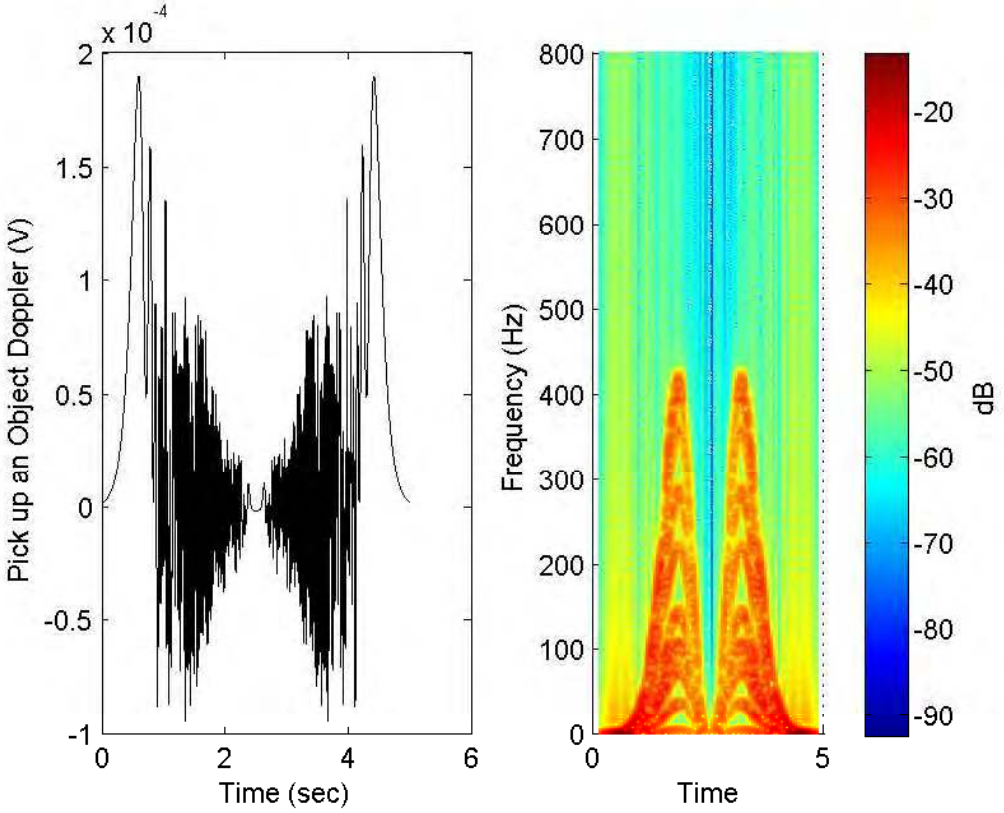

Figure 6.21: (Left) Simulated micro-Doppler of picking up an object and (Right) STFT of the simulated micro-Doppler signal for a mm-wave radar.

Transitioning from crouching to standing

The motion of transitioning from crouching to standing is similar in nature to picking up an object. For picking up an object, there were two full cycles of acceleration followed by deceleration. For transitioning from crouching to standing, the descending motion of the torso does not take place and the STFT should only complete one cycle of acceleration and deceleration. The time taken between the crouching position with the knees bent to the standing position is 3 seconds. In order to model this motion, a Gaussian trajectory cannot be used because it would have the same time-frequency characteristics as picking up an object. Instead, the motion is modeled as a sigmoid-like function. The equation that is used for this simulation is:

$$\theta(t) = \frac{\theta_0}{2}\left[1 - \text{erf}\left(\frac{t - t_0}{\sigma\sqrt{2}}\right)\right]. \tag{6.6}$$

where $\text{erf}(t)$ is the error function and $\theta_0 = 90°$ is the initial torso angle.

Since we are using this function to model the motion, it means that the angular velocity of the torso is modeled as a Gaussian instead of modeling the torso angle as Gaussian. This is a reasonable assumption because when humans move their arm from one position to another, the tangential velocity is approximately Gaussian [58]. This can reasonably be extended to other human motions, such as standing up from a crouching position, where the body transitions from one location to another. This simulation uses $\sigma = 0.4$ seconds and $t_0 = 2.5$ seconds so that the motion is at the center of the time window. Figure 6.22 illustrates the simulated angular trajectory of the torso. The simulated micro-Doppler signals and the STFTs for both the S-band and mm-wave radars are shown in Figures 6.23 and 6.24.

As was the case with swinging arms and picking up an object, each point on the body causes a Doppler frequency shift. Again, 25 randomly located points are selected along the length of the upper torso for calculation of Doppler frequencies. If more points are included this will cause the simulation to even more closely resemble experimental data.

Here, we note that this model for transitioning from crouching to standing is a very simple model. The motions of the legs and arms are not considered for simplicity. Nevertheless, an excellent match between the simulation results and the experimental data is clearly observed, which validates the phenomenological approach used in our simulation procedure. In [60], standing up from a crouching position is discussed in more detail from the perspective of an optimal control problem. A similar motion, transitioning from sitting to standing, is discussed in detail in [61, 62].

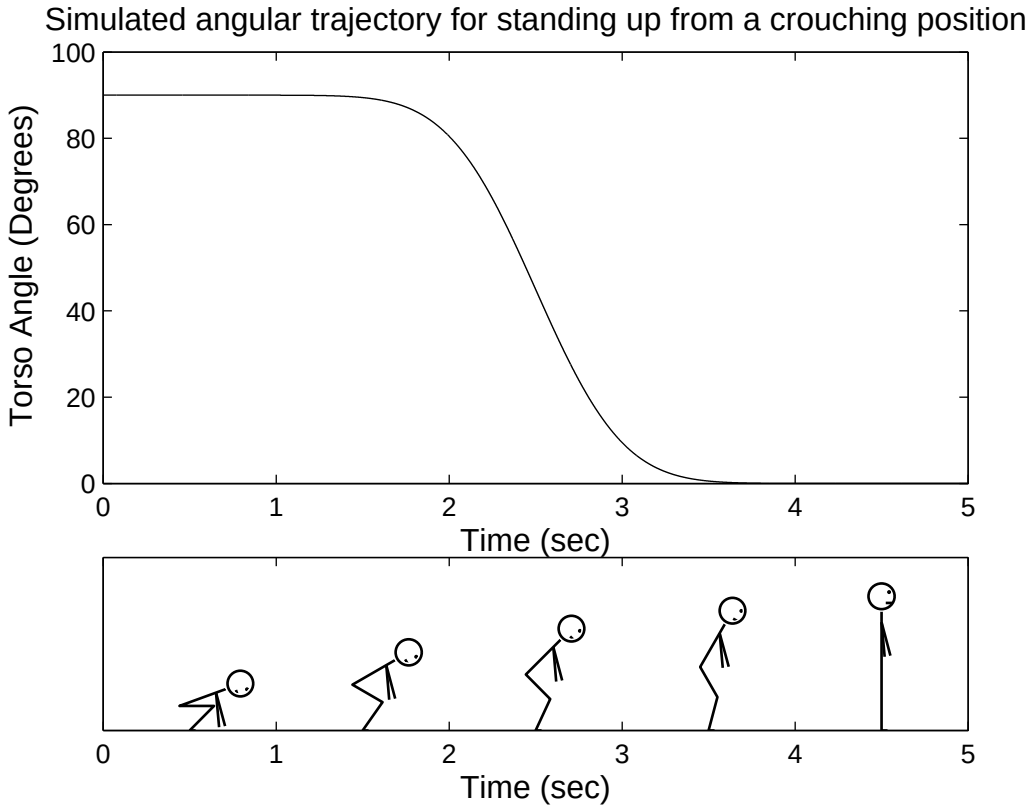

Figure 6.22: (Top) Simulated angular trajectory of a human standing up from a crouching position and (Bottom) side view of the motion.

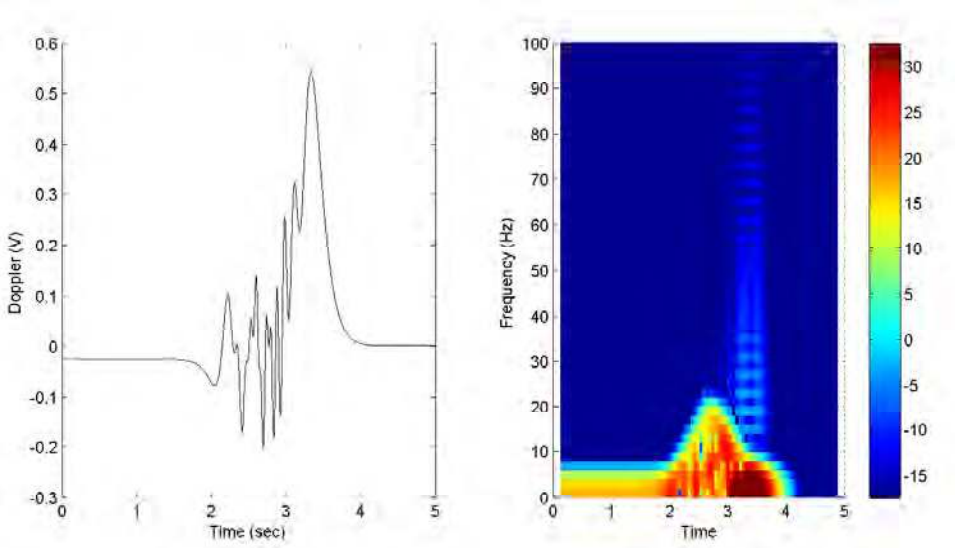

Figure 6.23: (Left) Simulated micro-Doppler of transitioning from crouching to standing and (Right) STFT of the simulated micro-Doppler signal for an S-band radar.

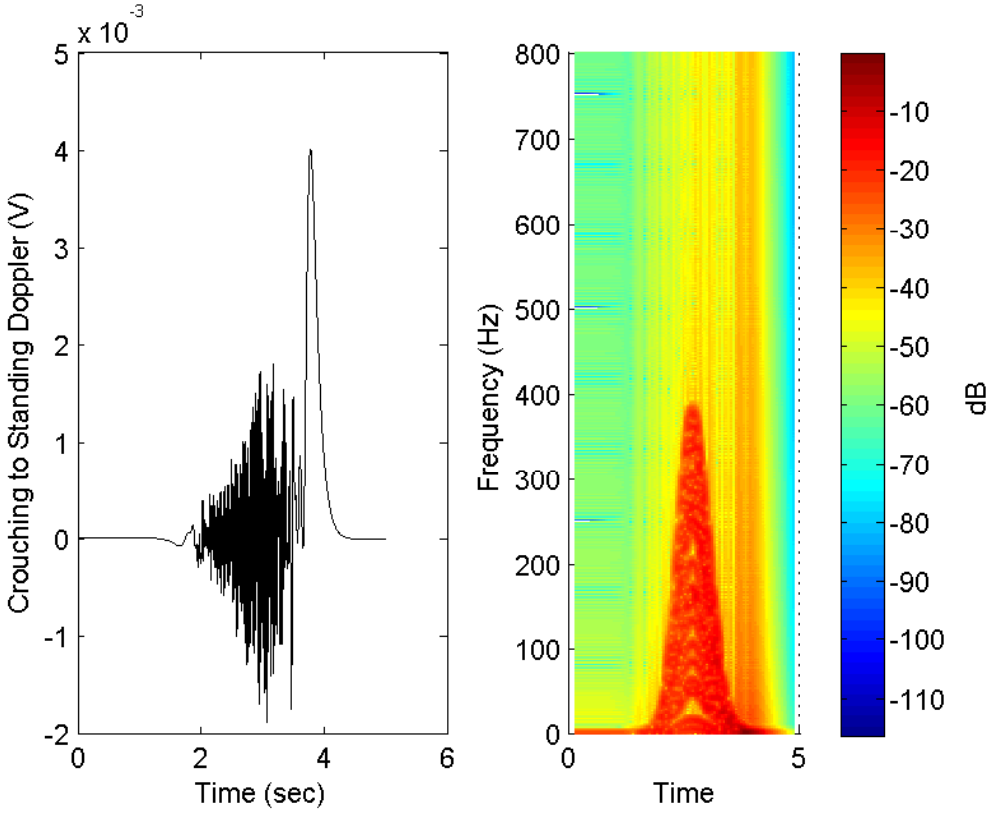

Figure 6.24: (Left) Simulated micro-Doppler of transitioning from crouching to standing and (Right) STFT of the simulated micro-Doppler signal for a mm-wave radar.

6.3 Comparison of Through-the-Wall vs. Non-Through-the-Wall micro-Doppler Signatures

In order to visualize how a wall affects micro-Doppler signatures, two examples are briefly discussed now. The first example compares the micro-Doppler due to a pendulum for both through-wall and barrier-free situations. This is shown in Figure 6.25. The second example is of a human target that is swinging their arms. The human comparison for swinging arms is shown in Figure 6.26. As expected, for both examples, the SNR is significantly reduced and the wall has introduced an additional DC offset to the signal. The wall clearly adds an additional DC component to the signal; however, the signal without a wall still has a DC offset

due to antenna coupling, multipath, and the constant distance, R_0 from the radar to the center point of the target's swing motion.

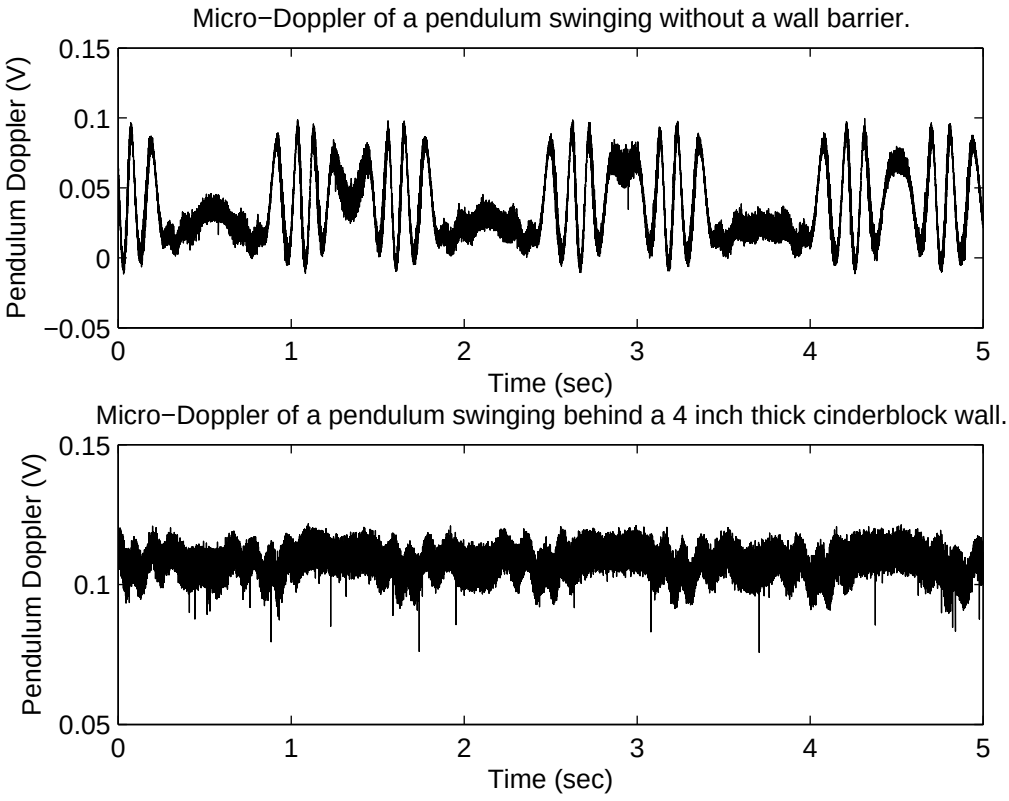

Figure 6.25: Comparison of the micro-Doppler signal of a pendulum (Top) without a wall barrier and (Bottom) with a wall barrier.

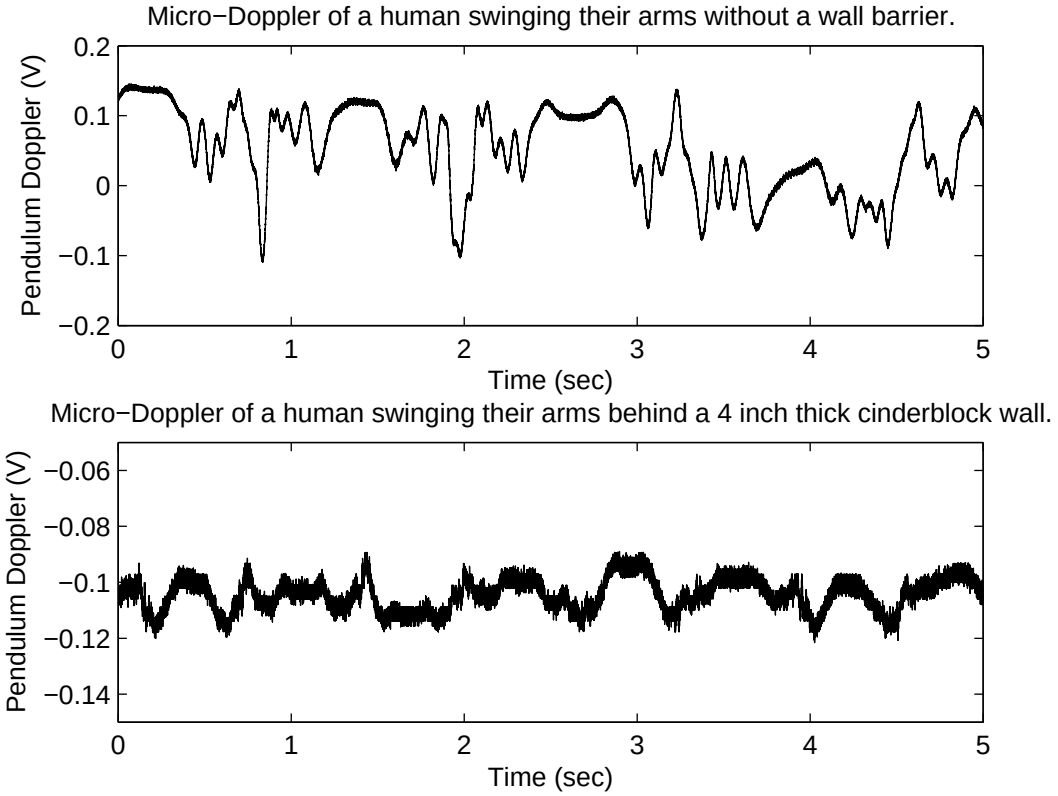

Figure 6.26: Comparison of the micro-Doppler signal of a pendulum (Top) without a wall barrier and (Bottom) with a wall barrier.

If the classification of motions is desired, there are additional factors that must be considered. To illustrate this, see Figures 6.27 and 6.28. Figure 6.27 compares the energy of each IMF produced by EMD for a pendulum both with and without a wall barrier. Figure 6.28 shows the same comparison, but with a person swinging their arms. The raw micro-Doppler signals that produced these energy plots are the same as in Figures 6.25 and 6.26.

In each energy plot comparison, the energy is greatly reduced by the presence of the wall. This is expected based on the discussions in Sections 2.3.1 and 2.3.4. If the energy of each IMF of a signal is to be used as a feature vector for classification, the amplitudes of each are critical to the accuracy of the classifier. Training a classifier under a scenario without a wall barrier, may not produce accurate results if the test data are taken from a through-wall scenario. For this reason, the classifier must be trained and tested under the appropriate conditions and it is important

to understand its limitations.

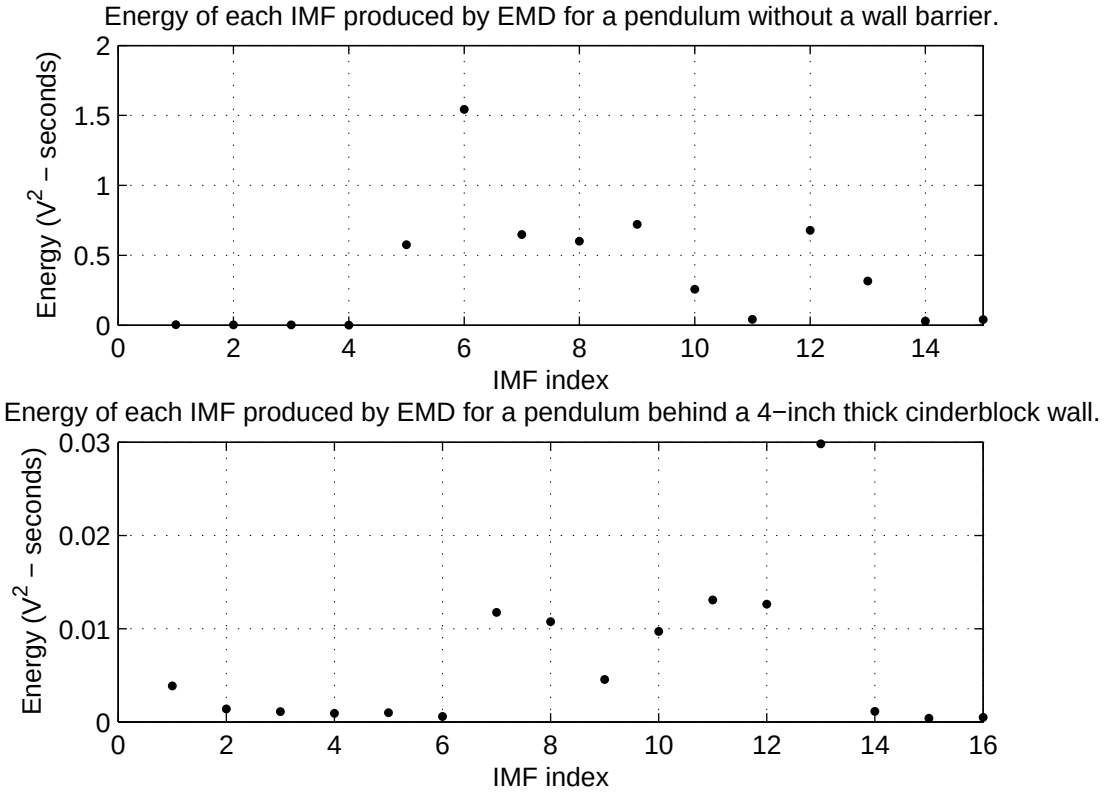

Figure 6.27: Comparison of the energy of each IMF produced by EMD for a pendulum (Top) without a wall barrier and (Bottom) with a wall barrier.

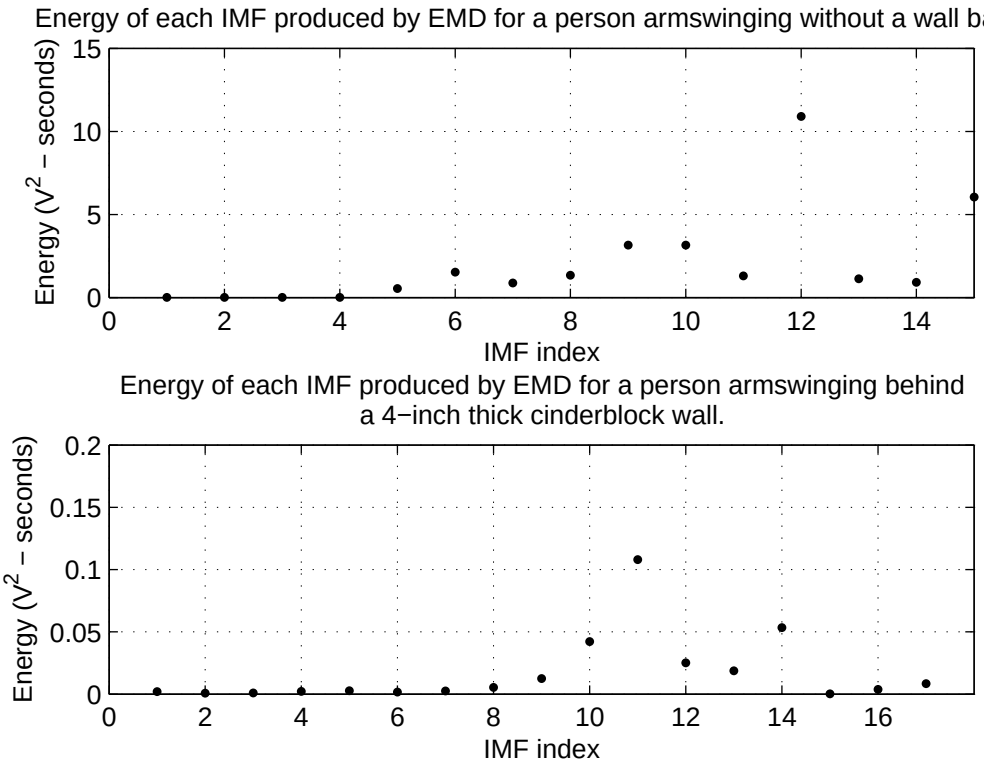

Figure 6.28: Comparison of the energy of each IMF produced by EMD for a person swinging arms (Top) without a wall barrier and (Bottom) with a wall barrier.

6.4 Adding Randomness to Human Motion Simulations

The simulated human movements described in Section 6.2 confirm that the experimental data is valid and provide some useful insights into how simple motions are performed. However, human motions cannot be perfectly repeated and the equations used to model them are only approximations of what really happens. For this reason, we are also interested in adding randomness to the human motion simulations.

The main objective is to model the motions with some randomness in the simulated angles. For swinging arms, this is the angle of the upper arms and the angle of the lower arms relative to vertical. For picking up an object and

transitioning from crouching to standing, this is the torso angle relative to vertical. However, some problems arise if Gaussian noise is added to the models. If noise is added, this causes micro-movements which change direction rapidly even though the macro-motion remains the same. These small changes in the direction of movement are not observed in reality because human gestures tend to transition smoothly from one point to another.

In order to add randomness to the human body angles in the simulations, while maintaining smooth transitions from one position to another, additive and multiplicative noise were not used. Instead, Gaussian noise was generated and convolved with the original angular trajectory. Figure 6.29 shows how this changes the angle for the pendulum simulation. The top plot shows the original angular trajectory and the bottom plot shows an example of the angular trajectory after convolution with a Gaussian noise vector of the same length as the angle vector. Figure 6.30 show the simulated micro-Doppler signal after adding randomness to the pendulum angle and the STFT of the signal for a mm-wave radar. It is clear from Figures 6.29 and 6.30 that the motion is no longer perfectly sinusoidal. Its shape has been distorted and the angle does not always reach its maximum during each cycle. Nevertheless, the micro-Doppler signal remains very similar to the micro-Doppler signal without any randomness (compare to Figure 6.13) and the STFT of the micro-Doppler signal has its repetitiveness preserved, with some distortion that corresponds to the distortion in the pendulum angle.

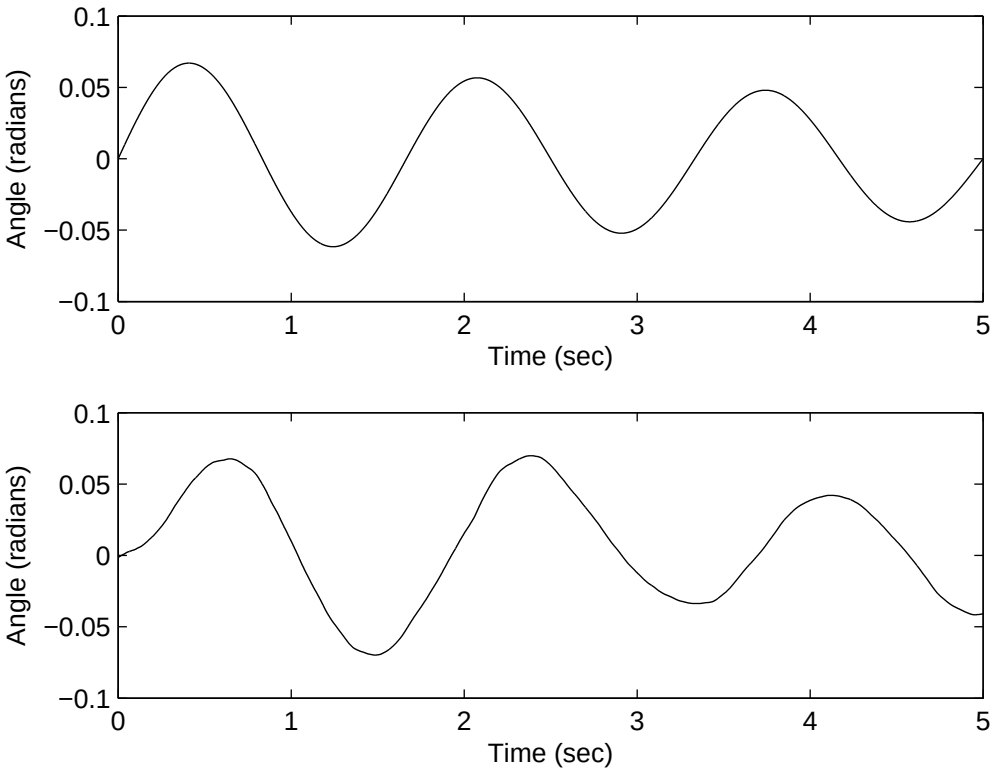

Figure 6.29: (Top) original angular trajectory for the pendulum simulation and (Bottom) angular trajectory for a pendulum after randomization.

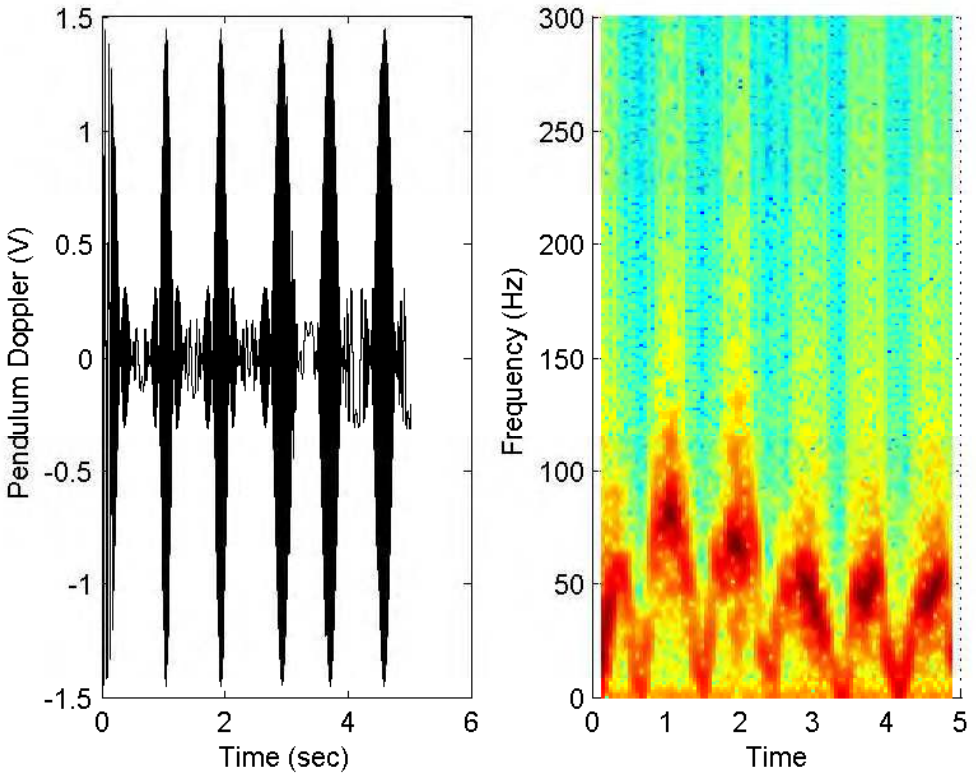

Figure 6.30: (Left) Simulated micro-Doppler of a pendulum with randomness added to the angle and (Right) STFT of the simulated micro-Doppler signal for a mm-wave radar.

Randomness has also been added to the swinging arms simulation. Gaussian noise is convolved with the angle vector for the upper arm. The results are shown in Figure 6.31. Again, the simulation results with randomness added closely resemble the original simulation results (compare to Figure 6.15) with slight variations that correspond to changes in the upper arm angle. Figure 6.31 illustrates the dependence of the lower arm movement on the upper arm. Randomness was not added to the lower arm angle (elbow joint), however the high frequency portions of the STFT plot that correspond to the forearm clearly show that the randomness in the upper arm angle has affected the lower arm as well as the upper arm.

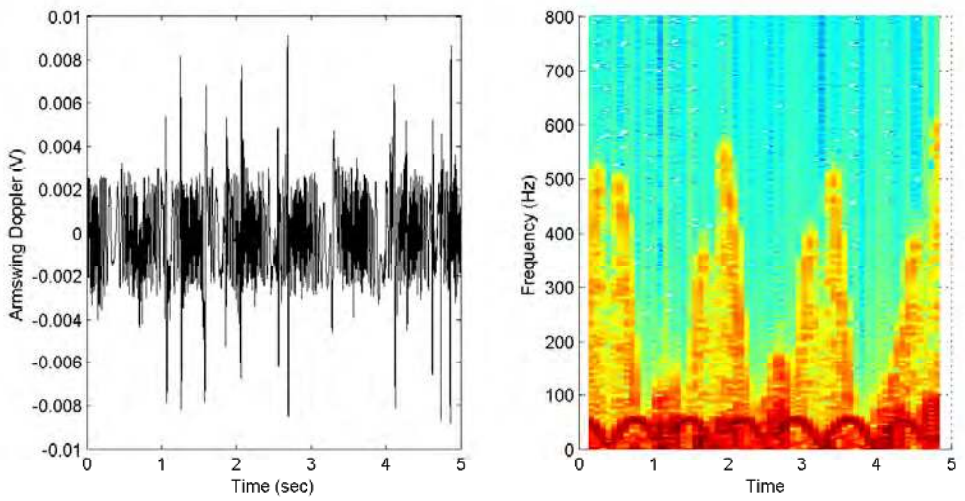

Figure 6.31: (Left) Simulated micro-Doppler of a human swinging arms with randomness added to the upper arm angle and (Right) STFT of the simulated micro-Doppler signal for a mm-wave radar.

Adding randomness to the motions of picking up an object and transitioning from crouching to standing was performed in a slightly different manner. If the same procedure as above is used, the angular trajectory of the torso loses its original shape. This is because small changes in the torso angle can cause large changes in the velocity when the velocity is low. In order to add randomness to the simulations, an additional "swaying" motion was added to the simulations. The angular trajectory of the torso remains the same, however, the range from the target to the radar has an additional sinusoidal swaying motion added to it. The amplitude of the swaying was 3 cm and had a frequency of 1/3 Hz. This simulates a person swaying to maintain balance, but this is a predictable motion. To add some randomness, a random phase angle is included in the sinusoidal swaying. Just like adding randomness to the pendulum, the swaying is then convolved with a Gaussian random noise vector. This allows the swaying motion to be non-repetitive and unpredictable. The results for picking up an object and transitioning from crouching to standing are shown in Figures 6.32 and 6.33 respectively.

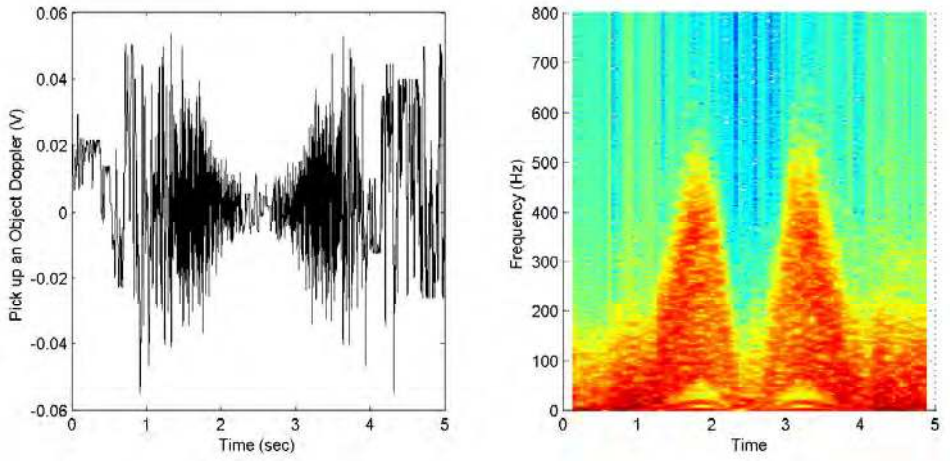

Figure 6.32: (Left) Simulated micro-Doppler of a human picking up an object with randomness added in the form of swaying and (Right) STFT of the simulated micro-Doppler signal for a mm-wave radar.

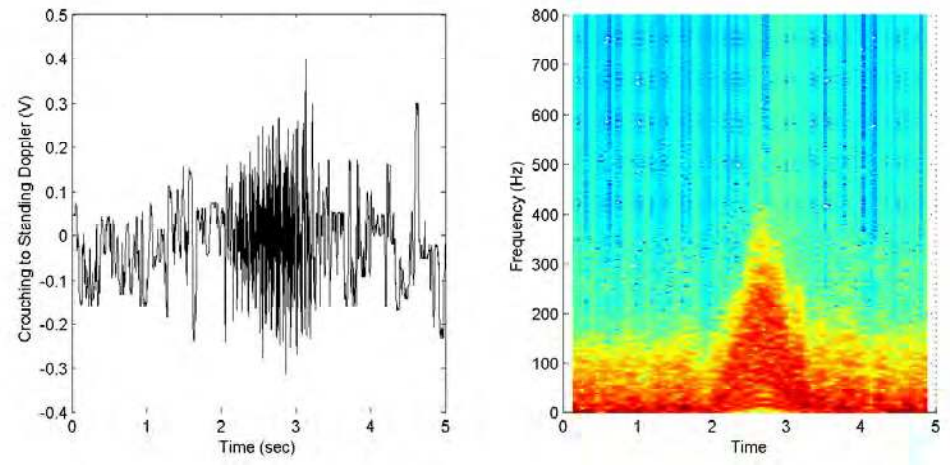

Figure 6.33: (Left) Simulated micro-Doppler of a human standing up from a crouching position with randomness added in the form of swaying and (Right) STFT of the simulated micro-Doppler signal for a mm-wave radar.

These figures show that the additional swaying movement is most prevalent in the low velocity areas of the STFT. In addition to this, the added randomness slightly distorts the higher frequency portions of the time-frequency plot as well and has a smearing effect. The STFT components from the 25 randomly located points on the torso components are less prevalent individually and the smearing

causes this to form a more complete micro-Doppler signature.

Randomness was also added to the human breathing simulations. In the experimental results of Figure 6.6, the test subject was seated in a chair to minimize other body movements and attempt to isolate the chest expansion due to respiration. Similar to the procedure described above for picking up an object and standing up from a crouching position, a small swaying motion was added to the breathing simulation. The swaying motion had an amplitude of 5 mm, a frequency of 4.5 Hz, was convolved with Gaussian random noise, and filtered to remove high frequency noise that produces non-smooth movements. The results are shown in Figure 6.34. The top left plot is the simulated micro-Doppler breathing signature with swaying and the bottom left plot is the STFT of the simulation. The top right plot is an experimentally measured breathing signature with a person who is standing and the bottom right plot is the STFT of the experimentally measured breathing signature. The experimental signatures display the effects of swaying. Comparison with the seated experimental breathing signature of Figure 6.6 clearly shows the differences between a subject that is standing and a subject that is seated. Because the swaying motion is very small in amplitude, this illustrates why it is so difficult to obtain the breathing signature from micro-Doppler data.

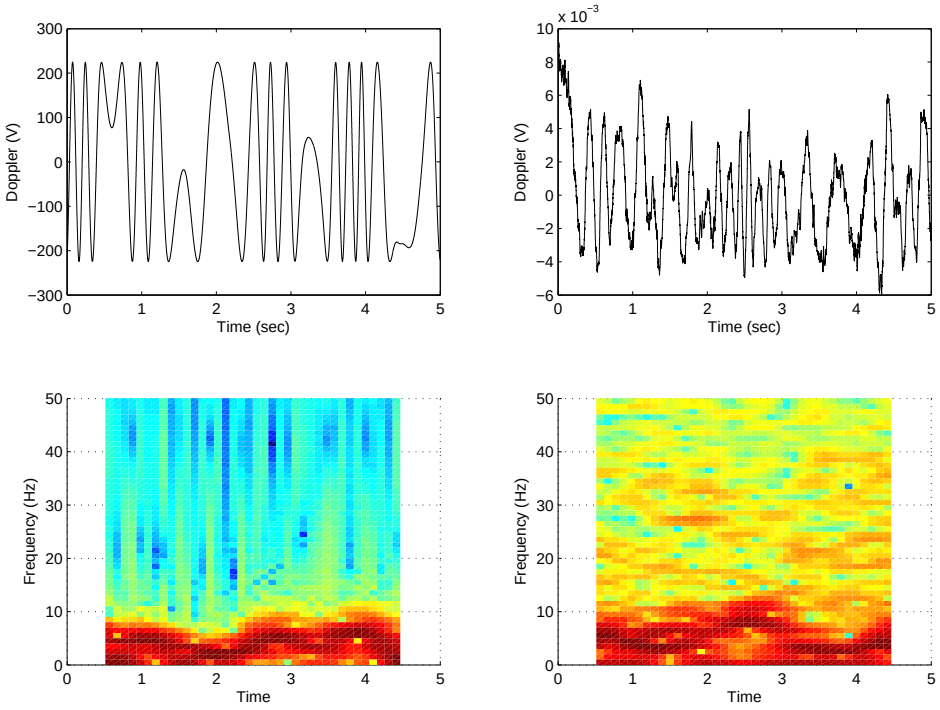

Figure 6.34: (Top Left) Simulated micro-Doppler signature of a human breathing after including swaying motions, (Bottom Left) STFT of the simulated breathing signature, (Top Right) experimentally measured breathing signature for a human subject who remained standing, and (Bottom Right) STFT of the experimentally measured breathing signature.

Chapter 7

Classification of Micro-Doppler Signatures

The ability to identify human motions using micro-Doppler signatures has become an area of interest recently. Activity classification has potential applications for surveillance, search and rescue operations, and patient monitoring in hospitals. Knowledge of human movements can aid in improving the safety of security or surveillance personnel or it can potentially locate a person trapped inside a building. The identification of movements can be useful; however, the larger goal may be to infer the intent of the target, which is a much more difficult problem. The classification of human movements can be performed by utilizing a Doppler radar system. The micro-Doppler frequency will vary depending on the unique velocity profile of a radar target over time. Specific movements will have unique micro-Doppler signatures which can then be classified [2].

7.1 Support Vector Machines

Support Vector Machines, developed by Vapnik in 1995 [63], have proven to be an effective alternative to traditional classification techniques such as Bayesian classifiers and Artificial Neural Networks. The primary advantages that SVMs have over the other methods are their ability to generalize and that they are relatively easy to implement. SVMs have also found use in regression problems.

Support Vector Machines were originally developed to address the binary clas-

sification problem. The classifier is optimized to produce a model that is based on the training set feature vectors and their associated known class label. Using this model, the test set can be accurately classified using only their feature vectors, without knowledge of the class label [63, 64, 65].

SVMs require the use of two known quantities. The first is the training vectors (feature vectors): $x_i \in \mathbb{R}^n, i = 1, \ldots, l$. The second is the label vector, $y \in \mathbb{R}^l$ such that $y_i \in$ [+1, -1]. The following primal optimization problem is formulated:

$$\max_{w,b,\xi} \frac{1}{2} w^T w + C \sum_{i=1}^{l} \xi_i \tag{7.1}$$

$$\text{subject to: } y_i(w^T \phi(x_i) + b) \geq 1 - \xi_i,$$

$$\xi_i \geq 0, i = 1, \ldots, l.$$

where w is the weight vector that defines a linear hyperplane separating the two classes of data, b is the constant offset of the hyperplane, ξ_i are a measure of the error of any misclassifications, and C is a penalty parameter that allows the classifier to tolerate some errors. The function ϕ maps the feature vectors into an N-dimensional space. The parameters x_i and y_i are the feature vectors and their associated class label (± 1) respectively. For the specific problem of classifying micro-Doppler signals that arise from human motion, the x_i are the energy feature vectors that were extracted using EMD.

The corresponding dual problem is simpler to solve and is:

$$\min_{\alpha} \frac{1}{2} \alpha^T Q \alpha - \mathbf{e}^T \alpha \tag{7.2}$$

$$\text{subject to: } y^T \alpha = 0,$$

$$0 \leq \alpha_i \leq C, i = 1, \ldots, l.$$

Here, $\mathbf{e}$ is a vector of ones and $Q_{ij} \equiv y_i y_j K(x_i, x_j) \in \mathbb{R}^{lxl}$. $K(x_i, x_j) \equiv \phi(x_i)^T \phi(x_j)$ is a kernel that maps the input feature vectors to a higher dimensional space. In many classification problems, the data are not linearly separable. In these cases, mapping to a higher dimensional space allows the data to be separated linearly in the higher dimensional space. This corresponds to a non-linear separation of

the classes in the original feature space [64]. By including the penalty parameter, C, the SVM will allow for some errors in the training set to avoid the problem of over-training (the solution of this problem is also referred to as a soft margin hyperplane). The dual problem above is a quadratic programming problem and can be solved using standard techniques. The vector, $\mathbf{w}$ in the primal problem is related to the vector α in the dual problem by:

$$\mathbf{w} \cdot \phi(x) = \sum_{i=1}^{l} y_i \alpha_i K(x_i, x). \tag{7.3}$$

Once the optimal α_i have been calculated, the decision function for C-SVM is:

$$y_p(x) = \text{sgn}(\sum_{i=1}^{l} y_i \alpha_i K(x_i, x) + b) = \text{sgn}(\mathbf{w} \cdot \phi(x) + b) \tag{7.4}$$

where a positive y_p indicates a predicted output belonging to the class: +1, and a negative y_p indicates a predicted output belonging to the class: -1. The bias parameter, b, is:

$$b = \frac{1}{N_{SV}} \sum_{i=1}^{N_{SV}} \mathbf{w} x_i - y_i. \tag{7.5}$$

where N_{SV} is the number of support vectors. The kernel, K, is a symmetric, positive definite function and there are many choices for this function. For most cases, the Gaussian kernel is preferred and it is the kernel of choice for the experiments discussed in the following sections.

Because the solution of the optimization problem is dependent on the parameters, (C, γ), it is necessary to find the set of these parameters that are also optimal. To find these optimal parameters, a grid-search will be performed, along with ν-fold cross-validation. Cross-validation allows the classifier to generalize well, so that the classifier will be accurate not only for data in the training set, but also for other unknown data. For our experiments, $\nu = 5$ is used.

Support Vector Machines were originally developed to solve the binary classification problem; therefore, modifications must be made in order to extend the binary problem to a multi-class problem. Multiple methods have been proposed to tackle this problem including the one-against-all method (1-a-a), the one-against-

one method (1-a-1), binary decision trees, and decision directed acyclic graphs (DDAG). Because of its intuitiveness and its ability to be easily adapted for additional classes, the 1-a-a method was chosen for our experiments.

Using the one-against-all method, for k-class classification ($y_i \in [1, \ldots, k]$), k binary classifiers are constructed. All of the data from the k^{th} class is represented with a label of '+1' and data corresponding to all of the other classes are represented with a label of '-1.' The decision function of each of the k classifiers is: $f_k(x) = \mathbf{w}_k \cdot \phi(x) + b_k$. This is the same decision function as for binary classification, except there are k of them and the sgn$(\cdot)$ function is omitted. In binary classification, the sign of $f(x)$ determines the class to which the data belongs. In the 1-a-a method of multi-class classification the output classification is the decision function which produced the largest value for $f_k(x)$ [66, 67]. This is because the magnitude of the decision function is the distance of a feature vector from the separating hyperplane. The larger the distance, the more likely it is that the feature vector is correctly classified.

$$y_p(x) = \arg\max_k f_k(x) \tag{7.6}$$

7.2 Classification Results

The feasibility of using EMD and a SVM classifier to identify human movements has been demonstrated through the use of a 750 MHz micro-Doppler radar [6, 68]. This radar was designed to detect human targets concealed behind a wall [69]. The radar operates through direct transmission of a 750 MHz CW wave. Empirical Mode Decomposition and classification are performed off line using Matlab. The classification is performed through the use of the LIBSVM software package[64, 70]. Using the 750 MHz radar, the classification algorithm was tested to ensure that the optimal parameters were obtained. To do this, the Receiver Operating Characteristic (ROC) is used. While the concept of an ROC is specific to the radar's probability of detection and probability of false alarm, this concept can be extended to classification. The ROC curve for the classification of six movements (same movements as described earlier, but with the sixth class: "miscellaneous movements" included) is shown in Figure 7.1. Here the probability of detection

(percentage of correct classifications) is shown on the vertical axis and the probability of false alarm (percentage of vectors that are classified as belonging to class i, but actually belong to another class) is shown on the horizontal axis. ROC curves are shown separately for the classification of each classifier used in 1-a-a multi-class classification. The curves were generated by varying the bias parameter, b, in the SVM decision function. Multiple curves were created for different values of γ that are described above. For the most accurate classifier, it is desired that a high probability of detection (p_d) is achieved, while minimizing the probability of false alarm (p_{fa}). An ROC curve that rises very steeply will achieve this. Figure 7.1 illustrates that, while the optimal (b, γ) may not yield the best (p_d, p_{fa}) for every class, the optimal parameters outperform other (b, γ) combinations overall.

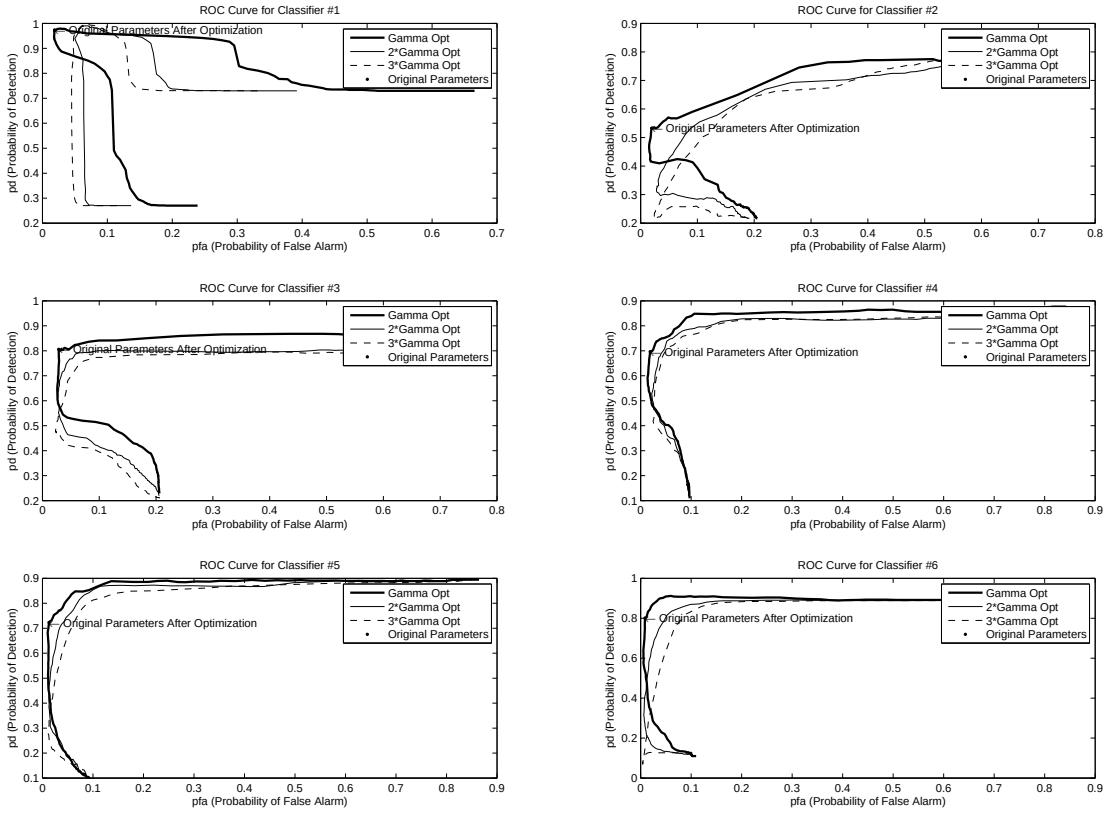

Figure 7.1: ROC curve for 6-Class classification (100 trials averaged).

In addition to calculating an ROC for the SVM, we also briefly investigated how to extend the binary SVM problem to multiple classes. As mentioned above, there are many choices for how to do this. Table 7.1 shows a comparison of the

results for the classification of 3 and 4 classes using the 1-a-a method and using a decision tree. As the table illustrates, both achieve nearly the same accuracy for this test. With this in mind and also realizing that the 1-a-a method was much simpler to implement than other methods, the 1-a-a method was selected for the remainder of our experiments.

Table 7.1: Comparison of the 1-a-a Method and Decision Tree Method of Multi-Class Classification

Average Accuracy of Training and Test Sets Combined (%)		
	3 Classes	**4 Classes**
1-a-a Method	95.84	96.69
Decision Tree Method	96.58	94.70

Our classification procedure has also been implemented for use with an S-band and mm-wave micro-Doppler radars [44, 45, 71]. The higher transmit frequencies allow these radars to pick out more subtle variations in the human movements because the Doppler frequency shift is directly proportional to the transmitted frequency. However, the larger carrier frequency also introduces higher losses for through-the-wall applications. The S-band radar is capable of detecting micro-motions through a 4-inch thick laboratory wall, a 4-inch thick brick wall, and an 8-inch thick cinder block wall and accurately classifies the motions of interest. The mm-wave radar is incapable of detecting through-wall signatures because of the high loss of the wall material, but it is capable of detecting micro-motions at distances of up to 300 feet or through light foliage.

The S-band radar is designed for close range, through-the-wall situations, whereas the mm-wave radar has been designed for longer range applications or applications where the target is concealed within light foliage. As we should expect, the mm-wave radar is not capable of detecting through-wall micro-Doppler signatures due to the extremely high losses that the wave will experience. Experiments have been conducted to test the accuracy of the micro-Doppler motion classification procedure. These experiments represent data taken for multiple different test subjects

with varying heights, weights, and fitness levels. For testing purposes, the data are rotated amongst these test subjects so that all except one of them are always used for training and cross-validation. The cross-validation and training sets consist of data from all but one of the test subjects, but the cross-validation and training sets contained no common data. The single remaining subject is used for the testing set. This will allow for an accurate assessment of how the classifier responds to data that are both "known" and "unknown."

The S-band micro-Doppler has been tested for four situations: (1) direct transmission (no wall), (2) through 4-inch thick laboratory wall, (3) through a 4-inch thick brick wall, and (4) through an 8-inch thick cinder block wall. For the first case, the person is located at approximately 11 feet from the radar antennas. For case two, the person is located approximately 3 feet behind the wall and the wall is located at approximately 8 feet from the radar antennas. For case three, the person is located approximately 5 feet behind the wall and the wall is located at approximately 6 feet from the radar antennas. For case four (cinder block wall), the attenuation was very great, so the distance must be shortened in order to receive a signal of adequate power. For that case, the person was located approximately 3 feet behind the wall and the wall was located at approximately 2 feet from the radar antennas. For cases (1), (3), and (4), the same 6 test subjects were used. For case (2), only 4 test subjects were used. These test subjects were the same as test subjects #'s 1, 2, 3, and 6 for the other 3 cases.

The classification procedure considers five different motions: 1) background noise, 2) breathing, 3) swinging arms, 4) picking up an object, and 5) transitioning from a crouching position to a standing position. The results are shown in Tables 7.2 - 7.5. The average accuracy when combining the results of all of the test subjects is 63.9%, 76.3, 49.8%, and 64.1% for no barrier, laboratory wall, brick wall, and cinder block wall respectively. The cinder block wall produced the lowest classification accuracy prior to shortening the distance to the target, which agrees with the expected results. The attenuation through cinder block is larger than through brick, so we would expect the classification accuracy to decrease accordingly. However, by shortening the distance for the cinder block case, we have shown that if the signal power is increased by an appropriate factor, classification through cinder block is feasible and the basic principles are no different than for

other materials. The accuracy of the laboratory wall is slightly higher than the others because those tests were conducted indoors, where wind, trees, etc. are not a factor. The other scenarios (no wall, brick, and cinder block walls) were conducted outdoors using a wall support frame that was constructed so that temporary wall structures could be built for testing the performance of through-wall radars.

Table 7.2: Classification results - S-band radar without wall barrier.

Test Subject	Set	Min (%)	Max (%)	Mean (%)	St. Dev
1	Cross-Val Set	58	80	70.4	7.9
	Test Set	70	80	76.0	3.3
2	Cross-Val Set	62	84	69.4	6.3
	Test Set	42	66	52.8	6.9
3	Cross-Val Set	60	82	69.0	7.9
	Test Set	56	68	61.0	3.8
4	Cross-Val Set	60	76	71.0	5.3
	Test Set	66	78	70.4	3.6
5	Cross-Val Set	60	86	72.4	7.0
	Test Set	60	72	66.8	3.6
6	Cross-Val Set	60	86	72.2	8.5
	Test Set	50	60	56.2	3.3

Table 7.3: Classification results - S-band radar through laboratory wall.

Test Subject	Set	Min (%)	Max (%)	Mean (%)	St. Dev
1	Cross-Val Set	80	96.7	87.3	6.2
	Test Set	72	92	85	5.4
2	Cross-Val Set	83.3	93.3	90.0	3.1
	Test Set	64	76	71.8	4.2
3	Cross-Val Set	86.7	96.7	92.3	3.2
	Test Set	66	82	74.4	5.0
4	Cross-Val Set	76.7	93.3	89.0	4.7
	Test Set	66	80	73.8	7.8

Table 7.4: Classification results - S-band radar through brick wall.

Test Subject	Set	Min (%)	Max (%)	Mean (%)	St. Dev
1	Cross-Val Set	48	66	59.4	6.1
	Test Set	54	68	61.4	5.1
2	Cross-Val Set	50	68	60.0	5.9
	Test Set	32	64	48.6	9.8
3	Cross-Val Set	54	72	61.8	6.4
	Test Set	38	54	44.2	4.3
4	Cross-Val Set	48	70	61.4	6.5
	Test Set	42	58	48.0	4.5
5	Cross-Val Set	56	68	61.4	3.4
	Test Set	38	56	46.6	5.0
6	Cross-Val Set	54	74	65.2	6.7
	Test Set	46	54	49.8	2.7

Table 7.5: Classification results - S-band radar through cinder block wall.

Test Subject	Set	Min (%)	Max (%)	Mean (%)	St. Dev
1	Cross-Val Set	60	78	71.0	4.6
	Test Set	48	64	57.2	5.0
2	Cross-Val Set	68	82	72.2	4.4
	Test Set	60	72	66	4.5
3	Cross-Val Set	58	78	68.6	7.0
	Test Set	64	78	68.4	5.3
4	Cross-Val Set	56	76	67.6	7.5
	Test Set	64	76	71.4	4.8
5	Cross-Val Set	68	82	73.0	4.0
	Test Set	50	66	59.6	5.8
6	Cross-Val Set	60	72	66.0	4.1
	Test Set	52	70	61.8	6.0

The mm-wave micro-Doppler radar has been tested for the situation of a person moving at a distances of 100, 200, and 300 feet in an outdoor environment. At a range of 300 feet, this radar is sensitive enough to be able to classify all of the motions of interest (the same five motions as in the S-band classifier). The training, cross-validation, and test sets were chosen in the same manner as was described for the S-band radar classification. Results are shown in Tables 7.6 - 7.8.

The average accuracy when combining the results of all six test subjects is 79.2%, 79.6%, and 94.3% for 100, 200, and 300 feet respectively. Because of the use of high gain antennas (approximately 40 dB), we were able to isolate the human target and eliminate much of the Doppler components that were caused by background motions such as swaying tree limbs. These results show that the classification algorithm is very accurate for micro-Doppler radars with a high transmit frequency. The reasoning behind the higher accuracy at 300 feet is because at the shorter distances, the human target will move outside of the antenna beam for portions of the motions of picking up an object and transitioning from crouching to standing. At the longer distances, the entire body is in the antenna beam, but the

illuminated area is still small enough to isolate the human target. When compared to the S-band radar results, we notice that the mm-wave radar performs much better and is more robust over different training scenarios. This does not detract from the S-band radar, but only serves to illustrate that higher Doppler frequency shifts are desirable for classification and also to illustrate that penetration through some materials may be a large obstacle to overcome for classification. In order to minimize the effects of the wall material, higher power or larger antenna gain is required.

Table 7.6: Classification Results - mm-Wave Radar at a Range of 100 feet.

Test Subject	Set	Min (%)	Max (%)	Mean (%)	St. Dev
1	Cross-Val Set	76	94	87.8	5.3
	Test Set	86	90	88.6	1.3
2	Cross-Val Set	86	98	91.4	4.3
	Test Set	84	90	87.0	1.9
3	Cross-Val Set	84	96	91.6	4.0
	Test Set	82	88	85.4	1.9
4	Cross-Val Set	82	92	89.0	3.7
	Test Set	78	86	80.6	3.1
5	Cross-Val Set	84	98	90.6	5.1
	Test Set	68	86	80.2	5.8
6	Cross-Val Set	82	100	90.4	4.8
	Test Set	40	72	53.4	9.3

Table 7.7: Classification Results - mm-Wave Radar at a Range of 200 feet.

Test Subject	Set	Min (%)	Max (%)	Mean (%)	St. Dev
1	Cross-Val Set	82	98	88	4.6
	Test Set	72	92	86.0	6.0
2	Cross-Val Set	84	94	88	4.0
	Test Set	80	84	80.4	1.3
3	Cross-Val Set	80	92	86	3.4
	Test Set	84	88	86.6	1.6
4	Cross-Val Set	74	92	87	5.4
	Test Set	78	90	84.4	4.6
5	Cross-Val Set	86	98	90.4	3.6
	Test Set	66	76	71.2	3.9
6	Cross-Val Set	84	94	90.2	3.6
	Test Set	56	80	69.2	7.1

Table 7.8: Classification Results - mm-Wave Radar at a Range of 300 feet.

Test Subject	Set	Min (%)	Max (%)	Mean (%)	St. Dev
1	Cross-Val Set	62	82	71.8	6.0
	Test Set	90	100	94.8	3.7
2	Cross-Val Set	60	82	70.0	6.1
	Test Set	90	98	95.2	3.2
3	Cross-Val Set	64	82	70.2	5.8
	Test Set	90	100	94.0	3.4
4	Cross-Val Set	62	80	72.2	5.5
	Test Set	92	98	95.2	1.9
5	Cross-Val Set	66	80	72.8	4.3
	Test Set	86	100	93.4	4.1
6	Cross-Val Set	58	78	67.4	6.4
	Test Set	84	98	93.4	5.0

A confusion matrix for the S-band classifier through a laboratory wall is shown in Table 7.9 and a confusion matrix for the mm-wave classifier at a distance of 300 feet is shown in Table 7.10. To remind the reader, the classes (or motions) that are classified are: (1) background, (2) swinging arms, (3) breathing, (4) picking up an object, and (5) transitioning from crouching to standing. This confusion matrix was obtained using data from all of the test subjects (4 for the S-band classifier and 6 for the mm-wave classifier) for training and cross-validation. The average cross-validation accuracy is shown in the confusion matrix where 20 trials have been averaged. Table 7.9 shows that all motions are classified well, with the lowest accuracy for classes 4 and 5. Table 7.10 shows that motions $1-4$ are classified well. The fifth motion is less accurate, but the confusion matrix indicates that it is approximately twice as likely to be classified correctly than it is to yield the output of the second most frequent result (picking up an object).

Table 7.9: Confusion Matrix for the Classification of S-Band micro-Doppler signals Through a Cinder Block Wall.

		Target Class				
		1	**2**	**3**	**4**	**5**
Output Class	**1**	100	0	3.2	0.6	5.4
	2	0	93.9	0	0	1.4
	3	0	0	87.3	15.5	0.7
	4	0	0	7.0	78.0	8.8
	5	0	6.1	2.5	6.0	83.8

Table 7.10: Confusion Matrix for the Classification of mm-wave micro-Doppler signals at a Distance of 91 m.

		Target Class				
		1	**2**	**3**	**4**	**5**
Output Class	**1**	74.1	19.9	3.4	0	8.3
	2	11.9	69.5	3.9	3.8	12.6
	3	8.2	1.6	84.1	4.6	12.6
	4	1.2	0	3.9	78.1	22.6
	5	4.5	9.0	4.7	13.4	43.9

The results using each radar system illustrate that different people perform motions in slightly different manners. This also means that classification is more accurate if the test subject performs the motions in a similar manner to other test subjects in the training set. For the best possible results, a large number of test subjects should be used for training so that as many variations in the movements can be accounted for as possible.

It may also be desired to simply determine if there is a moving human target or not. Based on the confusion matrices of Figures 7.9 and 7.10 we can see that high classification accuracy is achieved for background noise (class #1). The accuracies of the other 4 motions are also high, so the simple determination of the presence of moving targets can be performed by determining if the Doppler signal is classified as class 1 or classes $2-5$. Another approach to this problem is to construct a binary classifier, where all of the data from classes $2-5$ are combined into a single class.

Another observation that is made is that the results stated in other publications describe classifiers that use data from test subjects at very close ranges and in ideal conditions. Here, the classification accuracy is lower than some of these other experiments because we have implemented our algorithm for longer ranges and for through-wall environments. These reflect a more realistic environment and we still achieve a high degree of accuracy.

The classifier above utilizes EMD to produce feature vectors for classification and the target remains stationary when performing the motions. Other work has

been performed in this area, which concentrates on identifying human gait. One example is in [2], where the motions of running, walking, walking while holding a stick, crawling, boxing while moving forward, boxing while standing in place, and sitting still were considered for micro-Doppler classification. There, features were selected based off of STFT characteristics. The features that were selected for classification were: 1) torso Doppler frequency, 2) the total bandwidth of the Doppler signal, 3) the offset of the total Doppler, 4) the bandwidth without micro-Doppler, 5) the normalized standard deviation of the Doppler signal strength, and 6) the period of the limb motion. The data was classified using a Support Vector Machine. The classification of these motions were reported to have an accuracy as high as 92.8%

Another example of human activity classification can be found in [72]. The technique is different from the above techniques in that it transmits an ultra-wideband signal and uses principal component analysis as the feature extraction method. The overall classification accuracy for the classification of eight different human activities is 85.3%. The eight activities are: walking, running, rotating, punching, jumping, transitioning between standing and sitting, crawling, and standing still. Even though this technique does not utilize the micro-Doppler phenomenon, it is always of interest to investigate other methods.

7.3 Analysis of Classification Accuracy for Measurement Error

To investigate how robust the classifier is to other influences such as measurement error, slight changes in the EMD stopping criteria, and modest variations in how movements are performed, an error analysis is performed. Here, a classifier is trained in the same manner as described earlier. The test set features are then obtained and perturbed by small amounts to see how the classification accuracy is affected. For the first case, each feature within the test set is perturbed by a uniform random value ranging from $[-n\%, +n\%]$ of its original value. This means that the uniform distribution is not the same for each feature, but instead depends on the original magnitude of each individual feature. Classification is then

performed on the test set using the new feature vectors and the accuracy of the classifier is assessed. Figure 7.2 shows the classification results for various degrees of perturbation. The results shown are averaged over 100 trials. The classifier for Figure 7.2 uses mm-wave radar data for human targets moving at 100 feet. The test subject is test subject 1.

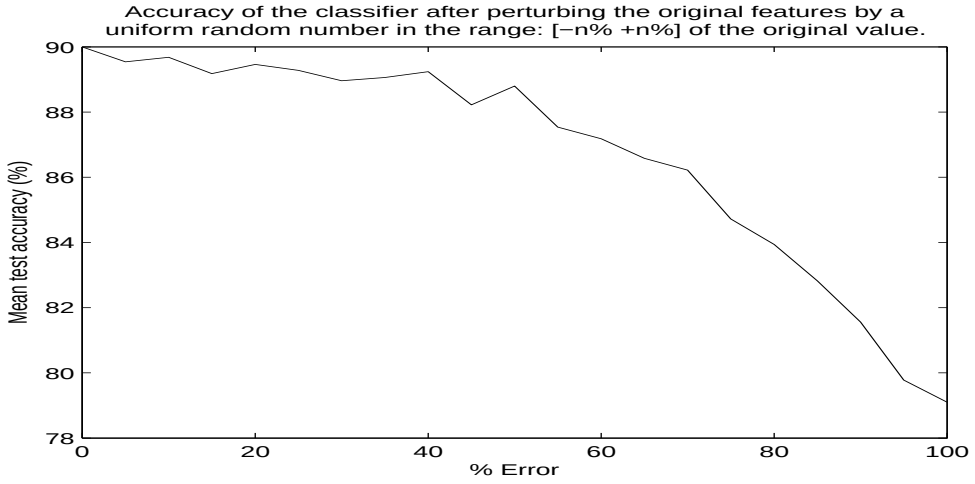

Figure 7.2: Classification accuracy after adding zero mean, uniformly distributed random noise to each feature with test subject 1 used for the data in the test set.

The same procedure has also been implemented using uniformly distributed random values in the range: $[0, +n\%]$ and $[-n\%, 0]$ and also for random values that are normally distributed with zero mean and a standard deviation of $n\%$ of the original feature value. These are shown in Figures 7.3, 7.4, and 7.5 respectively.

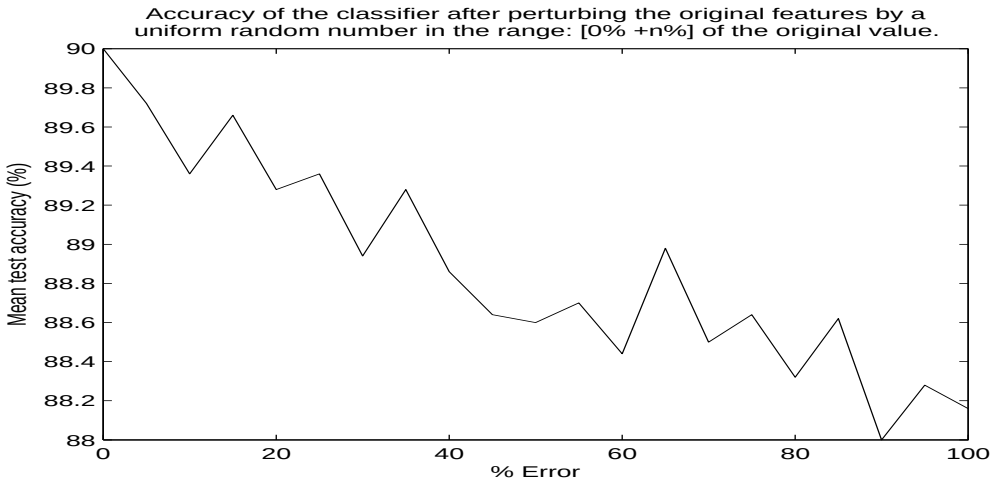

Figure 7.3: Classification accuracy after adding positive, uniformly distributed random noise to each feature with test subject 1 used for the data in the test set.

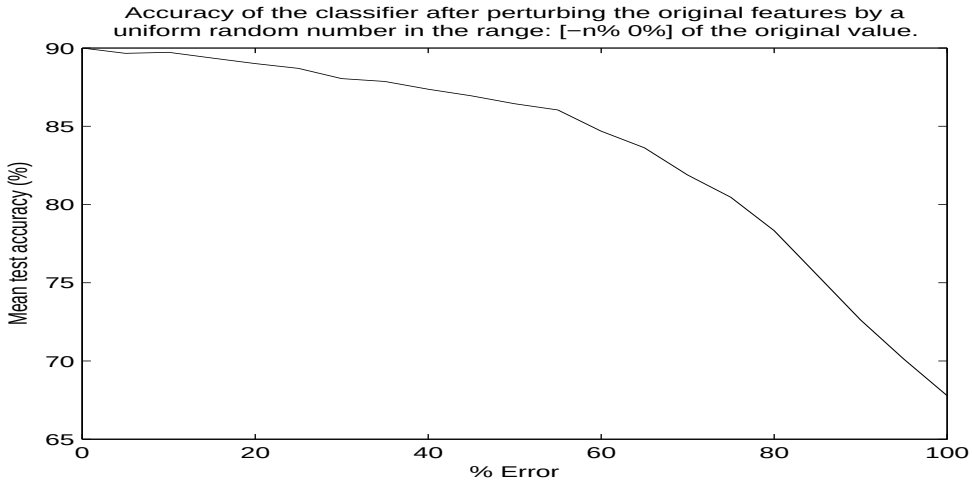

Figure 7.4: Classification accuracy after adding negative, uniformly distributed random noise to each feature with test subject 1 used for the data in the test set.

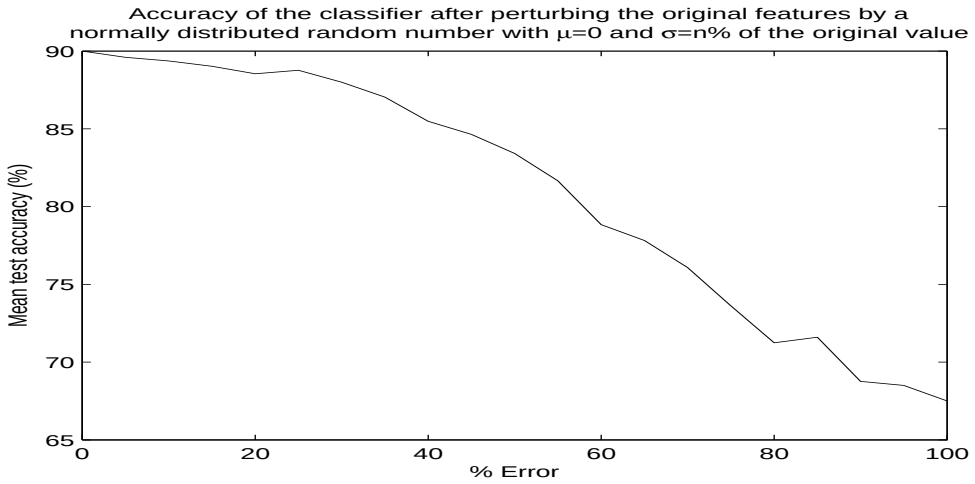

Figure 7.5: Classification accuracy after adding normally distributed random noise to each feature with test subject 1 used for the data in the test set.

This error analysis has been shown for test subject 1, however, it is important to view other test subjects as well. On average, for most of the test subjects, the classification accuracy follows similar patterns to those shown in Figures 7.2-7.5. However, some test subjects do not exhibit these trends for all cases. For example, if test subject 4 is used for the test set in the error analysis, the results are slightly different. The results using uniformly distributed random values in the range: $[-n\%, +n\%]$, $[0, +n\%]$, and $[-n\%, 0]$ and also for random values that are normally distributed with zero mean and a standard deviation of $n\%$ of the original feature value are shown in Figures 7.6, 7.7, 7.8, and 7.9 respectively.

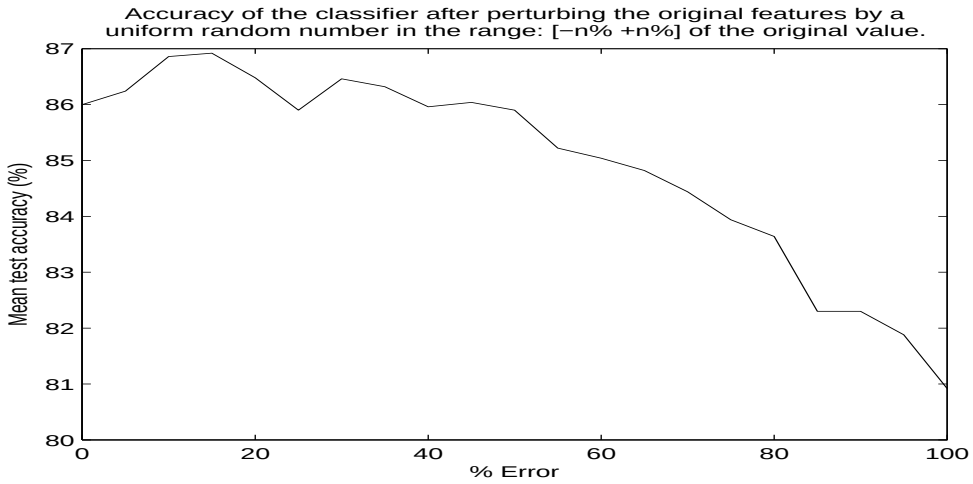

Figure 7.6: Classification accuracy after adding zero mean, uniformly distributed random noise to each feature with test subject 4 used for the data in the test set.

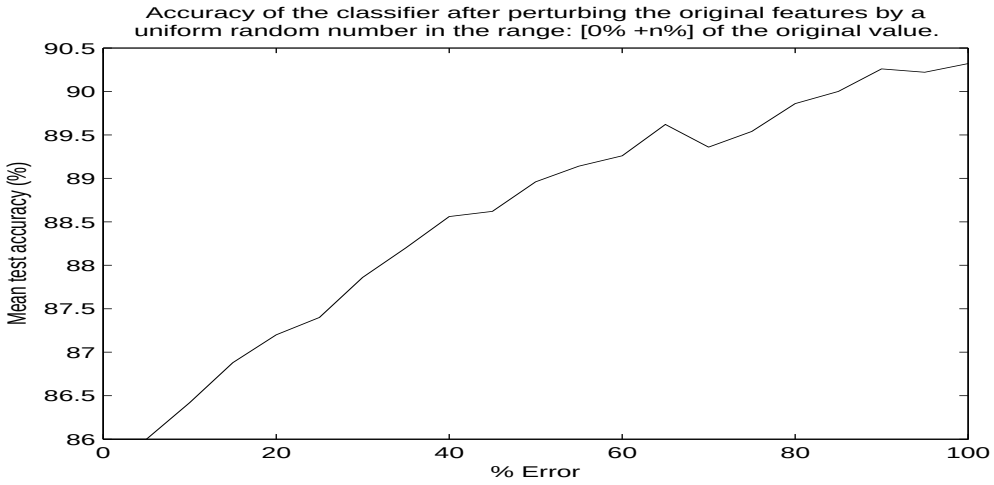

Figure 7.7: Classification accuracy after adding positive, uniformly distributed random noise to each feature with test subject 4 used for the data in the test set.

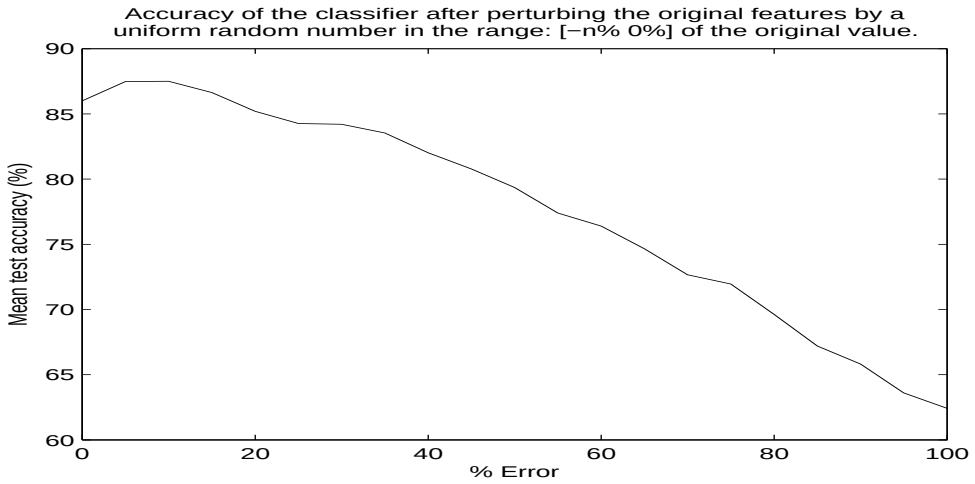

Figure 7.8: Classification accuracy after adding negative, uniformly distributed random noise to each feature with test subject 4 used for the data in the test set.

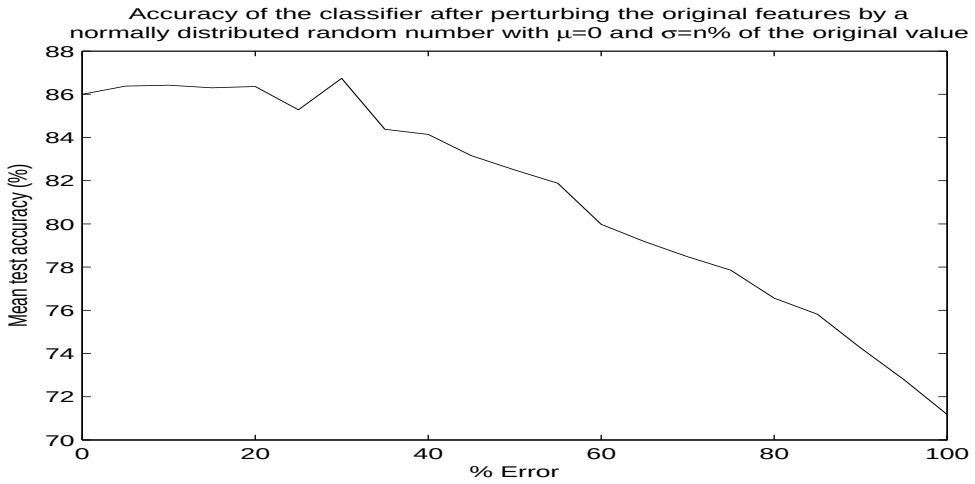

Figure 7.9: Classification accuracy after adding normally distributed random noise to each feature with test subject 4 used for the data in the test set.

For the cases of adding zero mean uniformly distributed error, negative uniformly distributed error, and zero mean normally distributed error, the results remain similar to those with test subject 1. The difference is in Figure 7.7. This figure illustrates that the classification accuracy using data from test subject 4 improves if positive error values are added to the features. Intuitively, this makes sense when we reflect on the differences in body types of test subjects 1 and 4. Test subject 1 has a large, athletic build, whereas test subject 4 is shorter and less mus-

cular. This means that test subject 4 has a smaller RCS than test subject 1 and the received Doppler signal from test subject 4 will be slightly weaker than that of test subject 1. This directly influences the energy of each IMF component (or components of the feature vector) that comes out of the EMD sifting process. Because all of this test subject's features have a lower value, we would expect that the feature vectors would be nearer to the boundaries between classes. Adding small values to the features moves those points away from the boundary and are more likely to be correctly classified. If the features are increased by large amounts, the classification accuracy follows the same pattern as shown by test subject 1 and this phenomenon is shown in Figure 7.10. This clearly shows the importance of using as many test subjects as possible and of using test subjects that exhibit different body types. If the classifier is trained using only test subjects that are similar in build, then the classifier will not work as well as one that used test subjects with diverse body types.

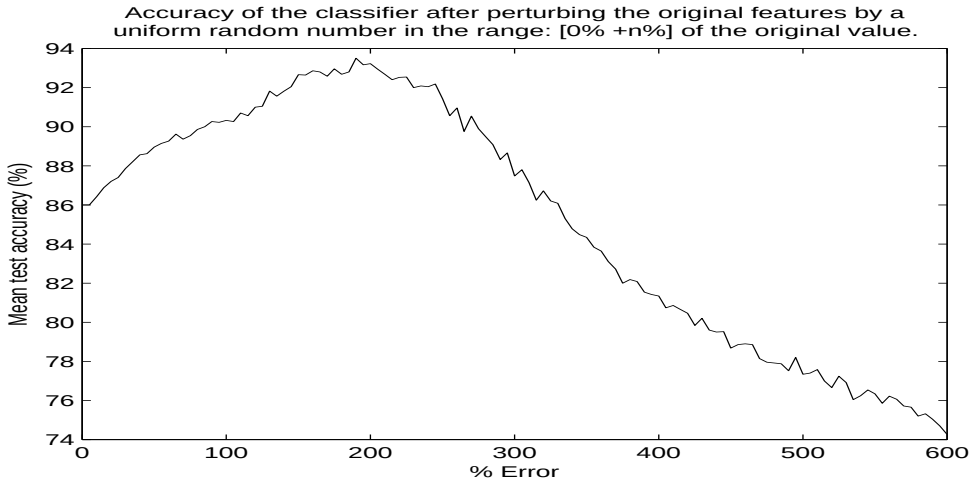

Figure 7.10: Classification accuracy after adding positive, uniformly distributed random noise to each feature with test subject 4 used for the data in the test set. The horizontal axis has been expanded beyond 100%.

The same analysis has been performed using data from the S-band radar. Here, the data that was chosen was for no wall barrier between the human target and the radar and the test set consists of data from test subject 1 once again. The results using uniformly distributed random values in the range: $[-n\%, +n\%]$, $[0, +n\%]$, and $[-n\%, 0]$ and also for random values that are normally distributed with zero

mean and a standard deviation of $n\%$ of the original feature value are shown in Figures 7.11, 7.12, 7.13, and 7.14 respectively.

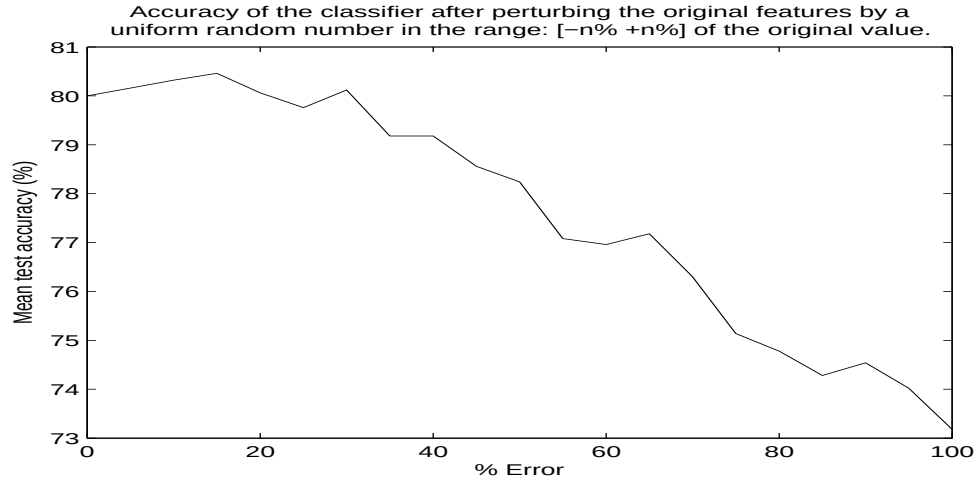

Figure 7.11: Classification accuracy after adding zero mean, uniformly distributed random noise to each feature with test subject 1 used for the data in the test set.

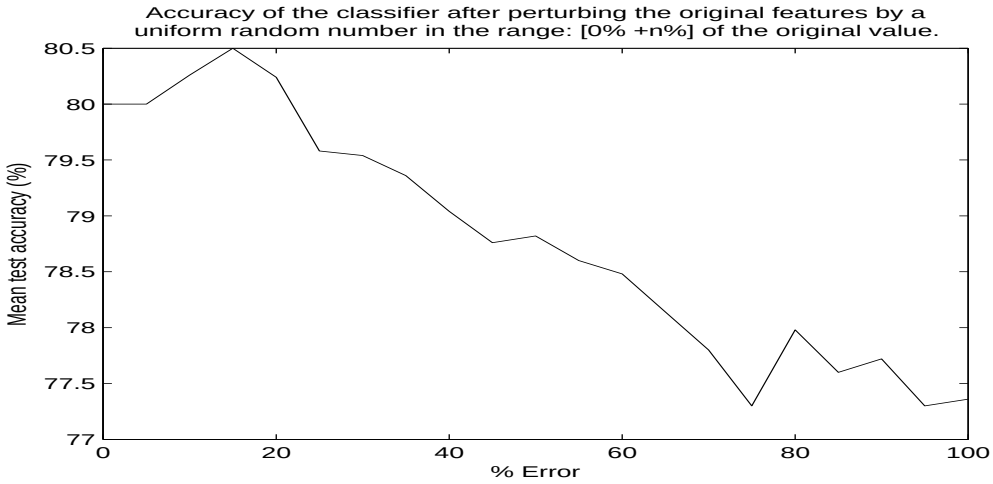

Figure 7.12: Classification accuracy after adding positive, uniformly distributed random noise to each feature with test subject 1 used for the data in the test set.

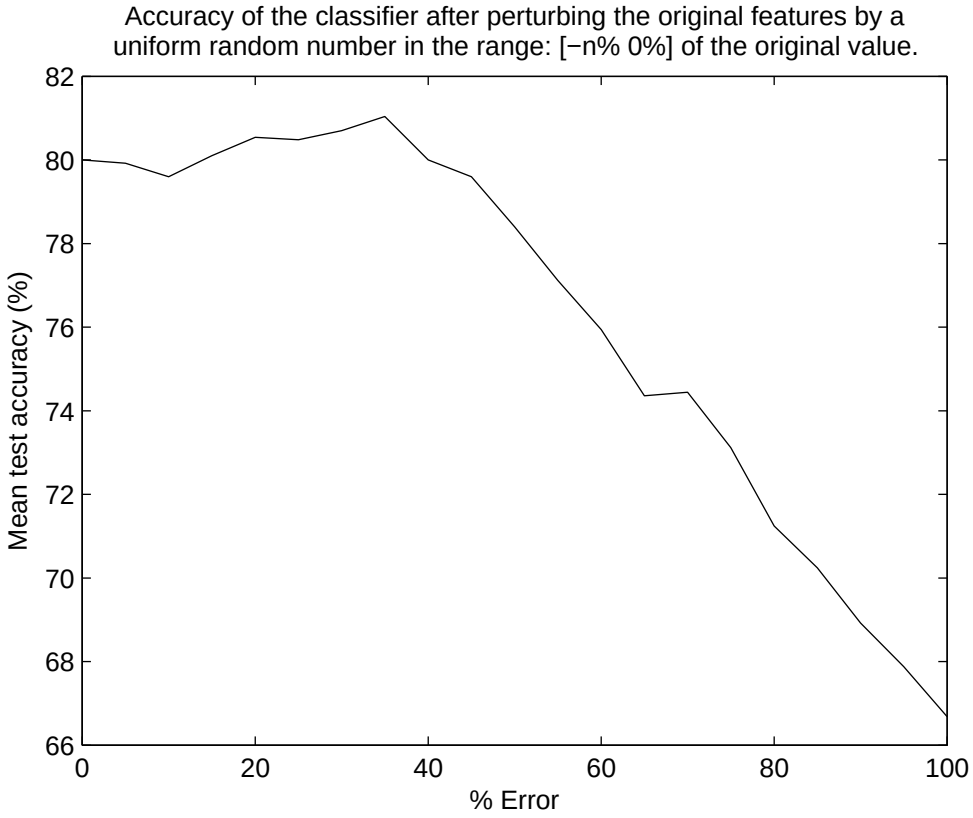

Figure 7.13: Classification accuracy after adding negative, uniformly distributed random noise to each feature with test subject 1 used for the data in the test set.

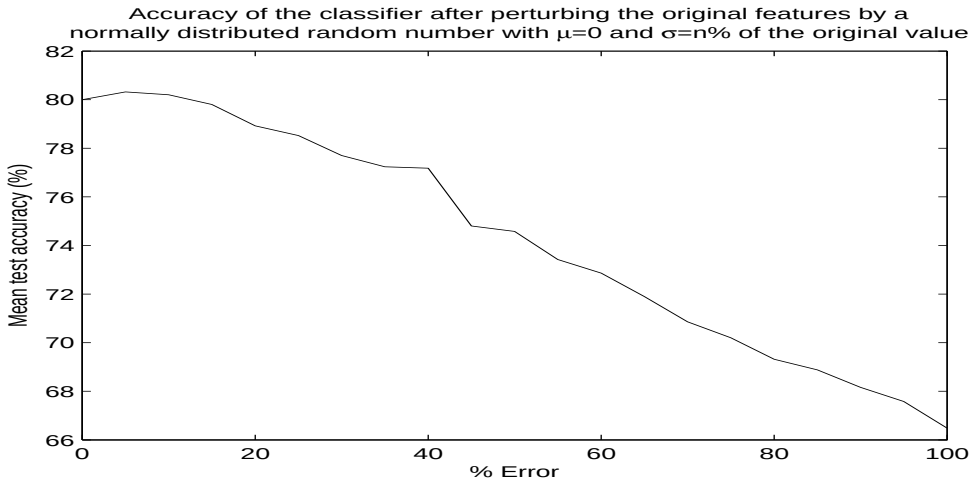

Figure 7.14: Classification accuracy after adding normally distributed random noise to each feature with test subject 1 used for the data in the test set.

Chapter 8

Effect of Stopping Criteria on EMD and SVM

The effect of the stopping criteria on the EMD and SVM results is important to consider. Figures 8.1 - 8.10 illustrate the effect that the EMD stopping criteria have. Here, a classifier is constructed from the data set that was used for generating the ROC curves in Section 7.2.

Setting the stopping criteria for EMD can be completed in two different ways. The first involves setting a maximum number of iterations for the inner loop of the EMD sifting process. The second involves setting limits for the mean envelope, $m(t)$. Ideally, the inner loop of the EMD algorithm stops when $m(t) = 0$ for all time. In practice, however, limits are set for $m(t)$. When setting limits for the mean envelope, a tolerance and two thresholds are defined. The tolerance determines the percentage of time samples that must be less than threshold #2. The remaining time samples must fall below threshold #1, which is the more restrictive of the two thresholds.

In general, when the stopping criteria are relaxed, the number of resulting IMFs from EMD is also less, which means that EMD will complete faster. Because the energy of each IMF is used as feature for classification, less IMFs will also mean that the feature vectors inhabit a lower dimensional feature space and will cause SVM training and classification time to be reduced accordingly. From Figures 8.4, 8.6, 8.8, and 8.10 it is easily seen that relaxing the stopping criteria a small amount will not have a noticeable effect on the classification accuracy. However, Figure 8.2

shows that if the number of points is reduced too much through decimation, some of the information in that signal is lost and the classification accuracy suffers.

As expected, relaxing the stopping criteria or reducing the number of samples through decimation will cause the SVM training time to decrease significantly. Once the classifier has been trained, the time to classify new data is always very small because the SVM optimization problem is only solved for training. Once the SVM parameters are determined, simple vector multiplication is all that is required to classify new data. For this reason, classification can essentially be performed in real time. The figures below illustrate that the stopping criteria does not have a noticeable effect on the testing time. The main time limitation for the total algorithm is that 5 seconds must be recorded to ensure that an entire motion is captured by the radar. Five seconds was chosen because adults typically have a respiration rate of $12 - 24$ breaths per minute ($0.2 - 0.4$ breaths per second) and 5 seconds will encompass one entire respiratory cycle for a typical adult.

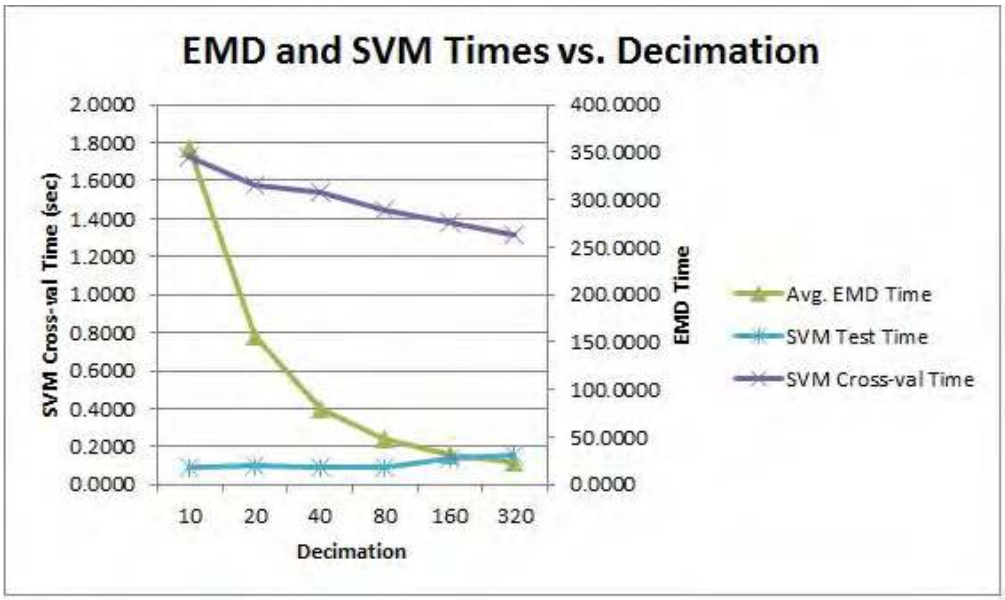

Figure 8.1: Decimation factor vs. EMD and SVM Completion Times.

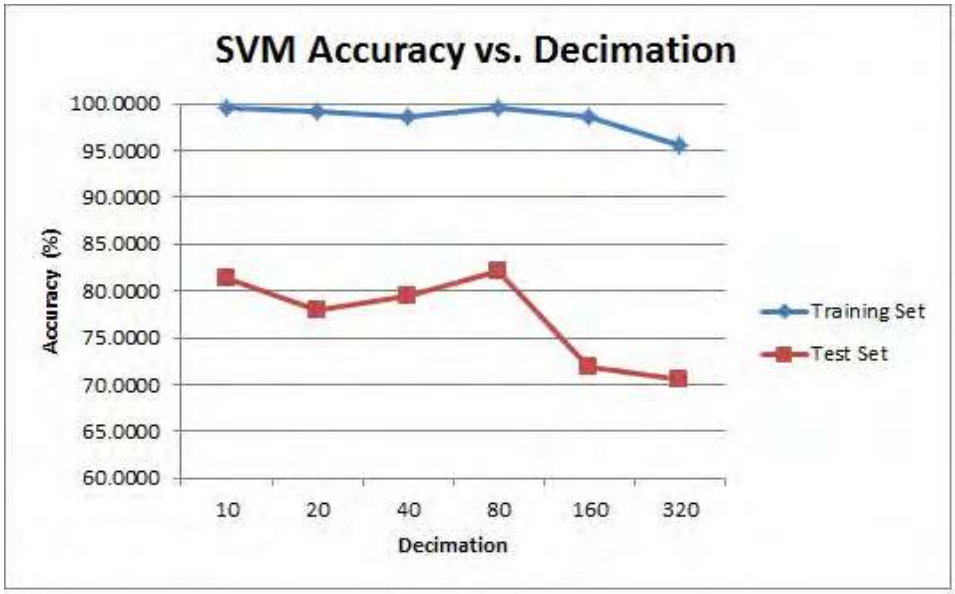

Figure 8.2: Decimation factor vs. SVM accuracy.

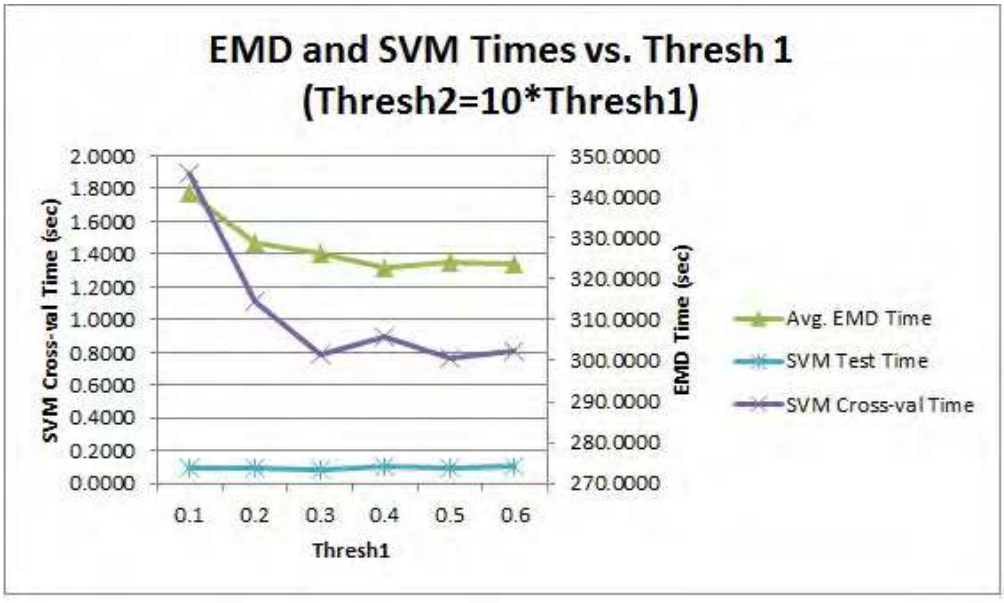

Figure 8.3: Threshold1 value vs. EMD and SVM Completion Times.

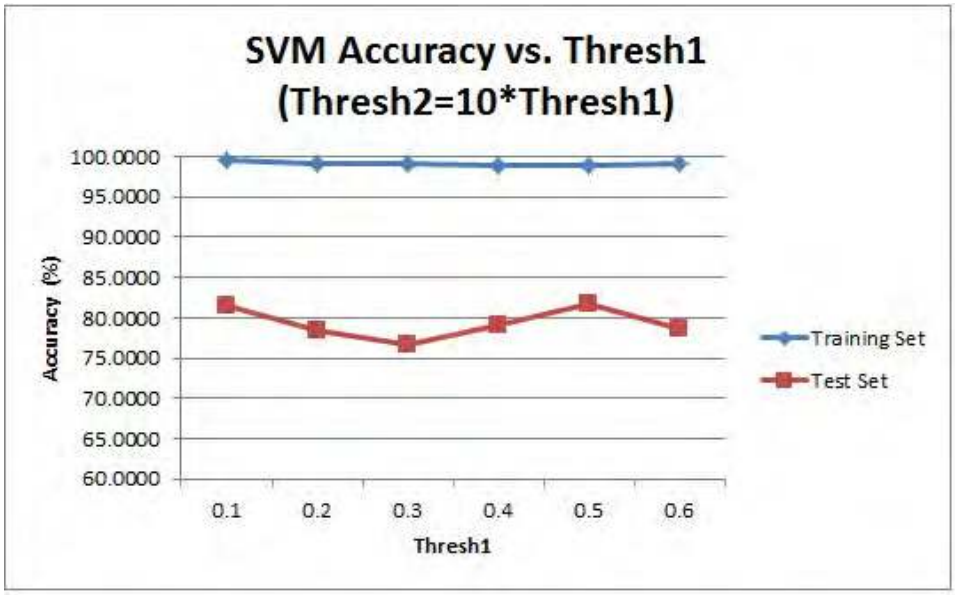

Figure 8.4: Threshold1 value vs. SVM accuracy.

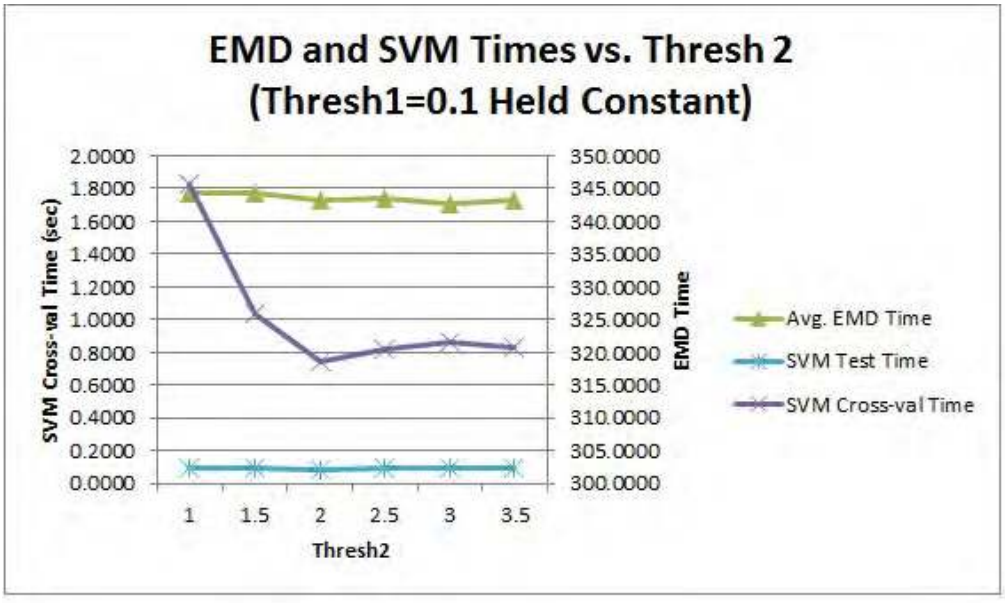

Figure 8.5: Threshold2 value vs. EMD and SVM Completion Times.

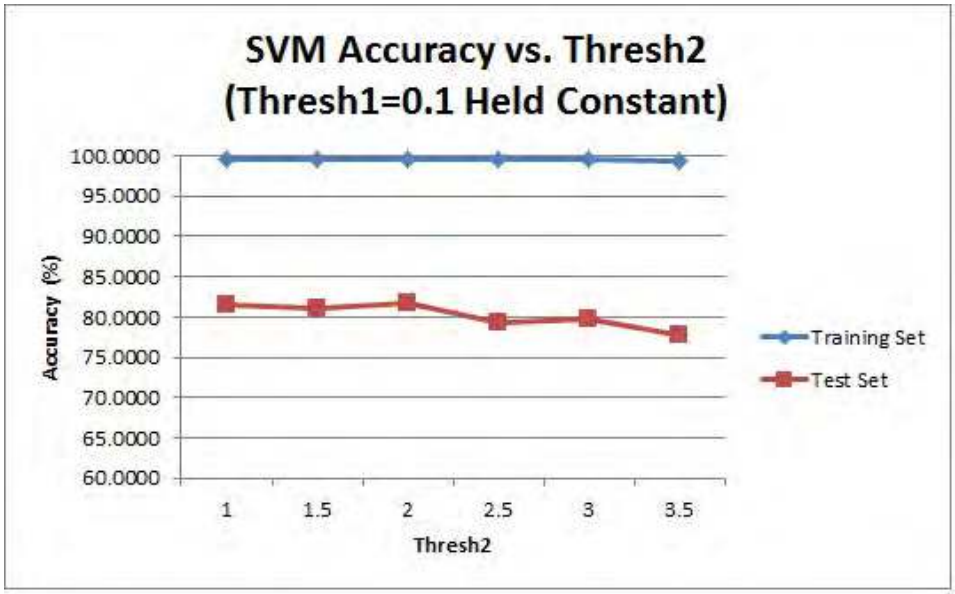

Figure 8.6: Threshold2 value vs. SVM accuracy.

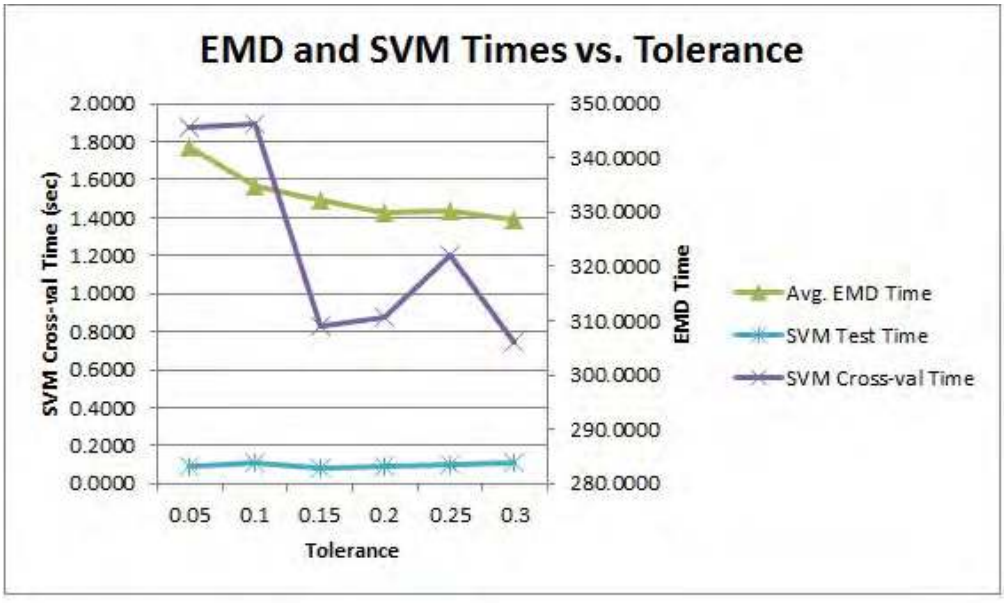

Figure 8.7: Tolerance factor vs. EMD and SVM Completion Times.

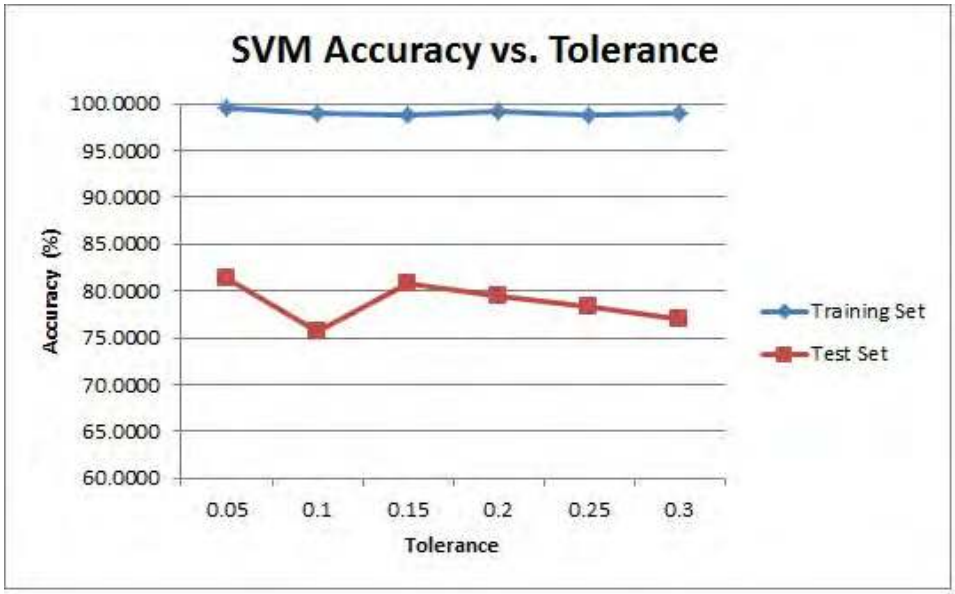

Figure 8.8: Tolerance factor vs. SVM accuracy.

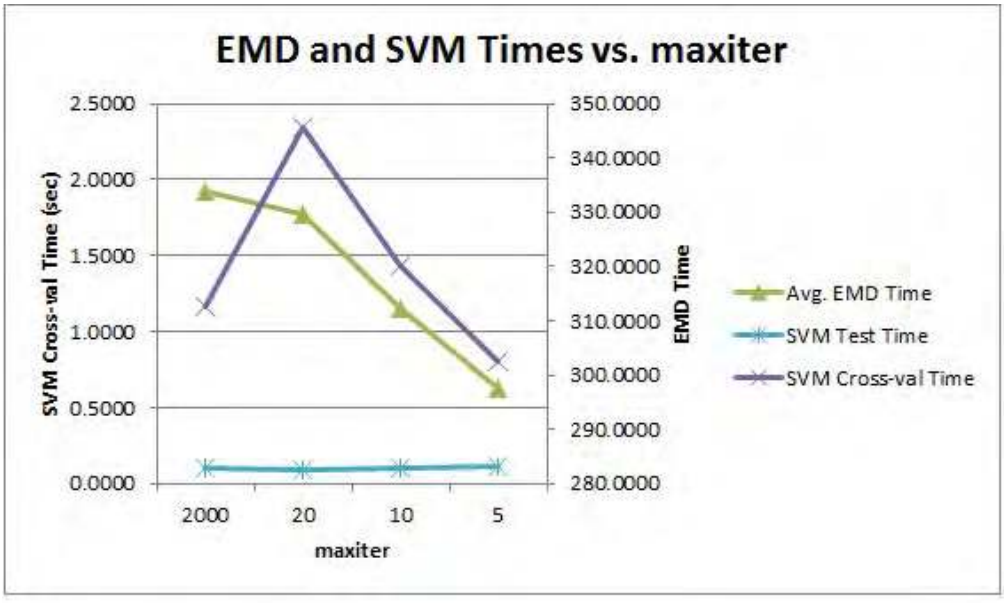

Figure 8.9: Maximum number of EMD inner loop iterations vs. EMD and SVM Completion Times.

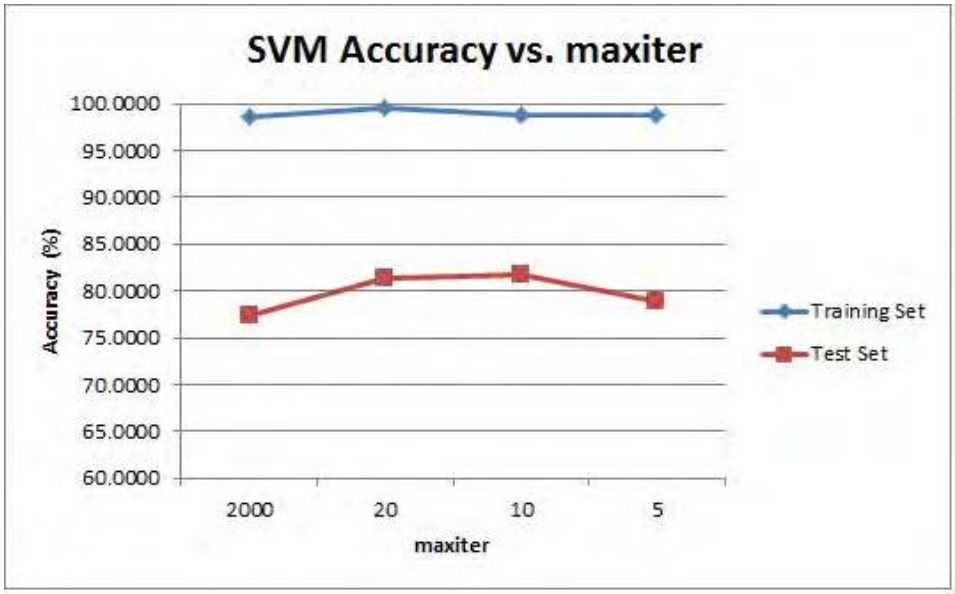

Figure 8.10: Maximum number of EMD inner loop iterations vs. SVM accuracy.

Chapter 9

MIMO Doppler for Detecting Target Orientation

Classification of human gestures using micro-Doppler signals has been demonstrated for a single sensor radar system. If multiple sensors are employed, additional information about the target can be inferred. Of interest is the direction a target is facing. Ranging is only capable of detecting the location of an object, but if multiple sensors are employed, a moving target's orientation can be determined.

The micro-Doppler effect for bistatic radar has been analyzed by multiple researchers. In [73], the micro-Doppler effect is studied for vibrating targets with a bistatic radar. In [74], the micro-Doppler effect is investigated for use in a single input, multiple output (SIMO) radar and [75] employs a bistatic radar system for use in synthetic aperture radar (SAR). In addition to this, if the transmitters and receivers are not distributed linearly, three-dimensional target information can be extracted using an algorithm described in [76], where the transmitters and receivers were located in a plane rather than a line. [77] has also demonstrated that multiple target angles will produce different time-frequency characteristics for each receiver and that these spectrograms can be fused to provide a complete picture of the target's time-frequency characteristics.

Here, many of these concepts will be built upon. Using knowledge of the bistatic micro-Doppler that is induced by target vibrations and utilizing multiple Doppler sensors, target orientation is determined. In addition to this, the classification algorithm that was proposed earlier in this dissertation will be employed with

SIMO micro-Doppler data. This radar contains a single transmitter (input) and two receivers (outputs). One receiver is collocated with the transmitter to create a quasi-monostatic Doppler sensor and the other receiver is separated from the transmitter to exploit additional advantages that can be achieved from a bistatic Doppler configuration.

9.1 MIMO Doppler Background

In the traditional monostatic Doppler equation, the Doppler frequency shift is:

$$f_d = \frac{2v(t)}{\lambda}\cos(\theta), \tag{9.1}$$

where $v(t)$ is the velocity of the target and θ is the angle of the target's velocity vector relative to the radar line of sight. If a single sensor Doppler radar is used, only the radial velocity of the target can be determined. It is clear from Equation 9.1 that if the target is moving at an angle of 90° from the radar line of sight, then a Doppler frequency shift cannot be measured.

In order to measure the orientation of a moving target, we have chosen to use two Doppler sensors, operating in a bistatic configuration. The bistatic Doppler equation is given by [11] and is:

$$f_d = \frac{2v(t)}{\lambda}\cos\left(\varphi/2\right)\cos\delta. \tag{9.2}$$

This expression differs from the traditional monostatic Doppler equation in two ways. First, the Doppler frequency shift is dependent on half the angle between the transmit and receive antennas (φ). Second, the angle θ in Equation 9.1 is replaced with the angle δ. Here, δ is the angle of the target's velocity vector relative to the bisector of the angle between the transmit and receive antennas. An illustration of this geometry is shown in Figure 9.1.

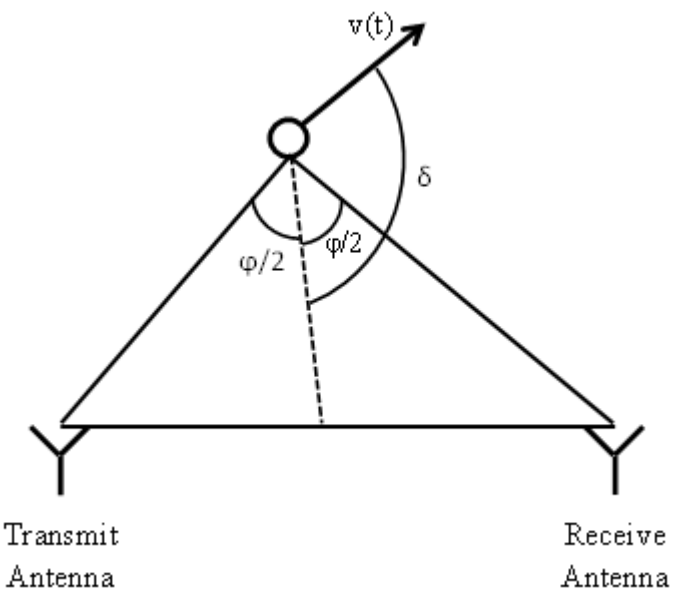

Figure 9.1: Diagram of a bistatic Doppler radar.

9.2 Theoretical Results

Changing to a bistatic configuration alone will still not allow for the target's orientation to be measured. In order to do this, multiple sensors must be used. This can be done in many ways, however, for demonstrative purposes, one transmit antenna and two receive antennas were used with one on each side of the transmit antenna. A diagram of this is shown in Figure 9.2.

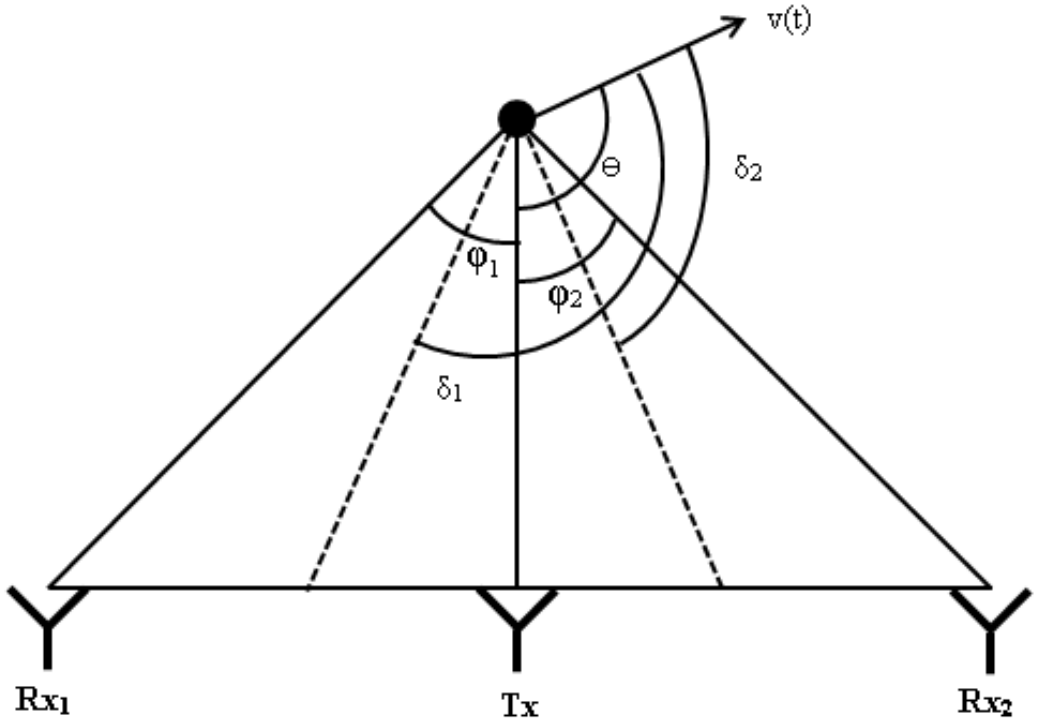

Figure 9.2: Diagram of the multiple radar sensor configuration.

With two receive antennas, subscripts are used to distinguish the Doppler expressions for each receiver. The equations corresponding to the receive antenna to the left of the transmit antenna are given the subscript 1 and the equations corresponding to the receive antenna to the right of the transmit antenna are given the subscript 2. The angle that the target is moving is measured relative to the transmit antenna and is denoted by θ.

The Doppler frequency shifts measured by each sensor are:

$$f_{d1} = \frac{2v(t)}{\lambda} \cos\left(\varphi_1/2\right) \cos\delta_1 \tag{9.3}$$

$$f_{d2} = \frac{2v(t)}{\lambda} \cos\left(\varphi_2/2\right) \cos\delta_2 \tag{9.4}$$

where $\delta_1 = \theta + \varphi_1/2$ and $\delta_2 = \theta - \varphi_2/2$. The ratio of Equation 9.4 to Equation 9.3 then yields:

$$\frac{f_{d2}}{f_{d1}} = \frac{\cos(\varphi_2/2)\cos\delta_2}{\cos(\varphi_1/2)\cos\delta_1}. \tag{9.5}$$

Because φ_1 and φ_2 are known from the initial setup, we can simplify the above expression by denoting $C = \frac{cos\varphi_2}{\cos\varphi_1}$. For ideal measurements and for motions that are smooth, Equation 9.5 will be a constant value. However, due to human movements being somewhat random, taking the ratio of the maximum of f_{d2} to the maximum of f_{d1} was found to produce more reliable measurements in practice. This means that Equation 9.5 becomes:

$$\frac{f_{d2}}{f_{d1}} = C\frac{\cos\delta_2}{\cos\delta_1} = k_1. \tag{9.6}$$

The remaining steps to determine an expression for δ_2 are as follows.

$$\delta_1 = \delta_2 + \frac{\varphi_1}{2} + \frac{\varphi_2}{2} \tag{9.7}$$

$$\cos\delta_2 = \frac{k_1}{C}\cos\delta_1 = \frac{k_1}{C}\cos\left(\delta_2 + \frac{1}{2}(\varphi_1+\varphi_2)\right) \tag{9.8}$$

Using the angle sum identity:

$$\cos(\delta_2 + \frac{1}{2}(\varphi_1+\varphi_2)) = \cos\delta_2\cos\left(\frac{1}{2}(\varphi_1+\varphi_2)\right) - \sin\delta_2\sin\left(\frac{1}{2}(\varphi_1+\varphi_2\right) \tag{9.9}$$

Let $\frac{1}{2}(\varphi_1+\varphi_2) = \psi$.

$$\cos\delta_2\Big[1 - \frac{k_1}{C}\cos\psi\Big] = -\frac{k_1}{C}\sin\delta_2\sin\psi \tag{9.10}$$

$$\tan\delta_2 = \frac{1-\frac{k_1}{C}\cos\psi}{-\frac{k_1}{C}\sin\psi} = \cot\psi - \frac{C}{k_1\sin\psi} \tag{9.11}$$

The angle that the target is moving is measured from the bisector of of the angle formed between the two receive antennas ($\frac{1}{2}(\varphi_1+\varphi_2)$) and is denoted by θ. This means that the angle that the target is moving relative to the transmit antenna is: $\theta_T = \theta - \delta_2 - \varphi_2/2$. Using this relationship and Equation 9.11, the angle

in which the target is moving relative to the transmit antenna can be determined. However, at angles beyond where f_{d1} is zero ($\delta_1 = 90°$ or $\theta = 90° - \varphi_1/2$), the results are inaccurate due to symmetry of k_1. This is illustrated in Figure 9.3. For this simulation, $\varphi_1 = 30°$, $\varphi_2 = 60°$, the transmitted frequency is 4 GHz, and the target is oscillating with a velocity that is sinusoidal in time.

In the left plot of Figure 9.3, there are two linear regions. These regions are where k_1 can be accurately used to calculate the angle of the target motion. In the linear region around $120° - 180°$, the measured angle is negative. This is because an oscillating target is used and adding $180°$ does not affect the results. Within the region of $75° - 120°$, the theoretical measured results are inaccurate. This is because of the repeating nature of using trigonometric functions to determine the angles.

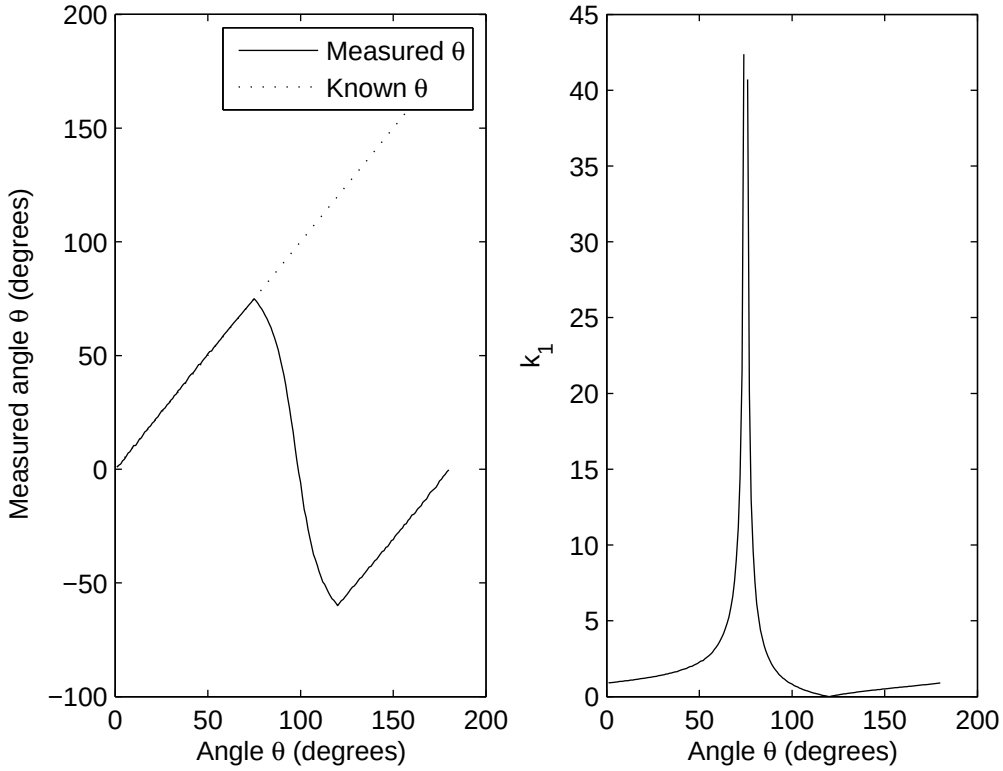

Figure 9.3: (Left) Measured angle θ using $k_1 = \frac{\max(f_{d2})}{\max(f_{d1})}$ and (Right) k_1 for a simple oscillating target.

In order to obtain accurate results for all angles, a second metric was used to

calculate the angle. The ratio of: $k_2 = (f_{d2} - f_{d1})/(f_{d1} + f_{d2})$ was used.
Using this value for k_2, the same steps as above can be taken to find an expression for δ_2. The steps are as follows:

$$f_{d2} + f_{d1} = \frac{2v(t)}{\lambda}[\cos(\varphi_2/2)\cos\delta_2 + \cos(\varphi_1/2)\cos\delta_1] \tag{9.12}$$

$$f_{d2} - f_{d1} = \frac{2v(t)}{\lambda}[\cos(\varphi_2/2)\cos\delta_2 - \cos(\varphi_1/2)\cos\delta_1] \tag{9.13}$$

$$k_2 = \frac{f_{d2} - f_{d1}}{f_{d1} + f_{d2}} = \frac{\cos(\varphi_2/2)\cos\delta_2 - \cos(\varphi_1/2)\cos\delta_1}{\cos(\varphi_2/2)\cos\delta_2 + \cos(\varphi_1/2)\cos\delta_1} \tag{9.14}$$

Letting $C = \frac{\cos(\varphi_2/2)}{\cos(\varphi_1/2)}$ as we did earlier results in:

$$k_2 = \frac{C\cos\delta_2 - \cos\delta_1}{C\cos\delta_2 + \cos\delta_1} \tag{9.15}$$

$$Ck_2\cos\delta_2 + k_2\cos\delta_1 = C\cos\delta_2 - \cos\delta_1 \tag{9.16}$$

$$Ck_2\cos\delta_2 + k_2\cos(\delta_2 + \psi) = C\cos\delta_2 - \cos(\delta_2 + \psi) \tag{9.17}$$

$$\cos\delta_2[Ck_2 - C] = -\cos(\delta_2 + \psi)[1 + k_2] \tag{9.18}$$

$$\cos\delta_2[Ck_2 - C] = -[1 + k_2][\cos\delta_2\cos\psi - \sin\delta_1\sin\psi] \tag{9.19}$$

$$-\frac{Ck_2 - C}{k_2 + 1} = \cos\psi - \tan\delta_2\sin\psi \tag{9.20}$$

$$\tan\delta_2 = \cot\psi + \frac{k_2 - 1}{k_2 + 1}\frac{C}{\sin\psi} \tag{9.21}$$

As was the case earlier, because human micro-Doppler motions are not ideal, the value of k_2 is altered to be:

$$k_2 = \frac{\max(f_{d2}) - \max(f_{d1})}{\max(f_{d1}) + \max(f_{d2})} \tag{9.22}$$

This produces much more reliable results in practice because the ratio was not always constant value when using real data. (Close inspection of the ratios show that the value of k_1 and k_2 are a function of time, but the time dependence arising from $v(t)$ cancels in the equations.) Because k_2 has been altered, Equation 9.21 must also be altered slightly. Because the sign information is removed by using the maxima of f_d in Equation 9.22, a sign change must be made in Equation 9.21.

This expression then becomes:

$$\tan\delta_2 = \cot\psi - \frac{k_2 - 1}{k_2 + 1}\frac{C}{\sin\psi} \tag{9.23}$$

The results of calculating the angle based on k_2 are shown in Figure 9.4. For this simulation, $\varphi_1 = 30°$, $\varphi_2 = 60°$, the transmitted frequency is 4 GHz, and the target is oscillating with a velocity that is sinusoidal in time. This figure shows that the angle is accurately measured for $75° - 120°$.

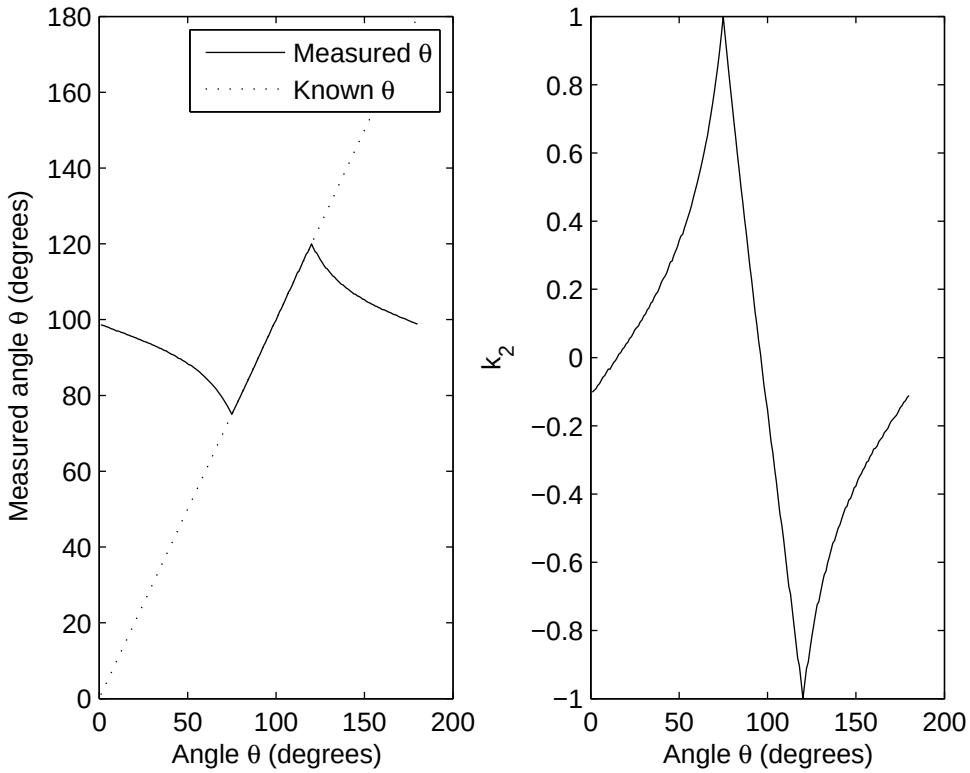

Figure 9.4: (Left) Measured angle θ using $k_2 = \frac{\max(f_{d2}) - \max(f_{d1})}{\max(f_{d1}) + \max(f_{d2})}$ and (Right) k_2 for a simple oscillating target.

By selecting the appropriate k value to use, the correct target oscillation angle can be calculated for any angle (because the target is oscillating back and forth, the angles $180° - 360°$ are equivalent to targets oscillating at angles of $0° - 180°$).

The criteria for selecting the correct k value to use is the phase difference between the time-frequency plots at each receive antenna. The phase angle can be

either 0° or 180°. If the target is moving either forward or backward relative to both of the receive antennas, the phase difference will be 0°, whereas if the target is moving toward one receiver and away from the other, the phase difference will be 180°.

After selecting the appropriate k value to use for calculations, the measured angle results are shown in Figure 9.5. As mentioned earlier, 180° can be added or subtracted to any results without changing the results, so the angles from 180° − 360° in Figure 9.5 are accurate even though they do not follow the dashed line.

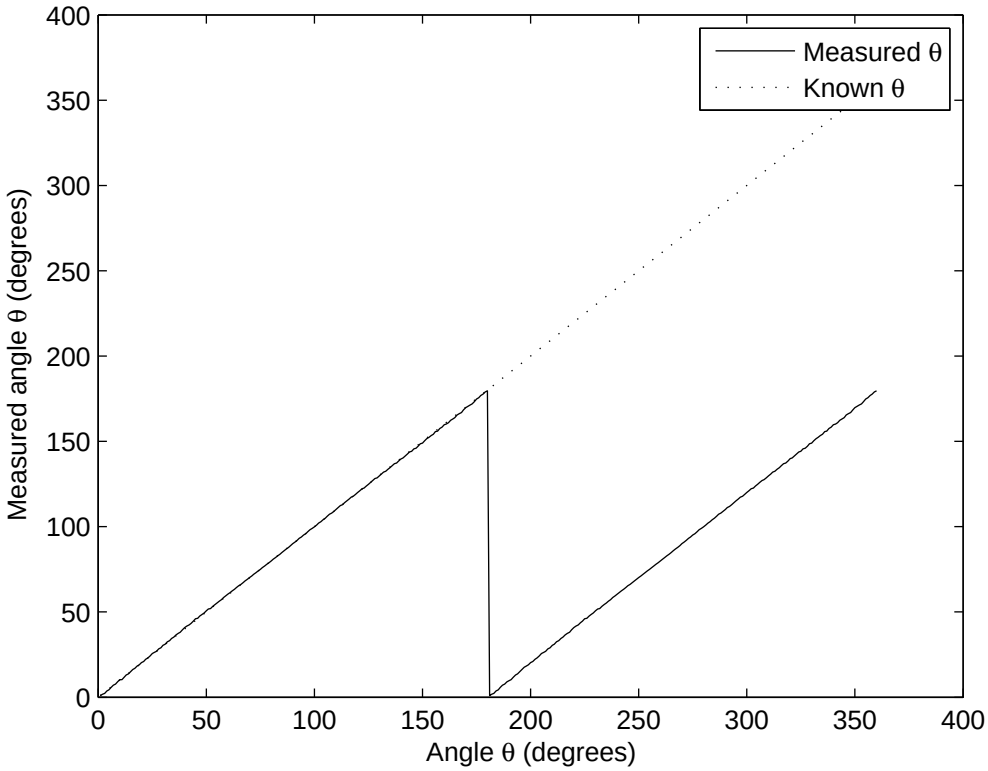

Figure 9.5: Measured angle θ based on a simulated oscillating target.

In addition to this, some small variations are observed in the measured angle. This is due to the frequency resolution of the STFT. The frequency resolution was chosen to be small so that an ideal simulation can be shown. If the frequency resolution is poorer, the results will be less accurate and are shown in Figure 9.6. In this figure, the sampling frequency was increased, but the maximum velocity

of the simulated Doppler target was kept constant. This illustrates that the sampling frequency for experimental data must be kept as close as possible to the Nyquist rate determined by the maximum Doppler frequency. In most cases this is subjective because the maximum velocity of a target cannot always be known beforehand, but an understanding of typical target speeds can be used to achieve the best results possible.

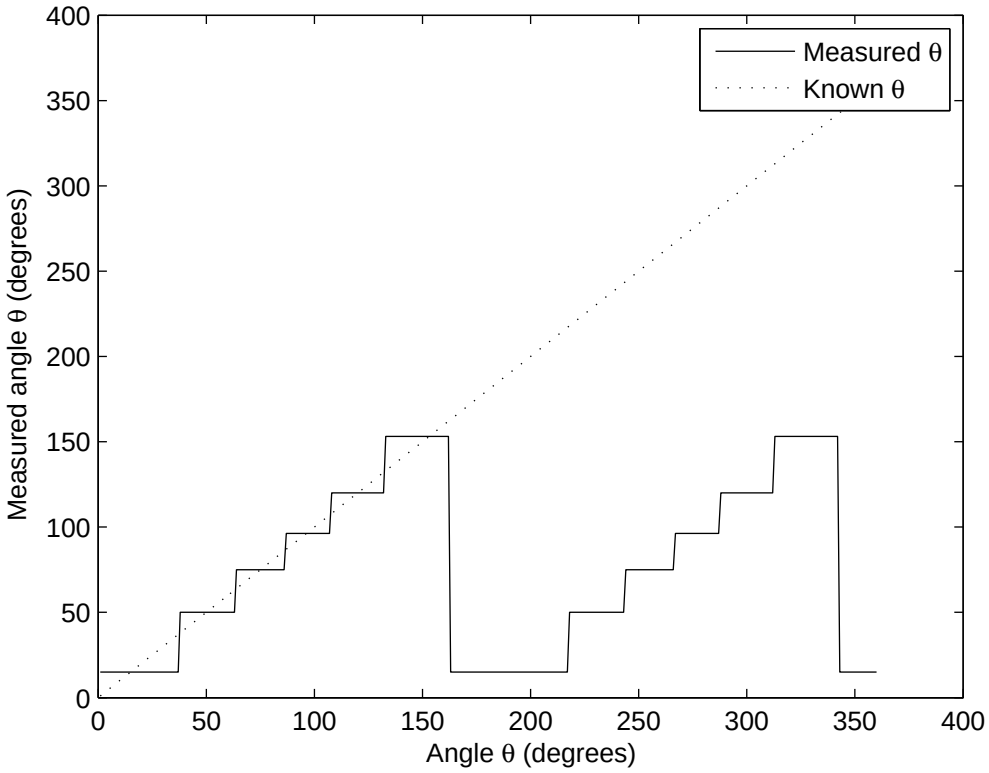

Figure 9.6: Measured angle θ based on a simulated oscillating target with poor STFT frequency resolution.

In the above simulations, the angles φ_1 and φ_2 are not required to be equal. However, if they are chosen to be equal, the equations are simplified slightly because $C = \frac{\cos\varphi_2}{\cos\varphi_1} = 1$.

9.3 Experimental Results

This procedure has been tested for a pendulum swinging. For the experiments that follow, the transmit antenna was located between two receive antennas with $\varphi = \varphi_1 = \varphi_2 = 45°$. A coherent Doppler radar was constructed with a transmit frequency of 4 GHz. A simple block diagram of the radar is shown in Figure 9.7. Filters are also included in the radar but are not shown in this figure.

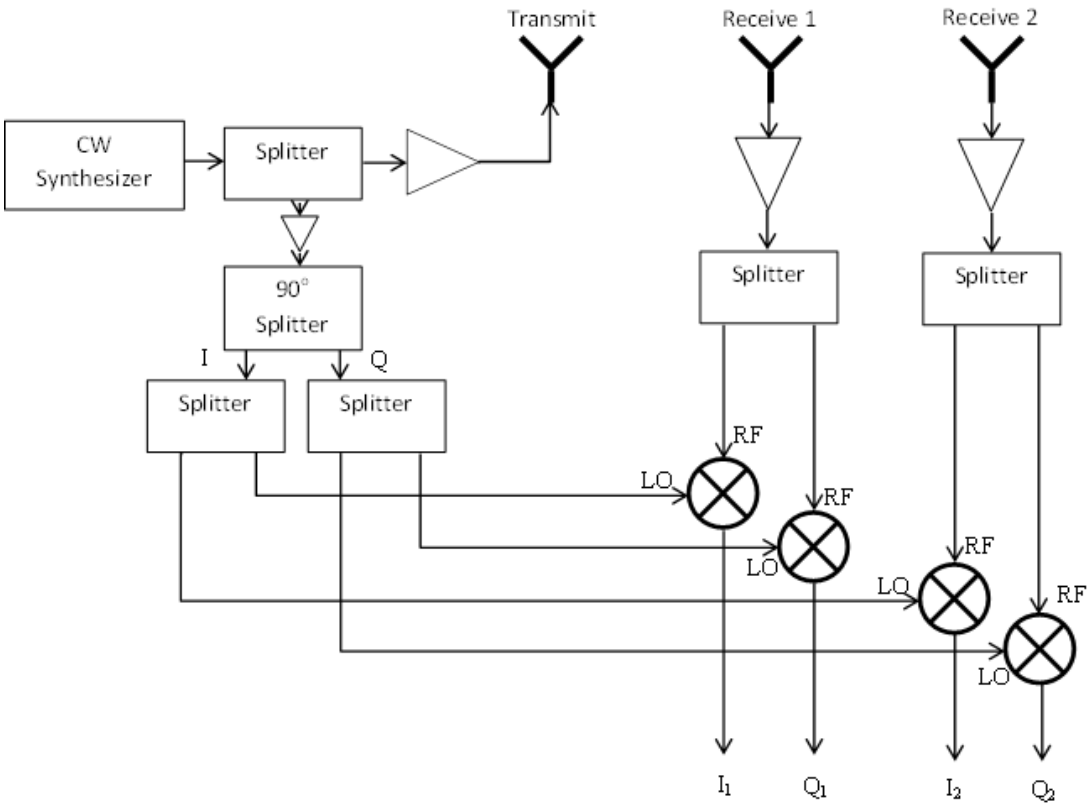

Figure 9.7: Simplified block diagram of the 2-sensor radar system.

Ten trials were averaged for each angle. An example of the received signals is shown in Figure 9.8. This figure shows the STFT when the pendulum was swinging at approximately 25°. At this angle, the pendulum moves toward both receive antennas simultaneously and then away from the antennas simultaneously. This can be seen in Figure 9.8 where the phase difference between the received signals is 0°. The radar has a strong lower sideband that is clear in this figure, but the stronger upper sideband indicates the direction of travel. After calculating the

oscillation angle at 5 degree increments, the results are shown in Figure 9.9.

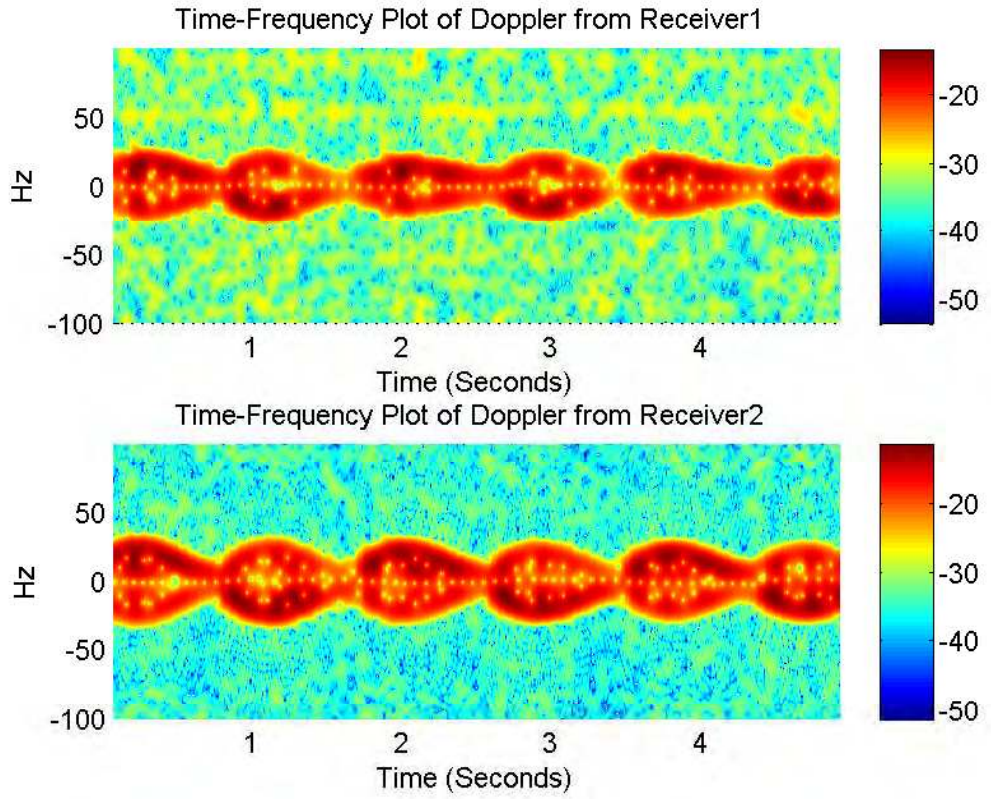

Figure 9.8: (Top) STFT of the experimentally measured Doppler signal from receiver 1 and (Bottom) STFT of the experimentally measured Doppler signal from receiver 2 using a pendulum.

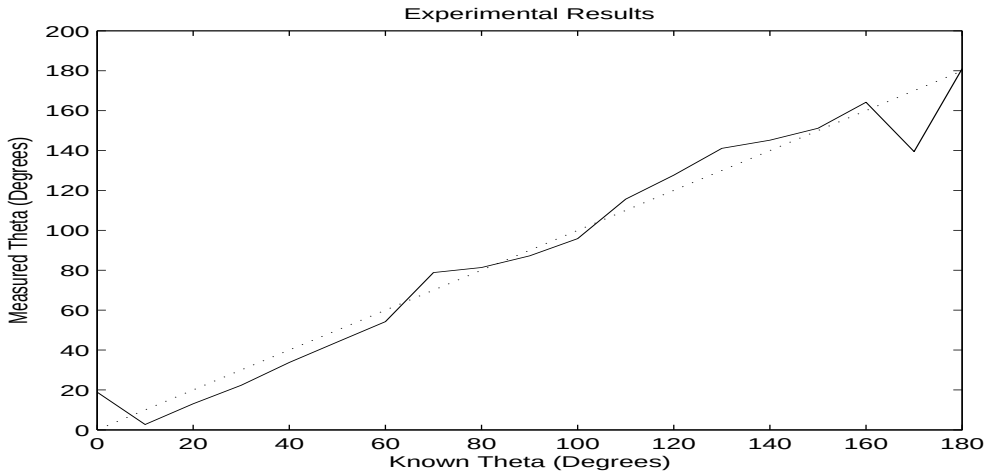

Figure 9.9: Experimentally measured angle using a pendulum as the target.

The procedure has also been tested using the same human motions that were considered for classification. To remind the reader, the motions are: breathing, swinging arms, picking up an object, and standing up from a crouching position. Figures 9.10, 9.11, 9.12, and 9.13 show the results for swinging arms, picking up an object, transitioning from crouching to standing, and breathing respectively.

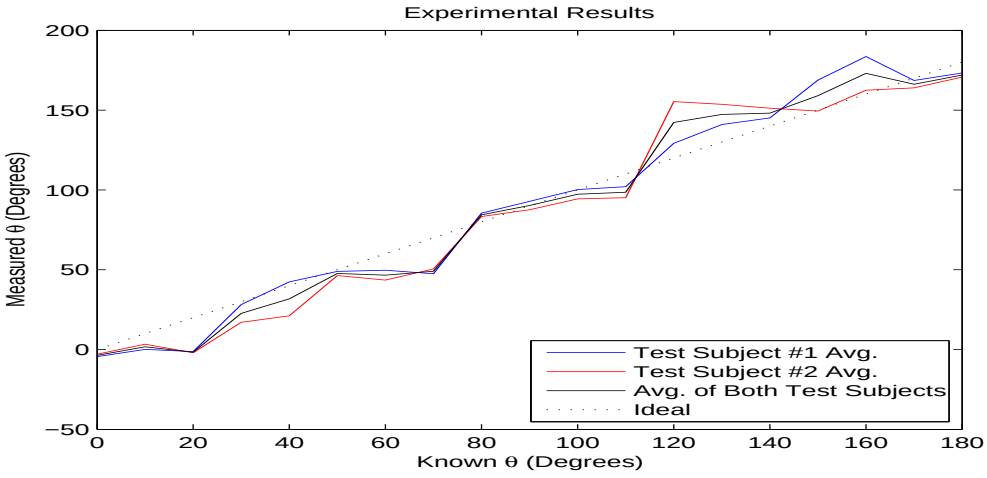

Figure 9.10: Experimentally measured angle for a human swinging their arms.

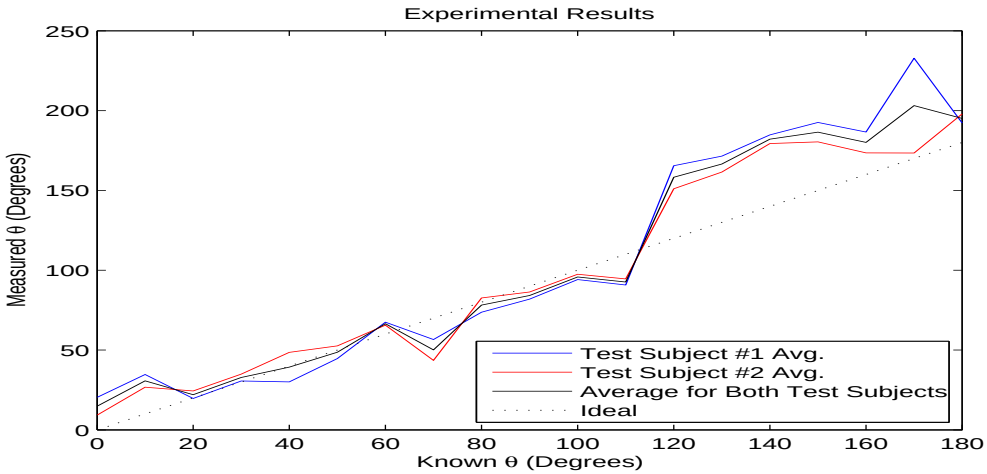

Figure 9.11: Experimentally measured angle for a human picking up an object.

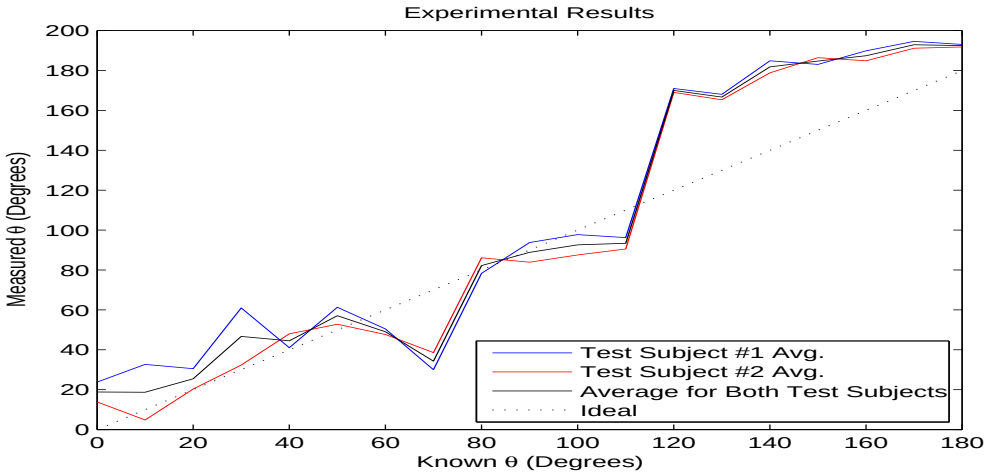

Figure 9.12: Experimentally measured angle for human transitioning from crouching to standing.

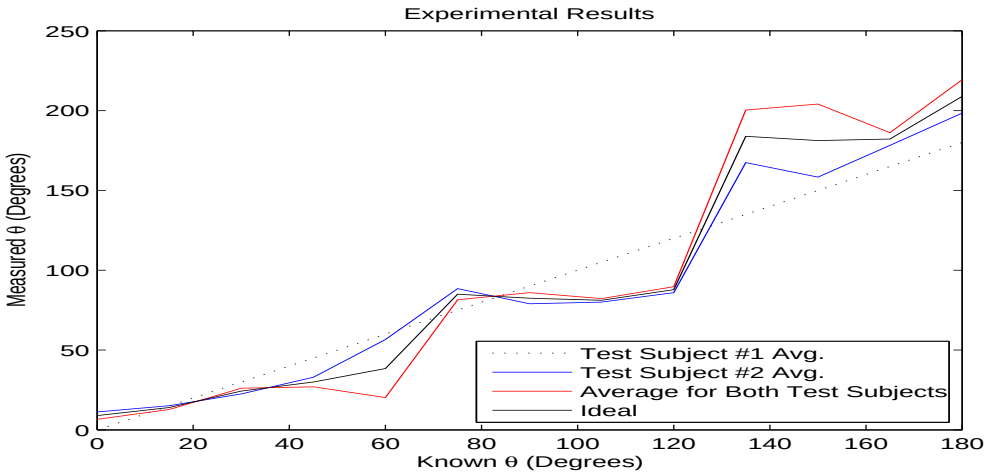

Figure 9.13: Experimentally measured angle for a human breathing while standing.

9.4 Classification of MIMO Doppler Signals

In addition to determining the orientation of an oscillating target, we also are interested in how the classification algorithm performs when the target is not directly facing the antennas. We are also interested whether using a MIMO radar architecture will improve classification. To answer these questions, the MIMO radar described above was used. To mimic the earlier monostatic classification scenario, one receive antenna was placed very close to the transmit antenna so that the angle between them was nearly zero. The second transmit antenna was placed at 45° to the right of the transmit antenna. A diagram of this setup is shown in Figure 9.14 for clarity.

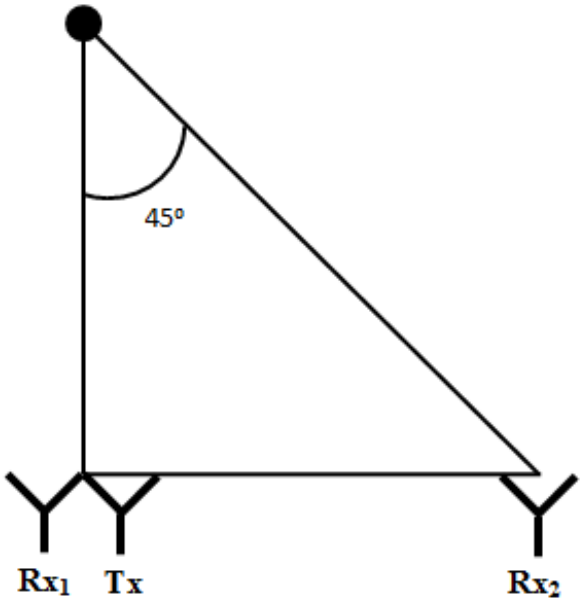

Figure 9.14: Setup for collecting MIMO Doppler data for classification.

Five test subjects performed the motions of swinging their arms and picking up an object at a distance of 10 feet from the transmit antenna. Background noise data were also collected, to bring the total number of motions to 3. The test subjects performed these motions (1) while facing directly toward the transmit antenna and (2) while facing at a 90° angle from the transmit antenna. For the classification, the training set consisted of data from receive antenna 1 while the human target was facing directly toward the transmit antenna. Once this was completed, we can investigate multiple scenarios. These scenarios are listed in Table 9.1.

Table 9.1: Description of classification scenarios when the antennas are placed linearly.

Scenario	Geometry
1	monostatic sensor with the target facing 0°
2	monostatic sensor with the target facing 90°
3	bistatic sensor with the target facing 0°
4	bistatic sensor with the target facing 90°

We expect the classification accuracy of scenario 1 to be very high because it is the training scenario. The classification accuracy of scenario 2 is expected to be lower because movements at 90° from the monostatic Doppler radar produce no Doppler shift. However, human motions do not follow straight lines and often have additional components aside from the main movement. The radar is able to detect the smaller, but still perceptible components of the human motions that are in the radial direction, making classification still possible for this scenario. For scenarios 3 and 4, the classification accuracies are expected to be lower than scenario 1. Based on inspection of equation 9.2, there is an additional $\cos(\varphi/2)$ component that will decrease the Doppler frequency shift when compared to the monostatic case. Because the angle between the transmit antenna and receive antenna # 2 is 45°, when the person is moving at an angle of 0° in relation to the transmit antenna, the angle of δ_2 in equation 9.2 is 22.5°. When the person is moving perpendicular to the transmit antenna, δ_2 is equal to 67.5°. Thus, scenario 4 should produce lower classification accuracies than scenario 3. Similarly, for scenario 2, the antenna configuration is monostatic and δ_1 is 90°. Therefore, we expect that this scenario would produce the worst results among the 4 scenarios.

The advantage of using a bistatic configuration is that target motion orthogonal to the transmit antenna will be non-zero. This means that if no Doppler is detected by the monostatic Doppler sensor, the motion can still be detected by the bistatic Doppler sensor. We can also consider the converse situation where the target motion is orthogonal to $\varphi/2$ ($\delta = 90°$ or $\theta = 90° - \varphi/2$). This will cause the bistatic Doppler sensor to detect no signal, but the monostatic sensor will still

detect a component of the target's motion.

The classification results for each of the scenarios described above are shown in Table 9.2. Some observations can be made based on this table. First, because human motions do not follow perfectly straight paths, the results of scenario #2 are not zero. Second, we expect scenario 2 (antenna #1, target angle = 90°) to produce the worst results. However, scenario 4 (antenna #2, target angle = 90°) actually produces the lowest classification accuracy. The reasoning for this is that the antennas were placed in a line, without considering the total path length of the electromagnetic waves. The path length to antenna 1 is 20 feet, whereas the path length to antenna 2 is 24.14 feet. This will lower the signal to noise ratio by 1.6 dB. I obtained this value by using the bistatic radar range equation. There is a factor R_r^2 in the denominator, which makes it a factor of approximately 1.45 overall, thus 1.6 dB lower.

Table 9.2: Classification results using a multi-sensor radar with human targets facing in two different directions when the receive antennas are placed linearly as in Figure 9.2.

	Antenna #, Target Orientation			
	1,0°	**1,90°**	**2,0°**	**2,90°**
Min (%)	92.0	67.6	78.7	59.6
Max (%)	97.8	74.7	84.4	68.0
Mean (%)	95.0	71.0	82.2	64.3
St. Dev.	1.29	1.72	1.39	2.88

Because of the path length difference between the monostatic and the bistatic sensors, the experiment above was repeated with both path lengths equal to 20 feet. The angle between the transmitter and receiver #2 was maintained at 45°. This experimental setup is shown in Figure 9.15. In addition to changing the path length of the bistatic sensor, the experiment was also expanded to include targets moving at 45° relative to the transmit antenna. The results of this experiment are shown in Table 9.4. Again, the monostatic case with the target facing 0° was used as the training scenario and the other cases were used for testing. The six

scenarios are listed in Table 9.3.

Table 9.3: Description of classification scenarios when the total path lengths are equal for both sensors.

Scenario	Geometry
1	monostatic sensor with the target facing 0°
2	monostatic sensor with the target facing 45°
3	monostatic sensor with the target facing 90°
4	bistatic sensor with the target facing 0°
5	bistatic sensor with the target facing 45°
6	bistatic sensor with the target facing 90°

Scenarios 2, 4, and 5 produce similar results because $\delta = 22.5°$ for each of these cases. Moreover, the accuracy of scenario 2 is slightly higher than scenarios 4 and 5 because the bistatic Doppler equation has an additional $\cos(\varphi/2)$ term, which lowers the bistatic accuracy slightly. Furthermore, the results of scenarios 3 and 6 are lower than the other scenarios because the δ angles are larger for these cases than for the others. The accuracy of scenario 3 is lower than that of scenario 6 because $\delta = 90°$. Scenario 6 is low, but not as low as scenario 6, because $\delta = 67.5°$ and also because of the $cos(\varphi/2)$ term in the bistatic Doppler equation.

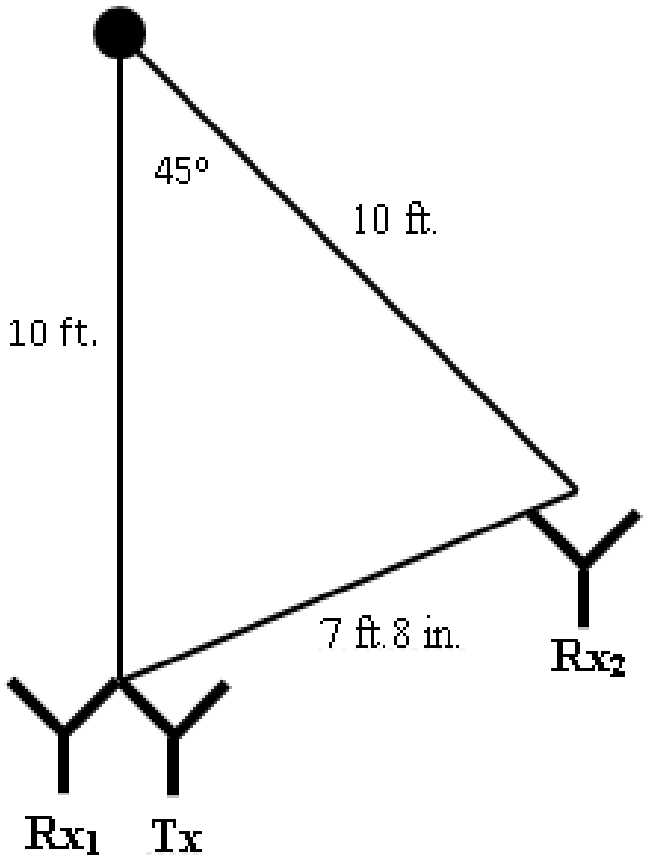

Figure 9.15: Setup for collecting MIMO Doppler data for classification.

Table 9.4: Classification results using a multi-sensor radar with human targets facing in multiple directions when the total path lengths are equal for both sensors.

	Antenna #, Target Orientation					
	1,0°	**1,45°**	**1,90°**	**2,0°**	**2,45°**	**2,90°**
Min (%)	95.6	76.0	60.0	72.4	70.7	62.2
Max (%)	98.2	80.9	68.9	82.2	84.0	73.3
Mean (%)	96.8	78.4	64.7	77.8	77.9	67.0
St. Dev.	0.79	1.66	2.50	2.71	3.13	2.87

These classification results clearly show that high accuracies are possible even

if the target is not facing the radar line of sight and also for a bistatic radar configuration. If human motions could be performed in perfectly straight paths, the Doppler frequency for the scenario with a monostatic sensor and a target angle of 90° should be zero. However, because a human target's motion will have some components in other directions, the radar is capable of detecting them. These results also illustrate that it may be possible to improve the classification algorithm described earlier by using multiple sensors. The data from these sensors could be fused together in some manner or additional features can be extracted to attempt to improve the classification accuracy. The accuracy can potentially be improved because the information in each sensor can provide redundancy that may solidify the results. Furthermore, the two sensors may compliment each other by providing information that the other sensor was incapable of picking up.

Confusion matrices have also been obtained for the 2-sensor Doppler radar system. They have been obtained for scenarios 1, 2, and 5 of Table 9.4 and the confusion matrices are shown in Tables 9.5, 9.6, and 9.7. Table 9.5 shows that scenario 1 (monostatic sensor with the target facing directly toward the antennas) achieves excellent classification not only for the total set, but also for each individual motion that is classified. Tables 9.6 and 9.7 begin to show where the classification accuracy decreases. Class #'s 1 and 3 (background and picking up an object) achieve a high classification accuracy even though the target is facing a different direction, and in the bistatic case, even though the radar antennas are not colocated. The accuracy of class #2 (swinging arms) shows a significant reduction when compared to the training scenario. Another observation is that the monostatic configuration of Table 9.6 slightly outperforms the bistatic configuration of Table 9.7.

Table 9.5: Confusion Matrix for the Classification of Scenario #1 (Monostatic radar with the target at an angle of 0°).

Output Class \ Target Class	**1**	**2**	**3**
1	100	0	0.8
2	0	95.6	4.4
3	0	4.4	94.8

Table 9.6: Confusion Matrix for the Classification of Scenario #2 (Monostatic radar with the target at an angle of 45°).

Output Class \ Target Class	**1**	**2**	**3**
1	100	0.2	2.0
2	0	53.0	13.7
3	0	46.8	84.3

Table 9.7: Confusion Matrix for the Classification of Scenario #5 (Bistatic radar with the target at an angle of 45°).

Output Class \ Target Class	**1**	**2**	**3**
1	100	1.0	2.3
2	0	48.5	8.3
3	0	50.5	89.4

Chapter 10

Conclusions and Recommendations for Future Work

10.1 Conclusions

Two radar systems have been successfully constructed for the detection of defilade human targets. The S-band radar is capable of ranging targets through wall barriers such as brick and concrete at short distances, whereas the millimeter-wave radar is capable of ranging human targets at longer distances and through light foliage.

Classification of human motions has also been demonstrated and has been shown to achieve accuracies up to 90% when using empirical mode decomposition for feature extraction. Based on ROC-like curves, the support vector machine classifier was shown to select the optimal parameters for classification. Also, error analysis shows that human motion classification is robust to small perturbations of the feature values. This confirms that the support vector machine is indeed, forming an optimal separating hyperplane that maximizes the margin between classes.

In addition to classification, simulations of micro-Doppler signatures that arise from simple human motions have been created. These models demonstrate that complex human movements can be reasonably approximated by simpler models and that these models very accurately mimic experimentally measured micro-Doppler

responses.

In regards to the MIMO Doppler radar, an algorithm has been developed that is capable of not only measuring time-varying micro-Doppler signals, but can also predict with reasonable accuracy the orientation of the Doppler target. This, when combined with target ranging, can provide the radar operator with valuable information. Utilizing a bistatic Doppler configuration, accurate classification results were obtained for targets that were facing in different directions. The ability of the classifier to be accurate for different target orientations is extremely important because uncooperative targets may not be facing directly toward the radar.

10.2 Future Work

The radar systems that have been developed have been shown to yield accurate and reliable results; however, the systems can be improved. If the micro-Doppler radars can improve their sensitivity, then it is possible that additional information such as respiration and heart rates may be inferred. Information about whether or not a human target has an increased respiration or heart rate can be useful to the warfighter. It would alert them to potential human threats that may be under stress due to concealed explosives or possibly tell a soldier that an enemy is fatigued.

In addition to increasing the system sensitivity, additional work may be able to improve the classification accuracy by being more selective about which EMD features are beneficial for classification and which EMD features may not provide any discriminating information in regards to human movements.

The MIMO radar can be improved significantly by eliminating mixer sidebands that often undermine the need to use a coherent Doppler radar. The power in the sideband is often comparable to the main Doppler signal, which leads to confusion concerning the direction of motion. This information is critical to selecting the appropriate equation to use for angle estimation. The results shown in section 9.14 suggest that the classification algorithm may be improved upon if multiple sensors are used. A method for combining the information obtained from each sensor can be developed to achieve this. The classification can be improved because the information from each sensor can provide redundancy that may solidify the

results and can also complement each other by providing information that the other sensors may not pick up.

Bibliography

[1] Currie, N. C., D. D. Ferris, R. W. McMillan, and M. C. Wicks (1997) "New law enforcement applications of millimeter-wave radar," in *Proc. SPIE on Radar Sensor Technology II*, vol. 3066, Orlando, FL, pp. 2–10.

[2] Kim, Y. and H. Ling (2009) "Human Activity Classification Based on Micro-Doppler Signatures Using a Support Vector Machine," *IEEE Transactions on Geoscience and Remote Sensing*, **47**(5), pp. 1328–1337.

[3] Raj, R. G., V. C. Chen, and R. Lipps (2009) "Analysis of radar dismount signatures via non-parametric and parametric methods," in *2009 IEEE Radar Conference*, pp. 1 –6.

[4] Zhang, Z., P. Pouliquen, A. Waxman, and A. G. Andreou (2007) "Acoustic Micro-Doppler Gait Signatures of Humans and Animals," in *41st Annual Conference on Information Sciences and Systems, 2007. CISS '07.*, pp. 627 –630.

[5] Ram, S. S. and H. Ling (2008) "Micro-Doppler Signature Simulation of Computer Animated Human and Animal Motions," in *Antennas and Propagation Society International Symposium, 2008. AP-S 2008. IEEE*, pp. 1–4.

[6] Chen, P. H., M. C. Shastry, C. P. Lai, and R. M. Narayanan (2012) "A Portable Real-Time Digital Noise Radar System for Through-the-Wall Imaging," *IEEE Transactions on Geoscience and Remote Sensing*, **50**(10), pp. 4123 –4134.

[7] Daniels, D. J. (1996) "Surface-penetrating radar," *Electronics Communication Engineering Journal*, **8**(4), pp. 165 –182.

[8] Falconer, D. G., K. N. Steadman, and D. G. Watters (1996) "Through-the-wall differential radar," in *Proc. SPIE on Command, Control, Communications, and Intelligence Systems for Law Enforcement*, vol. 2938, pp. 147–151.

[9] Grant, M. P., G. R. Cooper, and A. K. Kamal (1963) "A class of noise radar systems," *Proceedings of the IEEE*, **51**(7), pp. 1060–1061.

[10] Cooper, G. R. (1967) *Random Signal Radar*, *paper 366*, Purdue University.

[11] Chen, V. (2011) *The Micro-Doppler Effect in Radar*, Artech House Remote Sensing Library, Artech House.
URL `http://books.google.com/books?id=rE4qmQEACAAJ`

[12] Chen, V. C. (2005) "Spatial and temporal independent component analysis of micro-Doppler features," in *Radar Conference, 2005 IEEE International*, pp. 348–353.

[13] Chen, V. (2008) "Doppler signatures of radar backscattering from objects with micro-motions," *Signal Processing, IET*, **2**(3), pp. 291–300.

[14] Chen, V. C., F. Li, S. S. Ho, and H. Wechsler (Aug.) "Analysis of micro-Doppler signatures," *Radar, Sonar and Navigation, IEE Proceedings* -, **150**(4), pp. 271–6–.

[15] Chen, V. C. (2000) "Analysis of radar micro-Doppler with time-frequency transform," in *Statistical Signal and Array Processing, Proceedings of the Tenth IEEE Workshop on*, pp. 463–466.

[16] Bakhtiari, S., T. W. Elmer, N. M. Cox, N. Gopalsami, A. C. Raptis, S. Liao, I. Mikhelson, and A. V. Sahakian (2012) "Compact Millimeter-Wave Sensor for Remote Monitoring of Vital Signs," *Instrumentation and Measurement, IEEE Transactions on*, **61**(3), pp. 830–841.

[17] Mikhelson, I. V., S. Bakhtiari, T. W. Elmer, and A. V. Sahakian (June) "Remote Sensing of Heart Rate and Patterns of Respiration on a Stationary Subject Using 94-GHz Millimeter-Wave Interferometry," *Biomedical Engineering, IEEE Transactions on*, **58**(6), pp. 1671–1677.

[18] Silvious, J. and D. Tahmoush (2010) "UHF measurement of breathing and heartbeat at a distance," in *Radio and Wireless Symposium (RWS), 2010 IEEE*, pp. 567–570.

[19] Lubecke, V. M., O. Boric-Lubecke, A. Host-Madsen, and A. Fathy (2007) "Through-the-Wall Radar Life Detection and Monitoring," in *International Microwave Symposium, 2007. IEEE/MTT-S*, pp. 769 –772.

[20] Droitcour, A., V. Lubecke, J. Lin, and O. Boric-Lubecke (2001) "A microwave radio for Doppler radar sensing of vital signs," in *Microwave Symposium Digest, 2001 IEEE MTT-S International*, vol. 1, pp. 175–178 vol.1.

[21] Richards, M. A., J. A. Scheer, and W. A. Holm (2010) *Principles of Modern radar basic Principles*, SciTech Publishing, North Carolina.

[22] Jordon, J., P. Bishop, and B. Kiani (1989) *Correlation-based measurement systems*, 2nd ed., Ellis Horwood Limited, Chichester, West Sussex.

[23] Nguyen, D. P., N. Petrochilos, A. Host-Madsen, V. Lubecke, and O. Boric-Lubecke (2007) "A versatile through-the-wall Doppler radar using BSS algorithms," in *2007 IEEE Antennas and Propagation Society International Symposium*, pp. 273 –276.

[24] Muqaibel, A., A. Safaai-Jazi, A. Bayram, A. M. Attiya, and S. M. Riad (2005) "Ultrawideband through-the-wall propagation," *IEE Proc. on Microwaves, Antennas and Propagation*, pp. 581 – 588.

[25] Safaai-Jazi, A., S. M. Riad, A. Muqaibel, and A. Bayram (2002) *Ultra-wideband propagation measurements and channel modeling, Tech. rep.*, DARPA NETEX Program, Report on "Through-the-wall propagation and material characterization", available online at `http://www.darpa.mil/ato/solicit/netex/docs/models.pdf`.

[26] Wilson, R. (2002) *Propagation Losses Through Common Building Materials: 2.4 GHz vs. 5 GHz, Tech. rep.*, University of Southern California.

[27] Amin, M. G. (2011) *Through-the-wall Radar Imaging*, CRC Press.

[28] Oughstun, K. and N. Cartwright (2003) "On the Lorentz-Lorenz formula and the Lorentz model of dielectric dispersion," *Opt. Express*, **11**(13), pp. 1541–1546, `http://www.opticsexpress.org/abstract.cfm?URI=oe-11-13-1541`.

[29] Raj, R. G., V. C. Chen, and R. Lipps (2010) "Analysis of radar human gait signatures," *IET Signal Processing*, **4**(3), pp. 234 –244.

[30] Lin, A. and H. Ling (2005) "Through-wall measurements of a Doppler and direction-of-arrival (DDOA) radar for tracking indoor movers," in *2005 IEEE Antennas and Propagation Society International Symposium*, vol. 3B, pp. 322 – 325 vol. 3B.

[31] Boulic, R., N. M. Thalmann, and D. Thalmann (1990) "A global human walking model with real-time kinematic personification," *The Visual Computer*, **6**, pp. 344–358, 10.1007/BF01901021.
URL `http://dx.doi.org/10.1007/BF01901021`

[32] Lai, C. P., R. M. Narayanan, Q. Ruan, and A. Davydov (2008) "Hilbert-Huang transform analysis of human activities using through-wall noise and noise-like radar," *IET Radar, Sonar Navigation*, **2**(4), pp. 244 – 255.

[33] (2005) "IEEE Standard for Safety Levels with Respect to Human Exposure to Radio Frequency Electromagnetic Fields, 3 kHz to 300 GHz," *IEEE C95.1-2005*.

[34] Kraus, J. D. (1988) *Antennas*, 2nd ed., McGraw-Hill, New York, NY.

[35] Stutzman, W. L. and G. A. Thiele (1998) *Antenna Theory and Design*, 2nd ed., John Wiley & Sons, Hoboken, NJ.

[36] Cohen, L. (1995) *Time-Frequency Analysis*, Prentice Hall PTR.

[37] Huang, N. E. and S. P. Shen (2005) *Hilbert-Huang Transform and Its Applications*, World Scientific Publishing Co.

[38] Huang, N. E., Z. Shen, S. R. Long, M. C. Wu, H. H. Shih, Q. Zheng, N. C. Yen, C. C. Tung, and H. H. Liu (1998) "The empirical mode decomposition and the Hilbert spectrum for nonlinear and non-stationary time series analysis," *Proceedings of the Royal Society A*, **454**(1971), pp. 679–699.

[39] Chen, V. and H. Ling (2002) *Time-Frequency Transforms for Radar Imaging and Signal Analysis*, Artech House.

[40] Hlawatsch, F. and F. Auger (2005) *Time-Frequency Analysis: Concepts and Methods*, Wiley.

[41] Strang, G. and T. Nguyen (1996) *Wavelets and Filter Banks*, Wellesley-Cambridge Press.

[42] Du, Q. and S. Yang (2007) "Application of the EMD method in the vibration analysis of ball bearings," *Mechanical Systems and Signal Processing*, **21**(6), pp. 2634–2644.

[43] Narayanan, R. M., M. C. Shastry, P. H. Chen, and M. Levi (2010) "Through-the-wall detection of stationary human targets using Doppler radar," *Progress in Electromagnetics Research B*, **20**, pp. 147–166.

[44] Fairchild, D. P. and R. M. Narayanan (2012) "Classification and modeling of human activities using empirical mode decomposition with S-band and millimeter-wave micro-Doppler radars," in *Proc. SPIE Conference on Radar Sensor Technology XVI*, Baltimore, MD, pp. 83610X–83610X–15.

[45] Gallagher, K. A. and R. M. Narayanan (2012) "Simultaneous human detection and ranging using a millimeter-wave radar system transmitting wideband noise with an embedded tone," in *Proc. SPIE Conference on Radar Sensor Technology XVI*, vol. 8361, Baltimore, MD, pp. 836119–1 – 836119–10.

[46] Bugaev, A. S., V. V. Chapursky, S. I. Ivashov, V. V. Razevig, A. P. Sheyko, and I. A. Vasilyev (2004) "Through wall sensing of human breathing and heart beating by monochromatic radar," in *Proceedings of the Tenth International Conference on Ground Penetrating Radar, 2004. GPR 2004.*, vol. 1, pp. 291 –294.

[47] Chia, M. Y. W., S. W. Leong, C. K. Sim, and K. M. Chan (2005) "Through-wall UWB radar operating within FCC's mask for sensing heart beat and breathing rate," in *Radar Conference, 2005. EURAD 2005. European*, pp. 267 –270.

[48] Ivashov, S., V. Razevig, A. Sheyko, and L. Vasilyev (2004) "Detection of human breathing and heartbeat by remote radar," in *Progress in Electromagnetic Research Symposium*, Pisa, Italy, pp. 663–666.

[49] S.Jiping and L. Mingi (2011) "Life detection and location methods using UWB impulse radar in a coal mine," *Mining Science and Technology (China)*, **21**(5), pp. 687 – 691.
URL `http://www.sciencedirect.com/science/article/pii/S1674526411001281`

[50] Levitas, B. and J. Matuzas (2006) "UWB Radar for Human Being Detection Behind the Wall," in *International Radar Symposium, 2006. IRS 2006.*, pp. 1 –3.

[51] Li, W., X. Jing, Z. Li, and J. Wang (2012) "A new algorithm for through wall human respiration monitoring using GPR," in *14th International Conference on Ground Penetrating Radar (GPR),2012*, pp. 947 –952.

[52] Shirodkar, S., P. Barua, D. Anuradha, and R. Kuloor (2011) "Heartbeat detection and ranging through a wall using ultra wide band radar," in *2011 International Conference on Communications and Signal Processing (ICCSP)*, pp. 579 –583.

[53] Liu, Z., L. Liu, and B. Barrowes (2010) "The Application of the Hilbert-Huang Transform in through-wall life detection with UWB impulse radar," in *PIERS Online*, vol. 6, pp. 695–699.

[54] Liu, L., Z. Liu, and B. E. Barrowes (2011) "Through-Wall Bio-Radiolocation With UWB Impulse Radar: Observation, Simulation and Signal Extraction," *IEEE Journal of Selected Topics in Applied Earth Observations and Remote Sensing*, **4**(4), pp. 791 –798.

[55] Zaikov, E. and J. Sachs (2010) "UWB radar for detection and localization of trapped people," in *2010 11th International Radar Symposium (IRS)*, pp. 1–4.

[56] Wang, Q., Y. Li, J. Wu, and T. Zhang (2009) "Life signal extraction in through-the-wall surveillance," in *Annual International Conference of the IEEE Engineering in Medicine and Biology Society, 2009. EMBC 2009.*, pp. 1343 –1346.

[57] Zeng, Z., J. Sun, J. Li, F. Liu, Q. Lu, and X. Chen (2011) "The analysis of TWI data for human being's periodic motions," in *2011 IEEE International Geoscience and Remote Sensing Symposium (IGARSS)*, pp. 862 –865.

[58] Atkeson, C. G. and J. M. Hollerbach (1985) "Kinematic features of unrestrained vertical arm movements," *The Journal of Neuroscience*, **5**(9), pp. 2318–2330.
URL `http://www.jneurosci.org/content/5/9/2318.abstract`

[59] De Groote, A., M. Wantier, G. Cheron, M. Estenne, and M. Paiva (1997) "Chest wall motion during tidal breathing," *Journal of Applied Physiology*, **83**(5), pp. 1531–1537.
URL `http://jap.physiology.org/content/83/5/1531.abstract`

[60] Salan, C., V. Padois, and O. Sigaud (2009) "A Two-Level Model of Anticipation-Based Motor Learning for Whole Body Motion," in *Anticipatory Behavior in Adaptive Learning Systems* (G. Pezzulo, M. Butz, O. Sigaud, and G. Baldassarre, eds.), vol. 5499 of *Lecture Notes in Computer Science*, Springer Berlin Heidelberg, pp. 229–246.
URL `http://dx.doi.org/10.1007/978-3-642-02565-5_13`

[61] Nuzik, S., R. Lamb, A. VanSant, and S. Hirt (1986) "Sit-to-stand movement pattern: a kinematic study," *Physical Therapy*, **66**(11), pp. 1708–1713.
URL `http://ptjournal.apta.org/content/66/11/1708.abstract`

[62] Sibella, F., M. Galli, M. Romei, A. Montesano, and M. Crivellini (2003) "Biomechanical analysis of sit-to-stand movement in normal and obese subjects," *Clinical Biomechanics*, **18**(8), pp. 745 – 750.
URL `http://www.sciencedirect.com/science/article/pii/S026800330300144X`

[63] Corinna, C. and V. Vapnik (1995) "Support-Vector Networks," *Machine Learning*, **20**(3), pp. 273–297.

[64] Chang, C. C. and C. J. Lin (2001) *LIBSVM: a Library for Support Vector Machines*, software available at `http://www.csie.ntu.edu.tw/~cjlin/libsvm`.

[65] Hsu, C. W., C. Chang, and C. J. Lin (2003) *A Practical Guide to Support Vector Classification*, *Tech. rep.*, National Taiwan University, Taipei, Taiwan.

[66] Hsu, C. W. and C. J. Lin (2002) "A Comparison of Methods for Multiclass Support Vector Machines," *IEEE Transactions on Neural Networks*, **13**(2), pp. 415–425.

[67] Rifkin, R. and A. Klautau (2004) "In Defense of One-Vs-All Classification," *Journal of Machine Learning Research*, **5**, pp. 101–141.

[68] Fairchild, D. P. and R. M. Narayanan (2011) "Human activity classification using Hilbert-Huang Transform analysis of radar Doppler data," in *Proc. SPIE Conference on Radar Sensor Technology XV*, Orlando, FL, pp. 80210F–80210F–12.

[69] Chen, P. H., R. M. Narayanan, C. P. Lai, and A. Davydov (2009) "Through wall ranging and imaging using UWB random noise waveform: System design considerations and preliminary results," in *Digest 2009 IEEE International Symposium on Antennas and Propagation*, Charleston, SC, pp. 1–4, doi: 10.1109/APS.2009.5172369.

[70] Rilling, G. and P. Goncalves (2008) *EMD Toolbox for Matlab*, École Normale Supérieure de Lyon, Lyon, France, http://www.perso.ens-lyon.fr/patrick.flandrin/emd.html.

[71] Fairchild, D. P. and R. M. Narayanan (2013) "Micro-Doppler Radar Classification of Human Motions under Various Training Scenarios," in *Proc. SPIE Conference on Radar Sensor Technology XVII*, Baltimore, MD, pp. 873407–873407–11.

[72] Bryan, J. D., J. Kwon, N. Lee, and Y. Kim (2012) "Application of ultra-wide band radar for classification of human activities," *IET Radar, Sonar Navigation*, **6**(3), pp. 172 –179.

[73] fei Zhu, R., Q. Zhang, X. peng Zhu, and Y. Luo (2009) "Micro-Doppler analysis of vibrating target in bistatic radar," in *Synthetic Aperture Radar, 2009. APSAR 2009. 2nd Asian-Pacific Conference on*, pp. 981–984.

[74] jiao Liang, X., Q. Zhang, M. Zhu, and Y. Luo (2010) "Analysis of micro-doppler effect in SIMO radar," in *Signal Processing Systems (ICSPS), 2010 2nd International Conference on*, vol. 2, pp. V2–343–V2–346.

[75] Zhang, W., C. Tong, Q. Zhang, Y. Zhang, and X. Zhang (2012) "Extraction of Vibrating Features With Dual-Channel Fixed-Receiver Bistatic SAR," *Geoscience and Remote Sensing Letters, IEEE*, **9**(3), pp. 507–511.

[76] Luo, Y., J. He, X. jiao Liang, and Q. Zhang (2010) "Three-dimensional micro-doppler signature extraction in MIMO radar," in *Signal Processing Systems (ICSPS), 2010 2nd International Conference on*, vol. 2, pp. V2–1–V2–4.

[77] Karabacak, C., S. Z. Grbz, M. B. Guldogan, and A. C. Grbz (2013) "Multi-aspect angle classification of human radar signatures," , pp. 873408–873408–10.
URL +http://dx.doi.org/10.1117/12.2017709

Vita

Dustin P. Fairchild

Dustin Fairchild

- Educational Background

  1. Ph.D., Electrical Engineering, Aug 2008 - Dec 2013, The Pennsylvania State University, University Park, PA.
  2. B.S., Electrical Engineering, Aug 2004 - May 2008, Penn State Erie, The Behrend College, Erie, PA.

- Professional Experience

  1. The Pennsylvania State University, Research Assistant, August 2009 - July 2013.
  2. The Pennsylvania State University, Teaching Assistant, August 2008 - May 2009; Jan 2013 - May 2013.
  3. SKF Aeroengine, Electrical Engineering Intern, May 2006 - August 2006.

- Publications

  1. Fairchild, D. P. and Narayanan, R. M., "Human activity classification using Hilbert-Huang Transform analysis of radar Doppler data," in Proc. SPIE Conference on Radar Sensor Technology XV, Orlando, FL, pp. 80210F-80210F-12, April 2011.
  2. Fairchild, D. P. and Narayanan, R. M., "Classification and modeling of human activities using empirical mode decomposition with S-band and millimeter-wave micro-Doppler radars," in Proc. SPIE Conference on Radar Sensor Technology XVI, Baltimore, MD, pp. 83610X-86610X-15, April 2012.
  3. Fairchild, D. P. and Narayanan, R. M., "Micro-Doppler radar classification of human motions under various training scenarios," in Proc. SPIE Conference on Radar Sensor Technology XVII, Baltimore, MD, pp. 873407-873407-11, May 2013.
  4. Fairchild, D. P. and Narayanan, R. M., "Classification of human motions using empirical mode decomposition of human micro-Doppler signatures," IET Radar, Sonar, & Navigation, in press (accepted Aug. 2013).
  5. Chapter entitled "Through-the-Wall Micro-Doppler Signatures," to be published in the book: "Radar Micro-Doppler Signatures-Processing and Applications" edited by Victor Chen.